Title
On the Design of Oxide Films, Nanomaterials, and Heterostructures for Solar Water Oxidation Photoanodes

Author
Kronawitter, Coleman

Publication Date
2012

Peer reviewed|Thesis/dissertation

On the Design of Oxide Films, Nanomaterials, and Heterostructures for Solar Water Oxidation Photoanodes

By

Coleman Xaver Kronawitter

A dissertation submitted in partial satisfaction of the

requirements for the degree of

Doctor of Philosophy

in

Engineering – Mechanical Engineering

in the

Graduate Division

of the

University of California, Berkeley

Committee in charge:

Professor Samuel S. Mao, Co-Chair
Professor Ralph Greif, Co-Chair
Professor Xiang Zhang
Professor David Graves

Spring 2012

On the Design of Oxide Films, Nanomaterials, and Heterostructures
for Solar Water Oxidation Photoanodes

by

Coleman Xaver Kronawitter

Abstract

On the Design of Oxide Films, Nanomaterials, and Heterostructures
for Solar Water Oxidation Photoanodes

by

Coleman Xaver Kronawitter

Doctor of Philosophy in Engineering – Mechanical Engineering

University of California, Berkeley

Professor Samuel S. Mao, Co-Chair
Professor Ralph Greif, Co-Chair

Photoelectrochemistry and its associated technologies show unique potential to facilitate the large-scale production of solar fuels – those energy-rich chemicals obtained through conversion processes driven by solar energy, mimicking the photosynthetic process of green plants. The critical component of photoelectrochemical devices designed for this purpose is the semiconductor photoelectrode, which must be optically absorptive, chemically stable, and possess the required electronic band alignment with respect to the redox couple of the electrolyte to drive the relevant electrochemical reactions. After many decades of investigation, the primary technological obstacle remains the development of photoelectrode structures capable of efficient and stable conversion of light with visible frequencies, which is abundant in the solar spectrum. Metal oxides represent one of the few material classes that can be made photoactive and remain stable to perform the required functions. The unique range of functional properties of oxides, and especially the oxides of transition metals, relates to their associated diversity of cation oxidation states, cation electronic configurations, and crystal structures.

In this dissertation, the use of metal oxide films, nanomaterials, and heterostructures in photoelectrodes enabling the solar-driven oxidation of water and generation of hydrogen fuel is examined. A range of transition- and post-transition-metal oxide material systems and nanoscale architectures is presented. The first chapters present results related to electrodes based on alpha-phase iron(III) oxide, a promising visible-light-active material widely investigated for this application. Studies of porous films fabricated by physical vapor deposition reveal the importance of structural quality, as determined by the deposition substrate temperature, on photoelectrochemical performance. Heterostructures with nanoscale feature dimensionality are explored and reviewed in a later chapter, which describes the methodologies to combine the unique and complimentary functional properties of dissimilar oxides to optimize the water photo-oxidation process Experimental results based on an iron(III) oxide-tungsten(VI) oxide system show enhancements associated with the heterostructure, which may indicate the presence of unexpected minority carrier dynamics, as observed additionally by ultrafast transient absorption spectroscopy.

Next, a new conceptual framework for the design of solar water oxidation photoelectrodes based on the spatially inhomogeneous doping of wide-bandgap metal oxide nanostructures is introduced and experimentally verified. It is found that optical absorption and electronic conduction can be decoupled and optimized by spatially segregating the functional impurity species that facilitate their associated physical processes. In the final chapters of this dissertation the electronic structures of key oxide-oxide interfaces, relevant to the operation of efficient photoanodes, are examined using synchrotron-based soft x-ray spectroscopy. These studies indicate that the interfacial regions of electrodes possess distinct electronic structures, which deviate in terms of orbital character and occupancy from those of their constituent bulk oxides. These observations inform methodology to address certain operational deficiencies associated with the use of metal oxides for solar energy conversion applications.

To my parents, Herbert and Luanne,
for twenty-eight years of love and support,
without which this work would not have been possible

Acknowledgements

I would like to express my most sincere gratitude to my advisor Samuel S. Mao, for his guidance and support over the past six years. On a nearly daily basis he has given me technical and professional advice, which has greatly enriched my education at Berkeley. He has provided me with countless opportunities, including travel throughout the country and abroad to present my research and learn from the scientific community. I would like to additionally thank Professor Ralph Greif, for advising me throughout my time in the Mechanical Engineering doctoral program, and for serving on my dissertation committee. Special thanks are also due to Professor Xiang Zhang and Professor David Graves for serving on my dissertation committee.

The majority of the research in this dissertation was funded by Sandia National Laboratories, through the University of California, Berkeley Excellence in Engineering Fellowship. I would like to thank Bonnie Antoun of Sandia National Laboratories for supporting me as a Fellow, which gave me the freedom to research this field as I saw fit.

I would like to acknowledge and thank Lionel Vayssieres, for providing a unique perspective to my research and introducing me to new aspects of the field, both of which have shaped and guided the direction of my research. He organized several fruitful collaborations with professors, scientists, and students at the Advanced Light Source, UC Santa Cruz, and Stanford University, which greatly increased the quality and depth of my research. Thanks are due to Jinghua Guo, Jin Zhang, and Stacey Bent and their research groups for their collaboration.

I would like to thank many people in Berkeley for their friendship, which helped make the last six years so enjoyable: John Edmiston, Armon Mahajerin, Daniel Peters, Travis Owens, Derrick Speaks, Tim Suen, Russell Carrington, Shaohua Shen, Zhixun Ma, Dongfang Liu, Sara Al-Beaini, Heather Chiamori, Amanda Dodd, Tony Ho, Matt Beres, Mike Fina, Matt Rogers, Jay James, Vassilia Zorba, Mukes Kapilashrami, Ioannis Zegkinoglou, and many others. Many friends are classmates in the Department of Mechanical Engineering or colleagues at Lawrence Berkeley National Laboratory, and contributed considerably to my education at Berkeley.

Finally, I owe so much to my parents, Herbert and Luanne Kronawitter, and to my brother Lukas Kronawitter, for supporting me and my decision to move to Berkeley for my continued education. The same is true for my aunts, Linda Piotrowski, Lisa Stackhouse, Charlene Bembenek, and Diane Dowd, and all my other family and friends, who always stayed interested in my life and studies in Berkeley.

Contents

Figures

1 Introduction

Quantitative analyses of global power consumption statistics have highlighted the necessity to distinguish between electricity and fuel use in the development and prioritization of solar energy conversion technologies.[1] Our global society is particularly reliant on stored energy: the worldwide average energy consumption rate is approximately 15-16 TW,[2] only about 17% of which represents electricity use.[3] The remaining energy is consumed mainly from chemical fuels by processes requiring heat or involving combustion, including for example manufacturing, transportation, and heating and cooling.[4] For this reason sustainable global energy production schemes must address the production of chemical fuels, which can be most easily stored and transported, as well as integrated into existing infrastructure. Solar energy, arriving on Earth at a rate of *ca.* 150,000 TW, provides the most distributed and abundant global energy resource and must facilitate future energy production scenarios based on renewable sources. Solar fuels – those high-energy-density chemicals whose bond energies are obtained through conversion processes driven by solar energy, mimicking the photosynthetic process of green plants – have the unique potential to significantly contribute to the storage of renewable energy on a large scale.

The production of chemical fuels using solar energy typically involves the simultaneous generation of oxygen and a reduced fuel such as hydrogen or organic species. To be effective this conversion process must be made significantly more efficient than natural photosynthesis, which for crop plants is typically less than 1% (for example based on the energy content of annually harvested biomass per area divided by the annual solar irradiance).[2] Photoelectrochemical processes show potential for the production of solar fuels, especially hydrogen gas from solar water splitting, because they simultaneously facilitate optoelectronic and chemical conversion processes.

The critical component of photoelectrochemical water splitting devices is the photoelectrode, which must be optically absorptive, chemically stable, and possess the appropriate electronic band alignment with respect to the electrochemical scale for its charge carriers to have sufficient potential to drive the hydrogen and oxygen evolution reactions. After many decades of investigation,[5] the primary technological obstacle remains the development of photoelectrode structures capable of efficient conversion of light with visible frequencies, which is abundant in the solar spectrum. Metal oxides represent one of the few material classes that can be made photoactive and remain stable to perform the required optical, electronic, and chemical functions required of photoelectrochemical solar water splitting cells. The unique range of functional properties of oxides, and especially the oxides of transition metals, relates to their associated diversity of cation oxidation states, crystal structures, and electronic configurations. This dissertation is intended as a contribution toward development of oxide photoelectrodes whose purpose is to oxidize water for the solar-driven generation of hydrogen in photoelectrochemical cells.

1.1 Introduction to contents

The studies in this dissertation are organized to most accurately represent the progression of ideas developed during the course of the experimental research. The initial portion presents a summary introduction to photoelectrochemistry and the basic principles involved in photoelectrolysis cells with particular focus on the semiconductor photoanode, whose design has been the major focus of this research. Following this, some introductory information on the experimental techniques utilized in this study is presented. Details on the experimental parameters are provided in Chapters 3 through 7 and presented alongside their associated results and discussions, in order to best provide context to the experiments. Similarly, the literature associated with the field is best understood in the context of the specific work carried out, and therefore is presented within the introductory discussions of later chapters.

Chapters 2 through 6 present five distinct and connected studies on the design of oxide films, nanomaterials, and heterostructures for the application of solar water oxidation. Each study builds on basic principles established in its preceding chapters, and they are generally organized by order of increasing complexity. Chapter 2 involves the characterization of thin film-based photoelectrodes which are perhaps the most straightforward system in terms of analysis and interpretation of results. Chapter 3 provides an overview and perspective on the use of nanoscale oxide heterostructures for solar water oxidation photoelectrodes, as well as presents original work on these systems. Chapter 4 establishes a new concept for the design of visible-light-active oxides for this application, based on the spatial separation of impurity distributions within wide-bandgap oxide nanostructures. Characterization of the electronic structure of oxide materials, which introduces a new level of involvement to the discussion, is reserved for the final portion of the dissertation, in Chapters 5 and 6.

1.2 Photoelectrochemistry and solar water splitting

1.2.1 Photoelectrolysis cells

Photoelectrolysis cells are a type of photoelectrochemical cell whose purpose is to drive the water splitting reaction using light energy,

$$H_2O \xrightarrow{h\nu} H_2 + 1/2\, O_2, \tag{1-1}$$

where hν is the photon energy. Within the semiconductor photoelectrode, the absorption of light can be represented as,

$$4h\nu \rightarrow 4h^+ + 4e^-, \tag{1-2}$$

where e^- are electrons and h^+ are holes. The anodic reaction is the oxidation of water, which for the systems analyzed in this dissertation occurs at the surface of a semiconductor photoanode,

$$4h^+ + 4OH^- \rightarrow O_2 + 2H_2O. \tag{1-3}$$

The cathodic reaction, the reduction of water,

$$4e^- + 4H_2O \rightarrow 2H_2 + 4OH^-, \quad (1\text{-}4)$$

occurs at a counter electrode, which in this dissertation is a platinum metal electrode.

The water splitting reaction described above requires 237.141 kJ mol^{-1} (Gibbs free energy, 298 K) to proceed; this quantity represents the thermodynamic requirement for energy input to the system. It is equivalent to 2.4578 eV per H_2 molecule, or 1.23 eV per electron because two electrons are required to generate one H_2 molecule.

A semiconductor photoelectrode whose charge carriers drive the anodic and cathodic reactions therefore must possess an energy separation between valence and conduction bands (bandgap) of 1.23 eV to meet the thermodynamic requirement. In practice, additional potential is required to compensate for various loss mechanisms, most especially the overpotential required to overcome kinetic losses. A bandgap of around 2 eV is typically required to overcome these losses.

1.2.2 Electronic band alignment

In addition to the magnitude of the energy gap between occupied and unoccupied bands in the semiconductor, the alignment of the bands with respect to the redox couple in the electrolyte must be optimized to drive the reactions. For spontaneous water splitting, this means that the valence and conduction bands must straddle the potentials of the H^+/H_2 and O_2/H_2O reactions. The application of an external bias or integration of the PEC cell into a tandem device alleviates this restriction (see Section 1.3 below), although irrespective of the design optimization of materials with this band alignment remains a major goal in the field. The band alignment with respect to the water splitting redox couple of the oxide materials investigated in this dissertation are presented in Figure 1-1. Nominal values are shown because the precise band offsets can shift energies on the order of 0.1 eV, depending on the fabrication technique specific material characteristics.

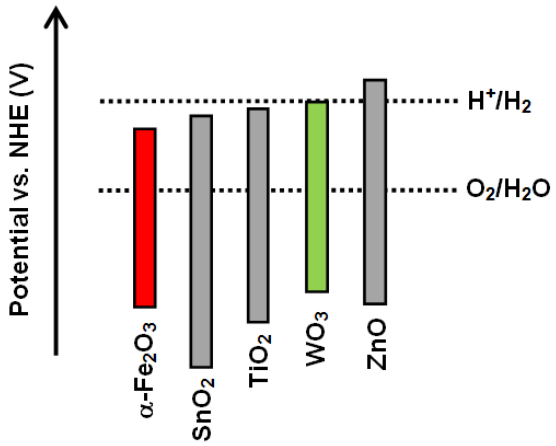

Figure 1-1 Nominal band alignment of materials investigated in this dissertation with respect to the water splitting redox couple. Color bars represents semiconductor bandgaps. Conduction band minima taken from maximum values in Reference 6.

The physical chemistry and optimization of these electrochemical reactions at the surface of a semiconductor is an entire-field within photoelectrochemistry. This dissertation does not generally consider the optimization of the kinetics of water oxidation and reduction reactions. These processes are addressed in the numerous reports which consider the deposition of catalysts on the surface of electrodes and photoelectrodes. Catalysts are especially effective for those systems whose efficiency is limited by the transfer of charge across the semiconductor/liquid interface.[7] For example it is suggested that the rate constant for electron transfer across the oxide-liquid interface is higher for transfer to O 2*p* orbitals than to metal 3*d* orbitals.[8] Consequently the efficiency of α-Fe_2O_3 is commonly enhanced by deposition of catalysts on the surface.

1.2.3 Oxides and electrode stability

A further requirement of photoelectrodes is that they remain chemically stable in operating conditions. Oxide materials are exclusively considered in this dissertation because oxides are one of the only material classes that remain chemically stable for the water oxidation process. In this section we provide a very brief introduction to the anodic decomposition of semiconductors.

In electrochemical processes involving semiconductors, there is often a competing dissolution reaction which requires consideration.[9] For a photoanode, we are primarily concerned with the anodic dissolution reaction, a valence band process. Gerischer[9] highlighted the various scenarios which promote semiconductor dissolution during electrochemical processes. For anodic dissolution these are generalized in Figure 1-2. If the standard potential for dissolution exists at potentials less than the valence band energy, the semiconductor is considered stable (Figure 1-2a). The semiconductor is considered unstable if the valence band edge exists at lower potentials than the decomposition reaction potential. Depending on the potential of the dissolution reaction with respect to the redox potential, the primary reason for instability can be kinetic or thermodynamic. For example, if the decomposition reaction potential is above the valence band but below that of the water oxidation reaction (Figure 1-2b), the decomposition is thermodynamically possible but probably not kinetically favorable. In contrast, if the decomposition potential is greater than both the valence band and the water oxidation potential (Figure 1-2c) the decomposition is thermodynamically favorable and thus the electrode is unstable. Oxides provide the greatest degree of chemical stability while retaining an ability to absorb visible light, as discussed above.

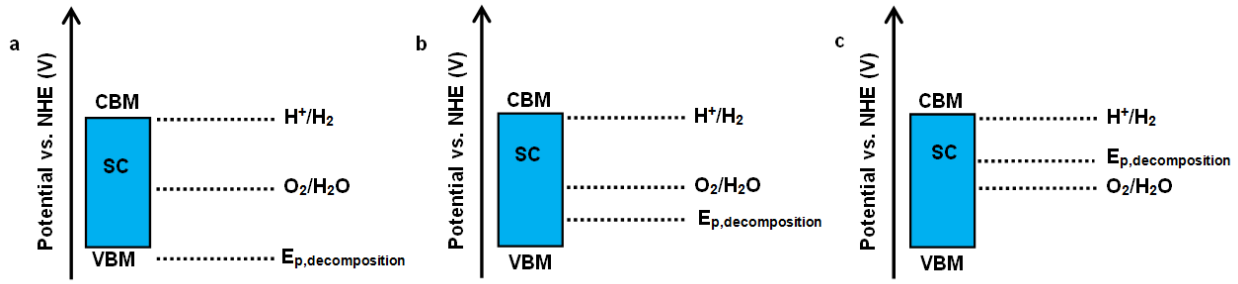

Figure 1-2 Generalized stability considerations for anodic dissolution for semiconductor electrochemistry. (a) stable electrode, (b) unstable electrode for kinetic reasons (c) unstable electrode for thermodynamic reasons. CBM is the conduction band minimum; VBM is the valence band maximum.

1.2.4 Optical absorption

Optoelectronic solar energy conversion devices rely on the efficient absorption and conversion of solar photons with a broad band of energies. For photovoltaics, this requires absorption of visible and infrared light. For photoelectrochemical water splitting cells, efficiency requires absorption and conversion of UV and visible light. Because the terrestrial solar photon flux is known, the theoretical efficiency of semiconductor photoanodes can be predicted based on criteria including the thermodynamic requirement for water splitting and the various expected loss mechanisms. [10] For example, a material with a bandgap of 3.2 eV (anatase TiO_2) has a theoretical solar to hydrogen efficiency of 1.3%, a material with a bandgap of 2.7 eV (WO_3) has a theoretical efficiency of 4.8%, and a material with a bandgap of 2.2 eV (α-Fe_2O_3) has a theoretical efficiency of 12.9%.[10] The dramatic increase in theoretical efficiency with decreasing bandgap results from the very small percentage of UV light available in the solar spectrum. This is made evident in Figure 1-3, which provides the terrestrial solar irradiance as a function of wavelength. Typical oxide semiconductor bandgaps are indicated by dashed vertical lines. The wavelength-integrated solar irradiance at energies exceeding the material bandgap (absorbed light) increases considerably for all visible-light active (approximately 400 to 800 nm) materials. This is the primary motivation for the intense study of α-Fe_2O_3,[11] which absorbs light up to approximately 600 nm.

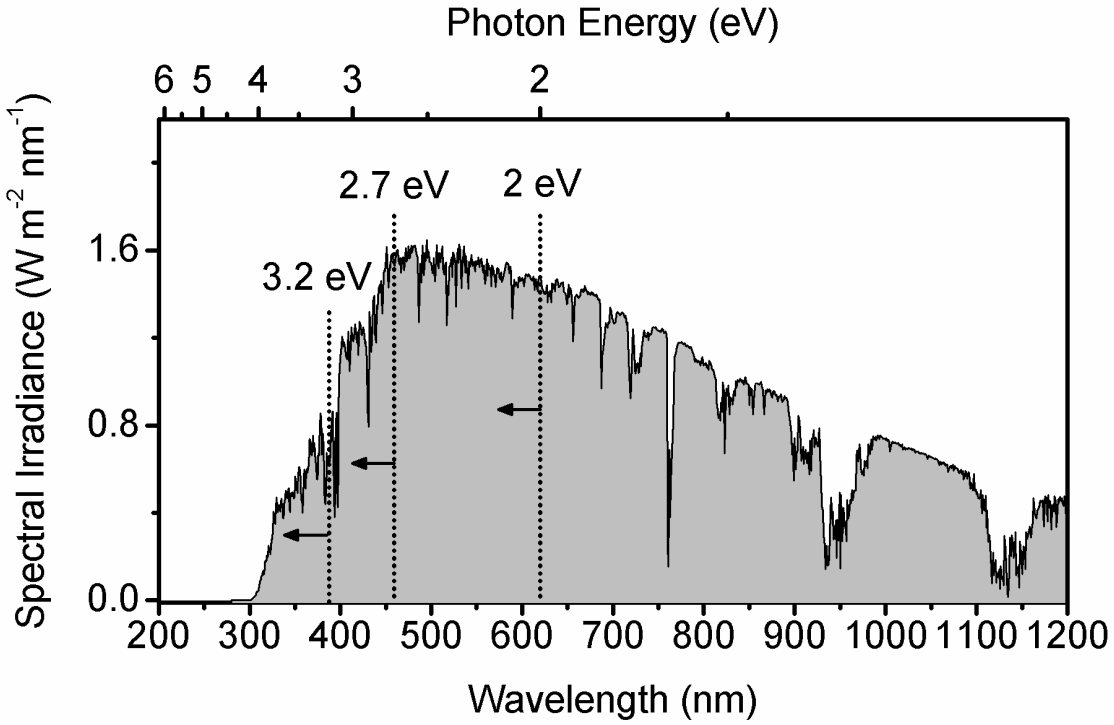

Figure 1-3 AM1.5 G solar spectrum with common oxide bandgap energies indicated with dashed vertical lines. 1.2.5 ASTM G-173-03 (International Standard ISO 9845-1, 1992).

The optical absorption of oxides can be tuned by altering their chemical composition. Chapter 4 for example demonstrates the introduction of transition metal impurities into a wide-bandgap post-transition-metal oxide, which serves to sensitize the material to visible light. In general, visible light sensitization of oxide materials can be achieved either by doping or alloying. Alloying and the discovery of new oxide materials is the most promising route, because it enables simultaneous optimization of band structure considerations, which relate to transport properties. Materials discovery is an exciting area of research within the field of photoelectrochemistry, and has yielded a number of interesting and promising studies.[12]

1.2.5 Operating mechanisms and semiconductor-liquid junctions

The operating mechanisms of a photoelectrolysis cell of the type which motivates the work in this report is presented in Figure 1-4. This diagram is constructed from principles outlined by Nozik and Memming in Reference 13 in their description of the physical chemistry of semiconductor-liquid junctions.

When placed in electrical contact with the electrolyte, the charges within the interfacial region redistribute such that the Fermi level between the two phases is equalized (Figure 1-4a, Fermi level drawn arbitrarily for this material). In operating conditions (Figure 1-4b) the system is perturbed by the energy of the incident photon flux and the application of an electrical bias. The absorption of photons and associated valence band to conduction band transition shifts the Fermi level in the semiconductor upward. Simultaneously, the applied anodic bias raises the Fermi

level in the metal above the H^+/H_2 potential. Band bending in the semiconductor increases to maintain the charge transfer rate.

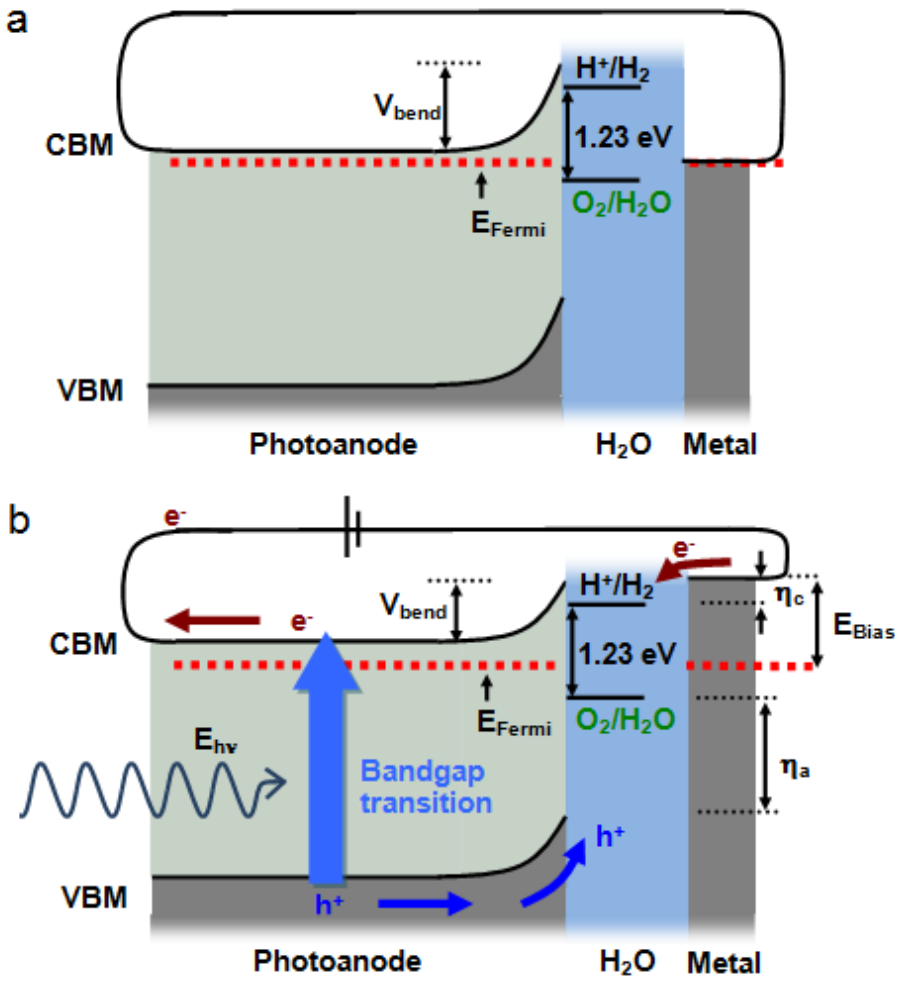

Figure 1-4 Schematic depicting the major processes involved in operation of a photoelectrolysis cell. (a) Equilibrium conditions in the dark and (b) non-equilibrium conditions, with light and application of anodic bias. η_a and η_c represent the overpotentials for the anodic and cathodic reactions, CBM is the conduction band minimum, VBM is the valence band maximum, e^- represents conduction band electrons, and h^+ represents valence band holes.

The electric field responsible for carrier separation at the semiconductor-liquid junction, reflected in the band banding in Figure 1-4, may be absent in systems where the photoelectrode possesses nanoscale feature dimensionality.[14] In systems of this type, under certain conditions, space-charge-limited current is not observed because majority carriers in the electrode can be effectively screened by charges in solution which are contained in the pores within the electrode structure. In this case, carrier transport occurs by diffusion, and the propensity to oxidize or reduce the electrolyte is determined by the interfacial kinetics and the band alignment of the semiconductor with respect to the redox couple. The photoresponse is determined by the rate of

reaction of the positive and negative charge carriers with the redox couple.[14] This has been explicitly demonstrated with nanocrystalline photoelectrodes, where *both n*- and *p*-type behavior can be observed, depending on the redox couple in the electrolyte. In response to an applied electric field, these systems have been described, in interpretations of transient absorption spectroscopy measurements, to shift from the equilibrium background density of conduction electrons.[15] All the materials examined in this dissertation behave as *n*-type anodes, suggesting that in all cases the oxidation of water is the preferred reaction at the semiconductor-liquid interface.

1.3 Tandem cells

High efficiency in solar energy conversion technologies relies generally on the absorption of a wide portion of the incident spectrum of solar light. Photoelectrochemical water splitting in a single absorber system, such as is discussed above, is established primarily by conversion of photons with energy greater than 2 eV, which is sufficient energy to drive the electrochemical reactions (+1.23 eV vs SHE for O_2/H_2O) as well as provide any needed overpotentials to the system. However, a significant portion of the total energy flux exists associated with photons with energies less than 2 eV. Researchers have proposed a number of promising tandem configurations, which involve placing multiple photoabsorbers in series to optimize the total energy conversion efficiency of the system.[16,17,18,19] In these configurations, lower-energy light not absorbed by the photoactive anode in the photoelectrolysis cell passes through the semi-transparent electrodes and irradiates a solar cell or photocathode. The purpose of the design is to provide additional potential to the system, which can be used to assist in overcoming the thermodynamic requirements discussed above. They are stand-alone systems, and can generate hydrogen without an external power source.

In each of these systems, the efficiency is limited by the performance of the photoanode, which either provides insufficient photocurrent or requires too large of an applied potential to operate efficiently. For example, Reference 17, which describes the use of a hybrid multijunction cell coupled to an oxide photoelectrode in a layered structure, indicates that performance can be limited by the ability of the oxide (such as WO_3) to current match with the in-line device, or by the high bias required for generation of current in the oxide (such as α-Fe_2O_3). Similar conclusions were drawn in Reference 18, which coupled the α-Fe_2O_3-based PEC cell to a series of dye-sensitized solar cells to achieve water splitting without an external power supply.

The research in this dissertation is motivated additionally by these tandem devices, which provide a potentially low-cost and practical configuration for sustainable hydrogen generation. The photoanode optimization and design considerations (namely, high photocurrent with low applied potential) are equally applicable when considered in the context of the tandem designs.

1.4 Experimental Techniques

1.4.1 Fabrication techniques

1.4.1.1 *Pulsed laser deposition*

Thin films are the simplest structure for semiconductor electrode materials deposited onto transparent conductive electrodes. Importantly, these structures provide an avenue for investigating the fundamental characteristics of electrodes because their geometries are easily represented in models. Pulsed laser deposition (PLD) is utilized in many studies within this dissertation as an enabling technology, which permits evaluation of a wide range of oxide materials and structures, especially thin films.

A typical PLD experiment involves installation of a substrate and target material, separated by several cm, into a vacuum chamber, which is subsequently evacuated to low pressure. For oxide deposition in this dissertation, O_2 gas is flowed into the chamber after attaining the base pressure; typical operating background O_2 pressures are ~ 3 mtorr. Deposition occurs by the collection of species generated by the pulsed laser ablation of the rotating target material. The substrate temperature during deposition in modulated through a resistance heater imbedded in the substrate holder block. The laser fluence is modulated by decreasing the high voltage supply to the laser and changing the spot size of the laser pulse incident on the target. A vacuum chamber suitable for the pulsed laser deposition of oxide photoelectrodes was constructed; a photograph of the completed chamber with major features highlighted is presented in Figure 1-5.

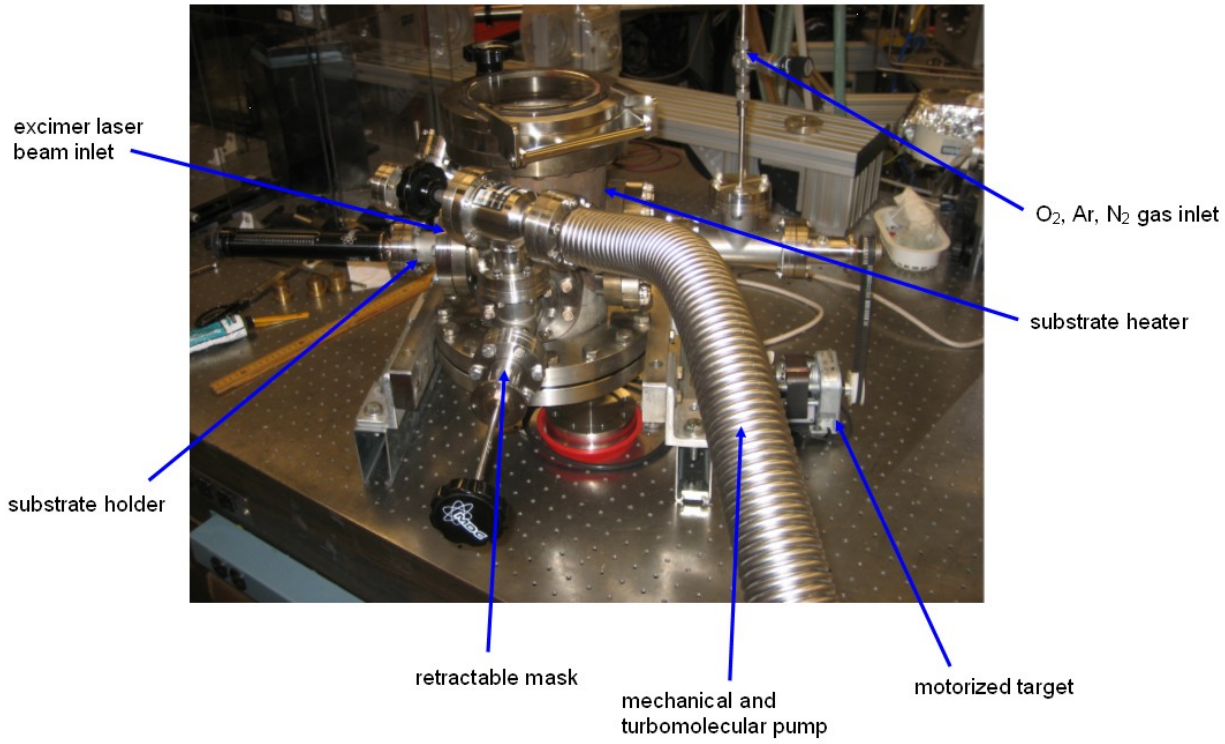

Figure 1-5 Vacuum chamber constructed for pulsed laser deposition of metal oxide photoelectrodes.

PLD is associated with a number of complex physical processes, which must be understood to some degree in order to produce a thin film with the desired properties. In particular, the laser-material interaction at the target and the laser ablation plasma and plume propagation are especially complex and nuanced areas, which are the subject of intense research.

Absorption of the laser pulse by the PLD target, and subsequent desorption or ablation of target material involves a competition between localized and delocalized energy transfer in the solid.[20] In this dissertation oxide films are deposited from pressed and polycrystalline metal oxide targets. The ablation mechanisms of these targets is expected to be quite complex, because the constituent oxides possess a wide range of degrees of electron-lattice coupling. From a functional point of view, it is known that the PLD target must be made as dense as possible to avoid exfoliation of large species from targets, which when incident on the substrate tend to create large particulates and disrupt film continuity. Avoidance of these features is further facilitated by the use of low laser pulse power densities, which limit the degree of hydrodynamic sputtering of micron-scale particulates.[21]

1.4.2 Characterization techniques

1.4.2.1 *Photoelectrochemistry*

1.4.2.1.1 Current-potential measurements

The primary technique used to evaluate photoelectrodes in this dissertation is the measurement of photocurrent under solar-simulated light irradiation. Specifically, electrodes are submerged into an aqueous electrolyte, prepared with prepared with 18.1 MΩ-cm water, contained in a pyrex cell fitted with a flat 3 mm-thick quartz window. An electrical contact is made to the electrode with a conductive silver paste and copper wire, which is encased in a glass pipet such that the wire is never exposed to the electrolyte during measurement. A masked-off, sealed region of constant area is irradiated with a 300 W Xe bulb solar simulator with adjustable power settings through an AM 1.5G filter (Oriel; 81092). The light intensity at the sample location in the photoelectrochemical cell is 100 mW cm^{-2} as measured by a power detector (Newport; 70284), unless otherwise specified. No correction is made for the optical absorption of the 4 cm of electrolyte between the quartz window and sample location. A potentiostat (Pine Instruments Bipotentiostat) is used to measure electrochemical data in a two- or three-electrode setup using a coiled Pt wire counter electrode and Ag/AgCl reference electrode. N_2 gas is continuously bubbled in solution and directly over the Pt counter electrode before and during the experiment to remove any dissolved O_2 and therefore suppress the reduction of dissolved O_2 at the counter electrode. For current-potential measurements, the potential scan is anodic (in the positive direction) and usually at a rate of 5 mV s^{-1}, with the light mechanically chopped every ten seconds.

It is important to note that the measured photocurrent does not necessarily correspond directly to hydrogen and oxygen gas generation (e.g. two electrons per H_2 molecule). So-called recombination current, capacitive current, and electrochemical dissolution processes could contribute to the magnitude of the measured current. The best way to establish the relationship between gas production and photocurrent is to directly measure gas evolution, however this

requires the optimization of the photoelectrochemical cell which is beyond the scope of this dissertation. Photocurrents therefore can be taken as an upper bound of hydrogen generating current.

1.4.2.1.2 Incident photon conversion efficiency

Photocurrent measurements under white light (solar-simulated) irradiation described above provide an important metric for understanding the overall performance of the photoelectrode. In order to obtain more detailed information on the electrode photoresponse, one measures the incident photon conversion efficiency (IPCE) or external quantum efficiency, which provides the spectral photoresponse of the photoelectrode under irradiation with monochromatic light. This measurement provides the number electrons in the external circuit generated per incident photon of fixed energy (within the bandpass of the monochromater). The IPCE is calculated as,

$$IPCE = \frac{J_p(\lambda)}{eE_s(\lambda)}, \tag{1-5}$$

where $E_s(\lambda)$ is the incident photon flux at λ, $J_p(\lambda)$ is the photocurrent measured at λ, and e is the elementary charge. IPCE measurements in this dissertation were performed on a commercial external quantum efficiency instrument from PV Measurements, Inc. A generalized schematic of the system is provided in Figure 1-6.

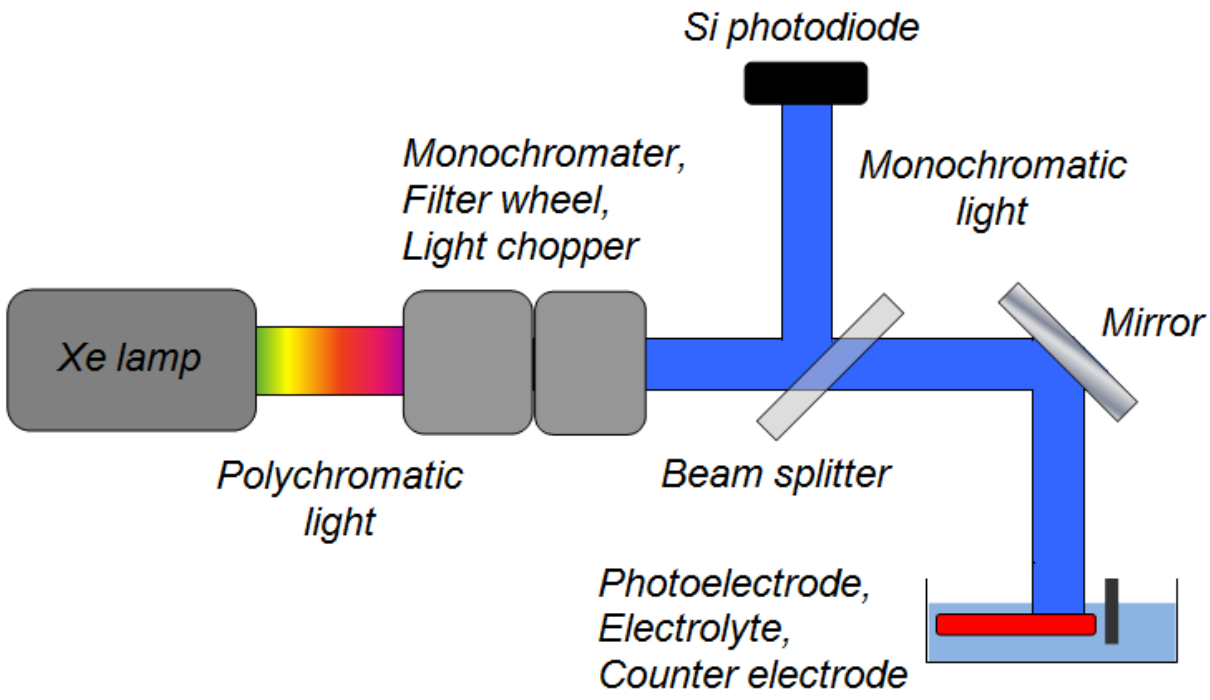

Figure 1-6 Generalized schematic of the external quantum efficiency system, illustrating the primary pieces of hardware required for the measurement.

Briefly, a Xenon arc lamp generates polychromatic (white) light, which is passed through a monochromater with a bandpass FWHM of 5 nm. A filter wheel in the beam path blocks second order, low energy light, and a light chopper with variable frequency is present to enable measurement of both light and dark currents. The monochromatic light passes through a beam splitter, which diverts a portion of the incident beam to a NIST-calibrated Si photodiode, which measures the incident photon flux. The remaining portion of the beam strikes a mirror and subsequently the surface of the photoelectrode, which is immersed in the aqueous electrolyte. A Pt counter electrode is also present in the electrolyte to complete the circuit. The system is capable of measuring the light and dark current, in the presence or absence of an external bias, and computes the external quantum efficiency.

1.4.2.2 *Spectroscopic ellipsometry-reflectometry and the WO_3 system*

Chapters 3 and 5 contain studies related to the determination of the optical functions of oxide materials, using spectroscopic reflectometry and/or ellipsometry. In this section we briefly present the optical characterization of WO_3 thin films, to provide a working example of the type of characterizations provided in this dissertation. Similar analyses were performed on α-Fe_2O_3 and ZnO within this dissertation. This section also provides an indication of the effect the selection of dispersion relation has on the simulated optical functions of oxide materials.

Quantifications of the optical functions of tungsten(VI) oxide (WO_3) films are of critical importance for the many optoelectronic device technologies into which they are integrated. Electrochromic devices, which modulate optical absorption of multi-layered structures upon application of an electric field, use WO_3 films for cathodic coloring.[22] In photoelectrochemical solar water splitting cells, WO_3 photoanodes efficiently oxidize water under solar irradiation. This functionality originates from the material's long minority carrier diffusion length,[23] large oxidative overpotential associated with its low valence band edge comprised mainly of O 2*p* orbitals,[24] and superior charge transfer kinetics with the electrolyte compared to other candidate semiconductor oxides.[8] For this application, the moderately large bandgap of WO_3 (measured from 2.5 to 3.2 eV)[25] and its chemical stability in acidic media permit its integration into tandem PEC-PV devices.[16,17]

WO_3 thin films, nominally 70 nm thick, were fabricated on Si (001) substrates by pulsed laser deposition in an oxygen enivornment whose pressure was regulated by a mass-flow controller to P_{oxygen} = 3 mtorr. The substrate temperature was maintained at 100 ºC during deposition using a resistive heater embedded in the substrate holder. This section considers the optical properties of two types of films: an as-deposited WO_3 film and a film subsequently annealed in air at 700 ºC (8.6 ºC min^{-1} ramp; 1 hr soak).

Optical measurements were performed *ex situ* in atmospheric conditions on a combined ellipsometer-reflectometer (Scientific Computing International Filmtek Par3000SE). The system is a rotating compensator design, which permits mesurements with high signal-to-noise ratios. It simultaneously measures the ellipsometric parameters psi (Ψ) and delta (Δ) as well as absolute values for 0º (normal incidence) reflectance and 70º (oblique angle incidence) reflectance, which are collected by measuring with respect to a reflectance spectrum of a known reference sample (Si). Ellipsometric and 70º reflectance data were collected from 330 nm to 1050 nm; 0º

reflectance data were collected from 240 nm to 1050 nm. The ellipsometric data can be represented by the complex reflectance ratio,

$$\rho = \frac{r_p}{r_s} tan\Psi e^{i\Delta}, \quad (1\text{-}6)$$

The system's multi-layer film analysis software (FilmTek) allows simultaneous simulation a multi-layer structure's optical response over the entire spectral range of interest. The multilayer structure employed to simulate the response consisted of a Si substrate and SiO_2 surface layer, whose refractive indices were taken from literature values, following by the WO_3 thin film and its surface layer. The surface layer was modeled with the Bruggeman effective medium approximation (EMA) and consisted of 50% WO_3 and 50% void. The software uses regression analysis to minimize an error function associated with the fit. The software couples the features of the effective medium layer to a computation of surface roughness scattering effects, which are then included in the reflectance simulations.

The optical functions of WO_3 thin films have been approximated previously using a number of models, including multiple Lorentz oscillators,[26,27,28] Lorentz oscillators modified to include Gaussian broadening,[29] and a Lorentz oscillator modified to include the Tauc joint density of states[30] (the Tauc-Lorentz parameterization[31]). In this study the films are analyzed by the Tauc-Lorentz parameterization as well as with a proprietary model from Scientific Computing International (SCI model[32]).

The SCI parameterization differs in a few significant aspects from the Tauc-Lorentz equations described above. In the Tauc-Lorentz parameterization, the bandedge is approximated by the Tauc joint density of states, which calls for a quadratic term. Rather than the constant energy value E_g, after which ε_2 is forced to zero, the SCI model instead uses a damping term that is itself a function of energy. Consequently the band edge dispersion is approximated by a higher order polynomial, which has potential to more realistically represent the band edges of real systems. In this aspect is relates to the Cody-Lorentz paramterization,[33,34] which simulates intraband Urbach tails using an exponential term in the expression for ε_2 over a transition energy range near the band edge. In addition, in the Tauc-Lorentz parameterization the oscillators are decoupled. In the SCI model the oscillators are coupled mathematically, through the damping term mentioned above.

In the Tauc-Lorentz and SCI models, the real and imaginary parts of the dielectric function are related by solution of the Kramers-Krong (KK) integral transformations, for which there are analytical solutions in both cases. The models are therefore considered accurate over the entire spectral range. The measured and simulated 0º and 70º reflectance as well as the ellipsometric parameters Ψ and Δ for a representative WO_3 film is presented in Figure 1-7. At lowest mean square error obtained, a near-perfect fit is found for the entire spectral range for both parameterizations.

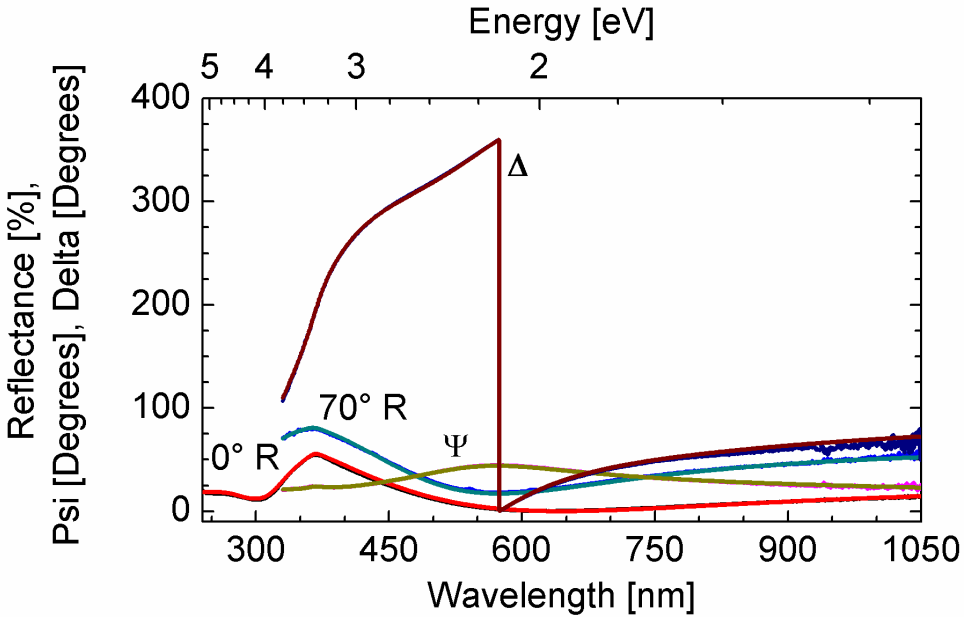

Figure 1-7 Measured optical responses of as-deposited WO_3 thin film, with overlapping simulated curves. Psi (Ψ) and delta (Δ) are the ellipsometric parameters; 0° R refers to reflectance with 0º (normal) incidence angle; 70° R refers to reflectance with 70º incidence angle.

The refractive indices of WO_3 films are provided in Figure 1-8. The top panels show values determined from best fits using the Tauc-Lorentz relations; bottom panels show values determined using the SCI relations. Each panel contains two plots: index values for the as-deposited film and those for the film annealed at 700 ºC.

.

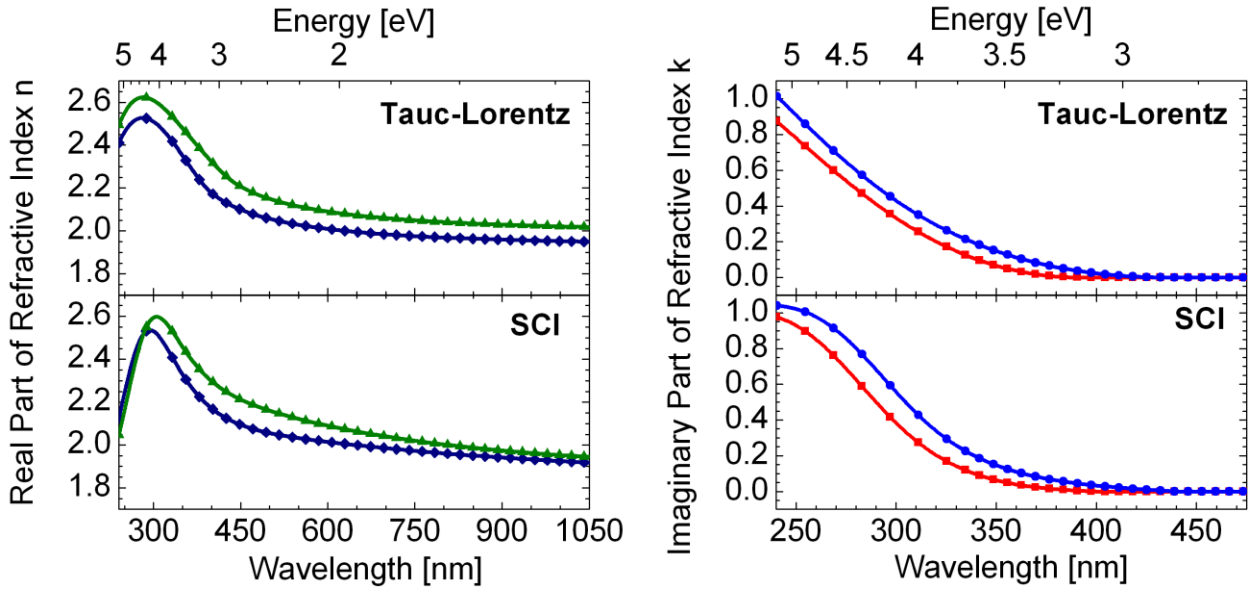

Figure 1-8 (a) Real part of the refractive index of WO_3 for as-deposited film (navy diamonds) and film annealed in air at 700 C (green triangles). Every one-hundredth point plotted (b) Imaginary part of the refractive index of WO_3 for as-deposited film (blue circles) and film annealed in air at 700 °C (red squares). Every thirtieth point plotted. Top panels show values determined from Tauc-Lorentz parameterization; bottom panels show values determined from SCI parameterization.

The refractive indices for the two methods are very similar, as expected, but differ in terms of line shape. This is most likely the result of the differing band edge dispersion approximations used in the two parameterizations. The data also show that an effect of the high-temperature annealing process is to reduce the energy of the primary optical transition probed in these measurements, a result which is indicated by optical functions produced from both parameterizations.

1.4.2.3 *Synchrotron-based soft x-ray spectroscopy*

Chapters 5 and 6 of this dissertation contain comprehensive electronic structure characterization of materials by synchrotron-based soft x-ray spectroscopy, performed at the Advanced Light Source. The following sections provide a very brief introduction to the primary techniques utilized in these studies, to provide sufficient context for the analysis of results in Chapters 5 and 6. The physics involved in core level spectroscopy is a large field and an in-depth discussion is beyond the scope of this dissertation; readers are referred to the literature for a detailed description, for example in Reference 35.

1.4.2.3.1 Soft x-ray absorption spectroscopy

In the soft x-ray absorption process (x-ray absorption spectroscopy, XAS), a core electron is excited through the electric dipole transition to a near-threshold state.[36] The spectra generated yield information relating to the symmetry-projected partial density-of-states of the excited state. The large energy separation among core levels gives the technique elemental selectivity, the participation of valence electrons yields chemical state sensitivity, and the dipole nature of the

transitions provides symmetry information. The probe is localized to one specific atomic site, around which the electronic structure is reflected as a partial density-of-states contribution.

The primary processes involved in O *K*-edge absorption are illustrated in Figure 1-9a. This schematic is based on discussions in Reference 35. The O *K*-edge absorption spectrum provides a representation of the O 2*p* unoccupied density-of-states through excitation of core O 1*s* electrons. The final state is coupled to the original state by the dipole selection rule.[37] The change in angular momentum quantum number (ΔL) must be ±1; only the oxygen *p* character is probed.

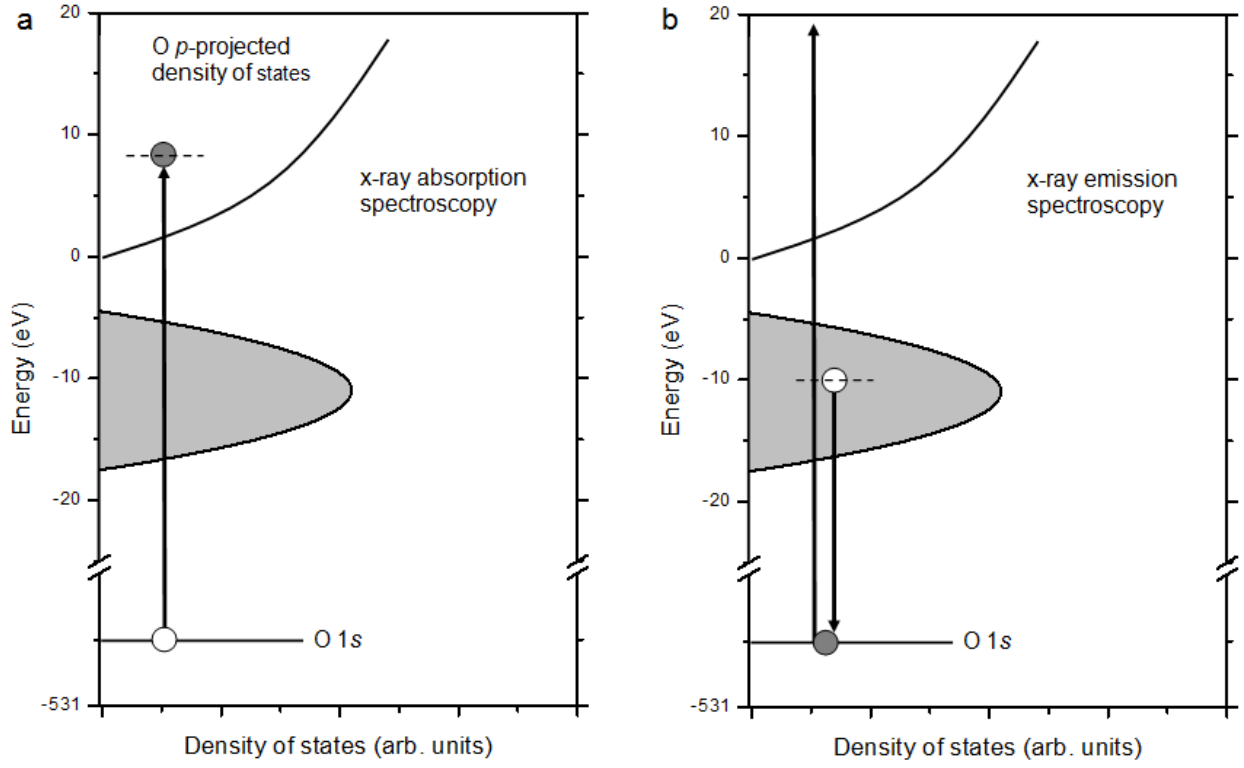

Figure 1-9 Schematic diagram of the density of states of an oxide and the O *K*-edge x-ray absorption process (a) and the normal x-ray emission process (b).

O *K*-edge spectra provide important information on interfacial metal sites relevant to this application, because in these electrodes, above the Fermi level empty bands are predominantly metal weight hybridized with O 2*p* character. The existence of these transitions in itself is an indication of the partially covalent bonding in these materials.[38] A typical XAS spectrum for anatase TiO_2 is provided in Figure 1-10. The intensity from about 530 to 536 eV is attributed to the Ti 3*d* band, and the higher energy region is attributed to the Ti 4*sp* band. The breadth of this region is a measure of the degree of covalency in the material. The absence of signal below the Ti 3*d* indicates a gap in the density of states; the intensity around 530 eV reflects the conduction band minimum of TiO_2. The strength of this technique for the study of oxide electrodes is illustrated in Chapter 6, where the interface between TiO_2 and a transparent conductive oxide is examined. This interface is associated with the electron conduction pathway in numerous

photoelectrochemical and optoelectronic devices, including solar water splitting cells, solar cells, and certain light emitting diodes. XAS probes the unoccupied electronic states above the Fermi level: aspects of the electron conduction environment can therefore be evaluated with this technique.

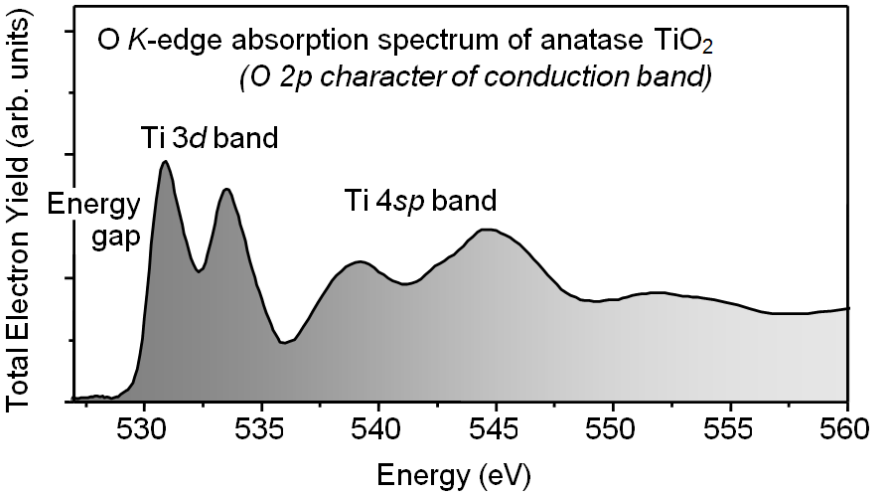

Figure 1-10 Oxygen *K*-edge x-ray absorption spectrum for anatase TiO_2, illustrating the 3*d* and 4*sp* bands of Ti hybridized with oxygen 2*p* character.

1.4.2.3.2 Soft x-ray emission spectroscopy

Soft x-ray emission spectroscopy (XES) is in contrast a second order process (photon-in, photon-out). Upon irradiation with soft x-rays with energies sufficient to promote a core electron to the continuum (normal x-ray emission spectroscopy, Figure 2-3b) or near to the threshold as in XAS (resonant x-ray emission spectroscopy). Fluorescence photons are detected in this case with a high-resolution spectrograph. The technique begins with a core hole and results with a valence hole, and therefore enables evaluation of the occupied electronic states in the material.

1.5 References for Chapter 1

1. N. S. Lewis and D. G. Nocera, *Proc. Nat. Acad. Of Sciences* **103,** 15729 (2006).

2. R. E. Blankenship, D. M. Tiede, J. Barber, G. W. Brudvig, G. Fleming, M. Ghirardi, M. R. Gunner, W. Junge, D. M. Kramer, A. Melis, T. A. Moore, C. C. Moser, D. G. Nocera, A. J. Nozik, D. R. Ort, W. W. Parson, R. C. Prince, and R. T. Sayre, *Science* **332**, 805 (2011).

3. S. Styring, *Faraday Discuss.* **155**, 257 (2012).

4. N. S. Lewis, *MRS Bulletin* **32**, 808 (2007)

5. M. G.Walter, E. L Warren, J. R. McKone, S. W. Boettcher, Q. Mi, E. A. Santori, and N. S. Lewis, *Chem. Rev.* **110**, 6446 (2010)..

6. J. A. Glasscock, PhD Thesis, University of New South Wales, Australia, 2008, 1-220.

7. J. Sun, D. K. Zhong, and D. R. Gamelin, *Energy Environ. Sci.* **3**, 1252 (2010).

8. M. P. Dare-Edwards, J. B. Goodenough, A. Hamnett, and P. R. Trevellick, *J. Chem. Soc., Faraday Trans. 1* **79**, 2027 (1983).

9. H. Gerischer, *J. Electroanal. Chem.* **82**, 133 (1977).

10. A. B. Murphy, P. R. F. Barnes, L. K. Randeniya, I. C. Plumb, I. E. Grey, M. D. Horne, and J. A. Glasscock, *Int. J. Hydrogen Energy* **31**, 1999 (2006).

11. K. Sivula, F. Le Formal, and M. Grätzel, *ChemSusChem* **4**, 432 (2011).

12. J. E. Katz, T. R. Gingrich, E. A. Santori, and N. S. Lewis, *Energy Environ. Sci.* **2**, 103 (2009).

13. A. J. Nozik and R. Memming, *J. Phys. Chem.* **100**, 13061 (1996).

14. M. Grätzel, *Nature* **414**, 338 (2001).

15. S. R. Pendlebury, M. Barroso, A. J. Cowan, K. Sivula, J. Tang, M. Grätzel, D. Klug, and J. R. Durrant, *Chem. Commun.* **47**, 716 (2011).

16. B. D. Alexander, P. J. Kulesza, I. Rutkowska, R. Solarska, and J. Augustynski, *J. Mater. Chem.* **18**, 2298 (2008).

17. E. L. Miller, R. E. Rocheleau, and X. M. Deng, *Int. J. of Hydrogen Energy* **28**, 615 (2003).

18. J. Brillet, M. Cornuz, F. Le Formal, J.-H. Yum, M. Grätzel, and K. Sivula, *J. Mater. Res*. **25**, 17 (2010).

19. H. Wang, T. Deutsch, and J. A. Turner, *J. Electrochem. Soc.* **155**, F91 (2008).

20. R. F. Haglund, Experimental methods in the physical sciences: Volume 30 Laser ablation and desorption, Academic Press, San Diego, 15-138 (1998).

21. D. B. Chrisey and G. K. Hubler, Pulsed laser deposition of thin films, Wiley-VCH (2003).

22. C. G. Granqvist, E. Avendano, and A. Azens, *Thin Solid Films* **442,** 201 (2003).

23. M. A. Butler, *J. Appl. Phys.* **48**, 1914 (1977).

24. H. H. Kung, H. S. Jarrett, A. W. Sleight, and A. Ferretti, *J. Appl. Phys.* **48**, 2463 (1977).

25. B. D. Alexander and J. Augustynski, in *On Solar Hydrogen and Nanotechnology*, edited by L. Vayssieres (Wiley, Singapore, 2009), pp. 333-347.

26. Y. Yamada, K. Tajima, S. Bao, M. Okada, K. Yoshimura, and A. Roos, *J. Appl. Phys.* **103**, 063508 (2008).

27. Y. Yamada, S. Kawaji, S. Bao, M. Okada, M. Tazawa, K. Yoshimura, and A. Roos, *Thin Solid Films* **515**, 3825 (2007).

28. J. S. Hale, M. DeVries, B. Dworak, and J. A. Woollam, *Thin Solid Films* **313-314**, 205 (1998).

29. K. von Rottkay, M. Rubin, and S. -J. Wen, *Thin Solid Films* **306**, 10 (1997).

30. I. Valyukh, S.Green, H. Arwin, G. A. Niklasson, E. Wäckelgård, and C. G.Granqvist, *Sol. Energy Mat. & Sol. Cells* **94**, 724 (2010).

31. G. E. Jellison, Jr and F. A. Modine, *Appl. Phys. Lett.* **69**, 371 (1996).

32. E. Zawaideh, *U S. Pat*., **5 889 592**, 1999.

33. A. S. Ferlauto, G. M. Ferreira, J. M. Pearce, C. R. Wronski,R. W. Collins,, Xunming Deng, and Gautam Ganguly, *J. Appl. Phys.* **92**, 2424 (2002).

34. J. Price, P. Y. Hung, T. Rhoad, B. Foran, and A. C. Diebold, *Appl. Phys. Lett.* **85**, 1701 (2004).

35. F. de Groot and A. Kotani, *Core Level Spectroscopy of Solids* (CRC Press, Boca Raton, FL, 2008).

36. F. J. Himpsel, *Phys. Status Solidi* B **248**, 292 (2011).

37. F. M. F. de Groot, M. Grioni, J. C. Fuggle, J. Ghijsen, G. A. Sawatzky, and H. Petersen, *Phys. Rev. B* **40**, 5715 (1989).

38. M. Abbate, F. M. F. de Groot, J. C. Fuggle, A. Fujimori, O. Strebel, F. Lopez, M. Domke, and G. Kaindl, G. A. Sawatzky, M. Takano, Y. Takeda, H. Eisaki, and S. Uchida, *Phys. Rev. B* **46**, 4511 (1992).

2 Doped, porous iron oxide films and their optical functions and anodic photocurrents for solar water splitting

Chapter 2 is an adaptation of a published article:

C. X. Kronawitter, S. S. Mao, and B. R. Antoun, Doped, porous iron oxide films and their optical functions and anodic photocurrents for solar water splitting, *Appl. Phys. Lett.* **98,** 092108 (2011)

The majority of the work in this chapter was supported by Sandia National Laboratories. Sandia National Laboratories is a multi-program laboratory managed and operated by Sandia Corporation, a wholly owned subsidiary of Lockheed Martin Corporation, for the U.S. Department of Energy's National Nuclear Security Administration under contract DE-AC04-94AL85000.

2.1 Abstract for Chapter 2

The fabrication and morphological, optical, and photoelectrochemical characterization of doped iron oxide films is presented. The complex index of refraction and absorption coefficient of polycrystalline films are determined through measurement and modeling of spectral transmission and reflection data using appropriate dispersion relations. Photoelectrochemical characterization for water photo-oxidation reveals that the conversion efficiencies of electrodes are strongly influenced by substrate temperature during their oblique-angle physical vapor deposition. These results are discussed in terms of the films' morphological features and the known optoelectronic limitations of iron oxide films for application in solar water splitting devices.

2.2 Introduction

Alpha-phase iron(III) oxide (hematite, α-Fe_2O_3) is an earth-abundant transition metal oxide compound that possesses many of the requisite characteristics for employment in efficient and scalable solar energy conversion technologies. It is inexpensive, non-toxic to humans, absorbs ultraviolet and high energy visible light, is electrochemically stable in a wide range of conditions, and its valence band edge is appropriately positioned to accept charges for the oxidation of water. It can function as a photoactive electrode material in photoelectrochemical (PEC) cells for solar energy conversion, most notably several promising tandem designs for solar hydrogen generation.[1,2] Its implementation into solar energy conversion devices presents some interesting technical challenges, mainly associated with its notoriously poor electronic transport properties (e.g.$\mu_{electron} < 0.1$ cm^2 V^{-1} s^{-1} [3]; $l_{diffusion,hole} \sim$ 2-4 nm[4]). Consequently the general strategy employed toward fabrication of efficient α-Fe_2O_3 photoelectrodes has been to simultaneously dope the lattice and to reduce the physical dimensions of the electrode structure to more nearly match the hole diffusion length. These efforts have been fruitful and yield very promising results; research into doped, nanostructured α-Fe_2O_3 water splitting photoanodes has recently been comprehensively examined in Reference 5.

One possible fabrication route to structures of this type is their oblique-angle or glancing-angle physical vapor deposition, the benefits of which have been established in the literature[6]. These techniques have been explored recently for photoelectrochemical and photocatalytic applications of TiO_2,[7] α-Fe_2O_3,[8] ZnO,[9] WO_3,[10] and composites thereof,[11] all of which are important solar water splitting materials. The typical motivation behind the unconventional geometry is the utilization of film growth shadowing phenomena resulting from ballistic species transport to the substrate, which can affect a nanostructured morphology. Engineering films by this technique is therefore particularly relevant to the study of iron oxide-based photoelectrodes because it enables fabrication of films with the aforementioned required physical properties (appropriate chemical composition and nanoscale morphology). This work is intended to contribute to the growing literature dedicated to the study of α-Fe_2O_3-based photoelectrodes for solar energy conversion, as well as to that of the oblique angle physical vapor deposition of metal oxides in general.

In this study, films were deposited onto conductive SnO_2:F-coated glass (FTO) and SiO_2 substrates in an oxygen environment at a moderate vacuum pressure of 4 mtorr. Deposition occurred from species ablated from a Fe_2O_3:TiO_2 (2.5 wt% TiO_2) target by approximately 130,000 shots from an excimer laser (Lambda Physik), with a laser fluence of ~1mJ/cm^2 on the target surface. Although the exact nature of resulting Ti incorporation into the films' crystal lattice was not studied, film composition analysis by x-ray fluorescence (50 kV Cu Kα radiation, Xradia) indicates the Ti content in the films is 2.25 atomic percent. The substrate was positioned at an angle of 49° from the target normal.[12] The importance temperature-related effects for this material system has been noted in the literature,[13] consequently three deposition substrate temperatures were examined (23 °C, 100 °C, 300 °C), and all samples were subsequently heat treated in air at 450 °C for 2 hrs before characterization. Adatom surface diffusion is an activated process and depends exponentially on temperature[14] – it is expected that depositions employing low substrate temperatures produce porous films with little structural organization, while those using high temperatures produce dense films with greater structural quality. Scanning electron microscopy images in Figure 2-1a,c of a sample deposited at 300 °C confirm that when species arriving at the substrate possess sufficient thermal energy for diffusion, a dense, rough, polycrystalline sample is produced. When the substrate is kept at 23 °C surface diffusion is quenched and a nanostructured (porous) morphology is attainable (Figure 2-1b,d).[12] Films deposited at 100 °C appeared in micrographs to have an intermediate level of porosity (not shown). The cross-sectional views indicate the films develop through the columnar growth mode,[14] which is expected to minimize the density of grain boundaries along the electronic conduction path normal to the substrate.

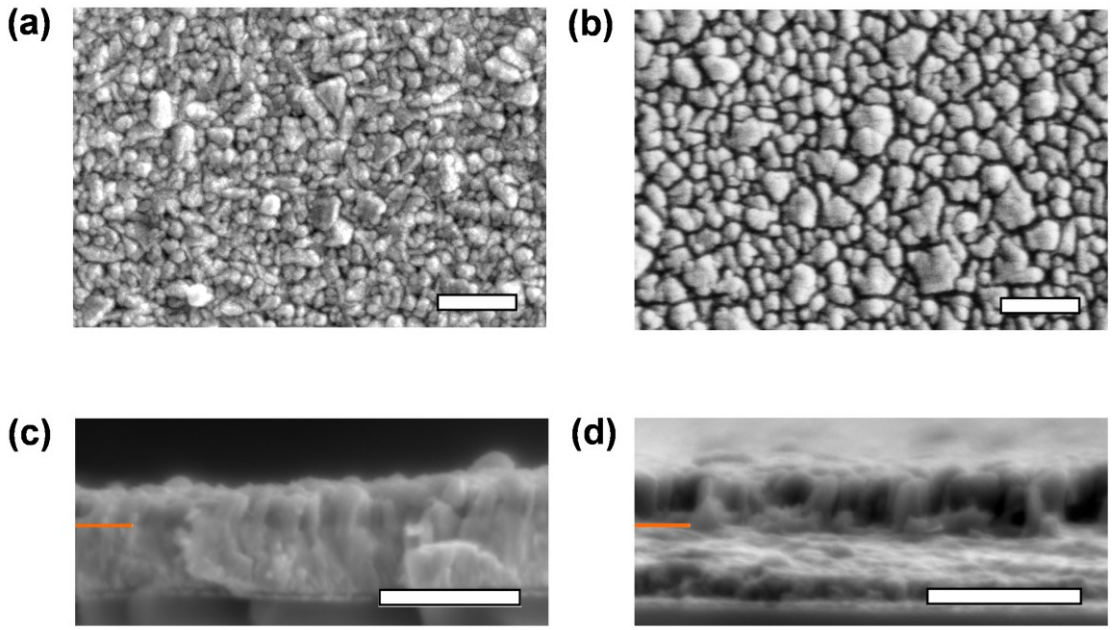

Figure 2-1 Scanning electron micrographs of films deposited with low and high substrate temperatures: (a) top-down view of 300 °C sample; (b) cross-sectional view of 300 °C sample; (c) top-down view of 23 °C sample; (d) tilted cross-sectional view of 23 °C sample. All white scale bars indicate 1 μm. Orange lines highlight film/substrate interfaces.

2.3 Optical properties

The optical properties of films were analyzed by measurement and subsequent modeling of spectral normal transmission and 0 (normal) and 70 degree specular reflection data using a thin film metrology system and its multi-layer film analysis software (FilmTek 3000 PAR SE). During deposition a small 0.5 mm thick single crystal SiO_2 substrate was mounted onto the FTO substrate surface at a location approximately 1 cm from the area later probed by PEC measurements. The measured quantities for the 300 °C sample are presented in Figure 2-2a. The sample was modeled as a three layer substrate/film/surface roughness structure as shown Figure 2-2b, and a regression analysis was performed utilizing the Cauchy dispersion[15] for the substrate, the Tauc-Lorentz dispersion relation[16] for the film, and the Bruggeman[17] EMA relation for surface roughness (modeled values indicated by lines in Figure 2-2a).[12] This analysis yielded a correlation coefficient of $R^2 = 0.995$ and predicts a film thickness of 303.5 nm and a surface roughness thickness of 34.7 nm, which is consistent with the microscopy image in Figure 2-1c. The resultant modeled optical data correspond to the complex index of refraction displayed in Figure 2-3a. These index magnitudes are relatively consistent with previous estimates for those of Fe_2O_3:Ti[18] and reflect the known optical transitions of α-Fe_2O_3 between 1.9 eV to 2.2 eV. Figure 2-3b presents the absorption coefficient as calculated from the extinction coefficient in Figure 2-3a; these values suggest that several hundred nanometers of material are required for

complete optical absorption of longer wavelength light. The disparity between this quantity and the minority carrier diffusion length in α-Fe_2O_3 is the primary obstacle for its technological implementation in PEC cells for solar energy conversion. Similar analyses of several locations on the FTO substrate indicate that over the 1 cm^2 probed by PEC measurements, the thickness gradient does not exceed ~20 nm/cm.

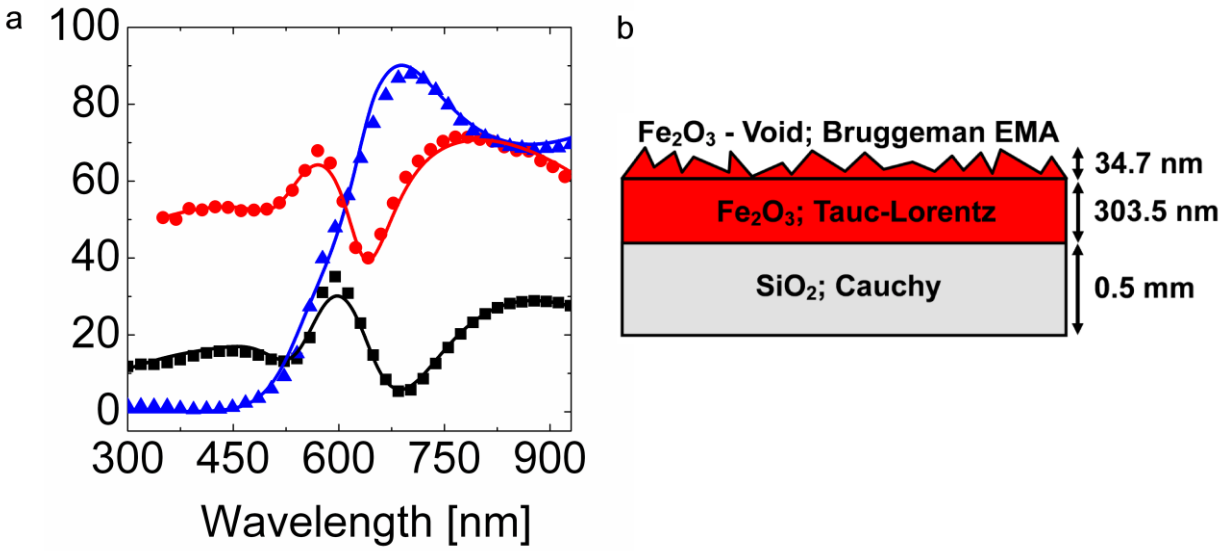

Figure 2-2 Optical characterization of film deposited on SiO_2 at 300 °C: (a) measured spectral normal transmission (blue triangles), 0° reflection (black squares), and 70° reflection (red circles). Every fortieth data point plotted for clarity. Simulated values are indicated by overlapping solid lines. (b) Multi-layer structure used as model for simulation of optical functions, with final determined values for layer thickness included.

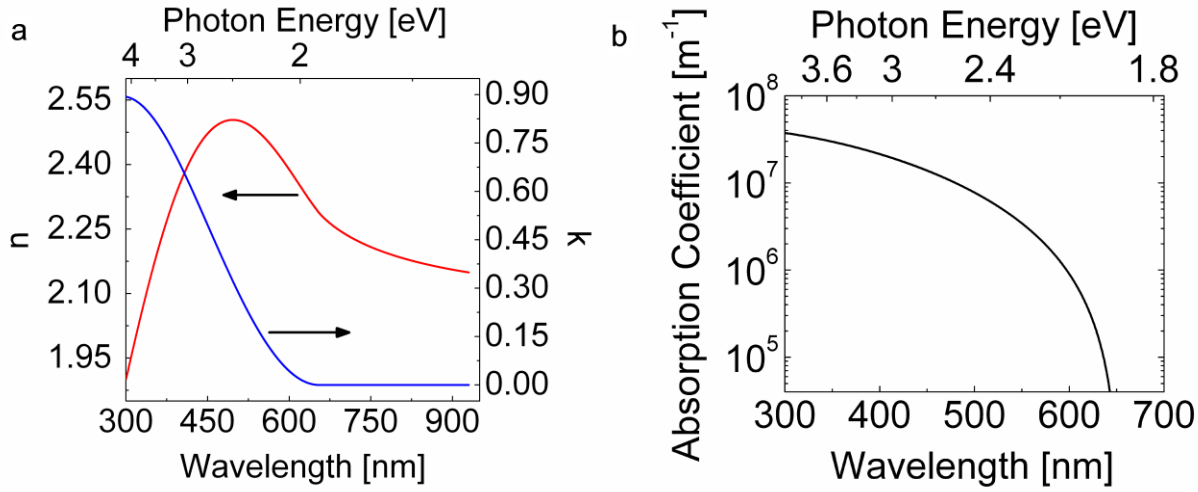

Figure 2-3 (a)Complex index of refraction $\tilde{n} = n + ik$ corresponding to the model presented in Figure 2-2a. (b) Absorption coefficient as calculated from the extinction coefficient in (a).

Photocurrent-potential curves (linear sweep voltammagrams) for films employed as working electrodes in a three electrode PEC cell fitted with a quartz window are shown in Figure 2-4a (Xe lamp solar-simulated light, Newport). There is a striking increase of anodic photocurrent magnitude with increasing substrate deposition temperature. The photocurrent magnitudes are more clearly indicated by the amperometric current-time curves displayed in Figure 2-4b, which show over an order of magnitude photocurrent range among the samples. The spectral characteristics of these trends are shown in Figure 2-4c with two-electrode incident photon conversion efficiency (IPCE) data, obtained with the use of a monochromator (5 nm FWHM bandwidth, 10 nm interval) and measurement of photon flux with a NIST-calibrated silicon photodiode. These data are compared in Figure 2-4c to the spectral absorptance, calculated from the absorption coefficient and film thickness as indicated in the right axis label. The discussion that follows elaborates upon the relationships among these quantities.

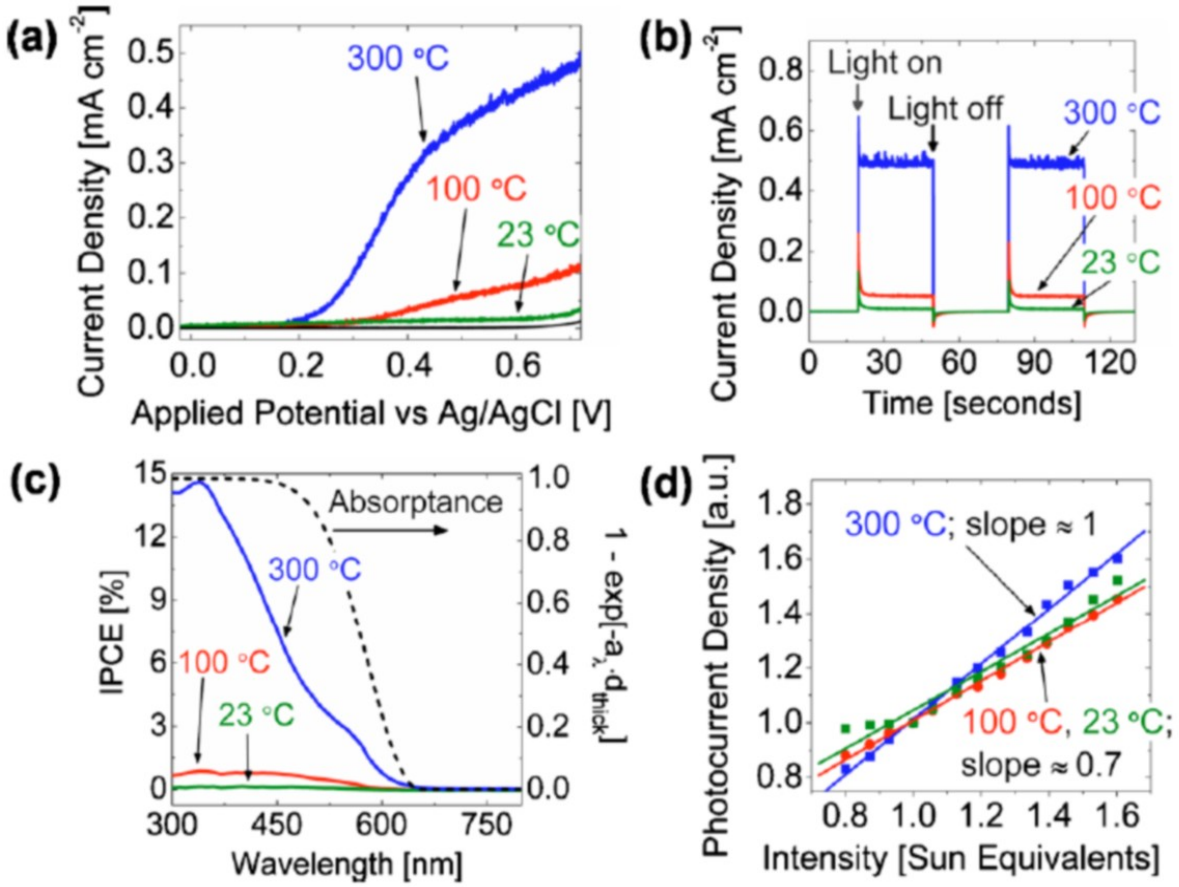

Figure 2-4Photoelectrochemical performance in 0.1 M NaOH aqueous electrolyte (pH=13) (a) Photocurrent-potential curves for samples deposited at 23 °C (green line), 100 °C (red line), and 300 °C (blue line) irradiated on the back side by 100 mW cm^{-2} AM 1.5 G-filtered solarsimulated light. (b) Current-time curves at 0.6 V vs Ag/AgCl with the same optical conditions as (a) but irradiated on the front side. (c) Incident photon conversion efficiency for front-side irradiation in two-electrode setup with an applied bias of +1 V vs counter electrode, plotted with absorption coefficient of 300 °C sample. (d) Photocurrent data collected at 0.6 V vs Ag/AgCl for 13 irradiation intensities with linear interpolations among data as described in the main text.

Examination of the temperature-photocurrent-irradiation intensity relationships for the samples provides additional information. Figure 2-4d shows the photocurrent density-intensity dependence of samples normalized by their respective photocurrents at 1 sun-equivalent irradiation. Linear interpolations are provided because the production of free electrons is directly proportional to light intensity.[19] The slopes of linear fits ($R^2 > 0.958$) to these data (1.01±0.02 for 300 °C, 0.72±0.01 for 100 °C, and 0.70±0.04 for 23 °C) are a measure of the efficiencies with which the structures are able to convert additional photon flux into current density in the external circuit.

The initial interpretation of this photocurrent-deposition temperature dependence acknowledges the poor electronic transport properties of n-type α-Fe_2O_3.[4] In the analysis that follows, it is assumed that the surface properties and consequently kinetics for water oxidation among the films are identical. This assumption seems reasonable considering their near-identical fabrication procedure and materials. The function of an n-type photoanode in a cell of this type is to generate and transport to the semiconductor-electrolyte interface holes with sufficient electrochemical potential to drive the oxygen evolution reaction. Electrons must be transported to the back contact where they enter the external circuit to participate in an electrochemical reduction reaction (e.g. proton reduction for H_2 generation). Considering that the reciprocal of the absorption coefficient (Figure 2-2d) is equal to the mean light penetration depth in a homogeneous system, this spectral quantity provides a measure of the average depth in the film up to which electron-hole pairs are created. The importance of this relationship is reflected in the spectral absorptance shown in Figure 2-4c, which indicates that although the films are optically thick at wavelengths below ca. 500 nm, the IPCE values remain low in this spectral range and gradually decrease with increasing wavelength. Electron conduction in α-Fe_2O_3 occurs in narrow Fe d levels[3] and has been described to occur by the small polaron hopping mechanism.[20] Consequently charge transport in this material is especially sensitive to defect concentrations. It is observed that in the lower energy region, where the longer light penetration depth requires longer carrier transport distances, lower photocurrents are measured in the external circuit. It could be inferred that although low temperature samples likely possess a higher degree of porosity and therefore greater electrochemically active surface area (see Figure 2-1b,d), the high temperature sample's expected superior transport properties outweigh this advantage.

The photocurrent-intensity dependencies in Figure 2-4d confirm the existence of differing transport properties among the films. Slopes near unity in plots of this type, as observed for the 300 °C sample, have been previously measured in conditions where electron-hole recombination is not significant.[21] The slope associated with the low temperature samples, near 0.7, indicates that even over the weak intensity range studied (80-160 mW cm^{-2}), these films are unable to efficiently convert additional photon flux into photocurrent. Most probably significant electron-hole recombination would be observed in the form of non-linear current-intensity dependences for all samples at irradiation intensities higher than those permitted within the experimental constraints of the present study. The comparatively weaker current-intensity dependence even at low intensities for samples deposited at low temperatures suggests severe transport limitations in these structures, perhaps originating from lattice disorder or higher densities of surface trap states caused by their apparently higher surface area.

2.4 Conclusions from Chapter 2

This chapter presented the morphological, optical, and photoelectrochemical characterization of doped iron oxide film electrodes for implementation into solar water splitting PEC devices. It was determined that despite their apparent increased surface area, porous electrodes deposited at 23 °C were significantly less efficient than denser electrodes deposited at 300 °C. It is hoped that such a finding is applicable to future studies of the fabrication of efficient iron-oxide-based photoanodes, which is known to require careful film growth engineering. In attempting to fabricate nanostructured Fe_2O_3 films for this application great care must be taken to maintain the structural quality and related electronic character of crystallites.

2.5 References for Chapter 2

1. J. Augustynski G. Calzaferri, J. Courvoisier, and M. Grätzel, in Proceedings of the 11th World Hydrogen Energy Conference, edited by T. N. Veziroglu, C.- J. Winter, J. P. Baselt, and G. Kreysa (DECHEMA, Frankfurt, 1996), p. 2378.
2. E. L. Miller, R. E. Rocheleau, and X. M. Deng, Int. J. Hydrogen Energy 28, 615 (2003).
3. F. J. Morin, *Phys. Rev.* **93**, 1195 (1954).
4. J. H. Kennedy and K. W. Frese, *J. Electrochem. Soc*. **125**, 709 (1978).
5. V. R. Satsangi, S. Dass, and R. Shrivastav, in On Solar Hydrogen and Nanotechnology, edited by L. Vayssieres (Wiley, Singapore, 2009), pp. 349–397.
6. K. Robbie, J. C. Sit, and M. J. Brett, *J. Vac. Sci. Technol. B* **16**, 1115 (1998).
7. A. Wolcott, W. A. Smith, T. R. Kuykendall, Y. Zhao, and J. Z. Zhang, *Small* **5**, 104 (2009).
8. N. T. Hahn, H. Ye, D. W. Flaherty, A. J. Bard, and C. B. Mullins, *ACS Nano* **4**, 1977 (2010).
9. A. Wolcott, W. A. Smith, T. R. Kuykendall, Y. Zhao, and J. Z. Zhang, *Adv. Funct. Mater.* **19**, 1849 (2009).
10. W. Smith, Z. Y. Zhang, and Y. P. Zhao, *J. Vac. Sci. Technol. B* **25**, 1875 (2007).
11. W. Smith and Y. P. Zhao, *Catal. Commun.* **10**, 1117 (2009).
12. K. Sivula, R. Zboril, F. Le Formal, R. Robert, A. Weidenkaff, J. Tucek, J. Frydrych, and M. Grätzel, *J. Am. Chem. Soc.* **132**, 7436 (2010).
13. D. L. Smith, Thin-Film Deposition: Principles and Practice (McGraw-Hill, Boston, 1995).
14. H. Fujiwara, Spectroscopic Ellipsometry: Principles and Applications (Wiley, West Sussex, 2007).
15. G. E. Jellison and F. A. Modine, *Appl. Phys. Lett.* **69**, 371 (1996).
16. D. A. G. Bruggeman, *Ann. Phys.* **416**, 636 (1935).
17. J. A. Glasscock, P. R. F. Barnes, I. C. Plumb, and N. Savvides, *J. Phys. Chem. C* **111**, 16477 (2007).
18. M. D. Ward, J. R. White, and A. J. Bard, *J. Am. Chem. Soc.* **105**, 27 (1983).

19. K. M. Rosso, D. M. A. Smith, and M. Dupuis, *J. Chem. Phys.* **118**, 6455 (2003).

20. H. Wang, T. Lindgren, J. He, A. Hagfeldt, and S. -E. Lindquist, *J. Phys. Chem. B* **104**, 5686 (2000).

2.6 Appendix for Chapter 2

2.6.1 Determination of optical functions

The optical properties of films were analyzed by measurement and modeling of spectral normal transmission and normal and 70 degree specular reflection data using a thin film metrology system and its multi-layer film analysis software (FilmTek 3000 PAR SE). As described below, the optical functions of a film deposited at 300 °C onto SiO_2 were determined by simulation of the dielectric functions of a substrate-film-surface roughness structure as indicated in Figure 2-5. The regression analysis software attempts to minimize a root mean square error function associated with the simulated quantities over the entire spectral range of collected data. Statistical analysis of the accepted final simulation yielded a correlation coefficient of 0.995 and standard errors as tabulated below. It is noted that a compensator in the 70 degree light source beam path polarized incident light. Since α-Fe_2O_3 crystals are known to be birefringent, it was necessary to check for polarization effects in the reflection measurement. This was accomplished by adjusting the angular positions of the analyzer and polarizer so that they are crossed by 90 degrees, and monitoring the signal at the detector. No signal beyond the system noise was detected; the sample did not depolarize incident light to any measurable degree. This is further confirmed by the observed correlation between experimental and simulated values.

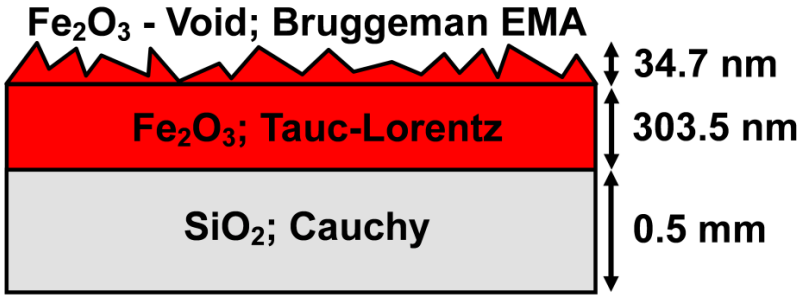

Figure 2-5 Multi-layer structure used as model for simulation of optical functions, with final determined values for layer thickness included.

The complex index of refraction of the 0.5 mm-thick SiO_2 substrate was modeled with the Cauchy dispersion relations[1]:

$$n_\lambda = A_n + \frac{B_n}{\lambda^2} + \frac{C_n}{\lambda^4} \qquad (2-1)$$

$$k_\lambda = A_k + \frac{B_k}{\lambda^2} + \frac{C_k}{\lambda^4} \qquad (2-2)$$

Coefficient data used were literature-derived values included in the commercial software package, displayed in Table 2-1.

Table 2-1 Coefficients for the Cauchy dispersion relations used for substrate characterization.

Cauchy	
Parameter	Value
A_n	1.44785
B_n	3.4134 x 10^{-3}
C_n	2.0470 x 10^{-5}
A_k	2.8619 x 10^{-19}
B_k	1.2274 x 10^{-19}
C_k	6.5623 x 10^{-21}

The optical functions of the photoactive Fe_2O_3:TiO_2 films were simulated using the Tauc-Lorentz parameterization, formulated by Jellison and Modine in 1996.[2] The software performs the regression with the parameterization:

$$\varepsilon_2(E) = \sum_j^m \frac{A_j^2 (E_{center})_j \upsilon (E - E_g)^2}{\left[E^2 - (E_{center})_j^2\right]^2} \cdot \frac{1}{E} \qquad E > E_g \qquad (2-3)$$

$$\varepsilon_2(E) = 0 \qquad E \le E_g \qquad (2-4)$$

$$\varepsilon_1(E) = \varepsilon_\infty + \frac{2}{\pi} P \int_{E_g}^{\infty} \frac{\xi \varepsilon_2(\xi)}{\xi^2 - E^2} d\xi \qquad (2-5)$$

The fitted values for a single oscillator and their associated standard errors are presented in Table 2-2.

Table 2-2 Coefficients for the Tauc-Lorentz dispersion relations used for film characterization.

Tauc-Lorentz		
Parameter	Value	Standard Error
ε_∞	2.042	0.025
E_g	1.894	2.265 x 10^{-3}
A	11.091	0.158
E_{center}	2.652	0.032
υ	3.622	0.076

The thickness of the Fe_2O_3:TiO_2 layer at the probe location was determined to be 303.5 nm.

The surface roughness was modeled with the Bruggeman[3] Effective Medium Approximation, which in this case assumes an isotropic mixture of the dielectric functions of void space and film.

$$\sum_{i=1}^{m} f_i \frac{\varepsilon_i - \varepsilon_{eff}}{\varepsilon_i + 2\varepsilon_{eff}} = 0 \qquad \sum_{i=1}^{m} f_i = 1 \tag{6}$$

Where f represents the volume fraction of constituent phases.

The regression analysis determined a composition of 87 % void and 13% film (volume percent), with a total layer thickness of 34.7 nm.

2.6.2 Deposition geometry

The off-angle deposition geometry, as described in the main text, is represented schematically over a photograph of a typical ablation plume in Figure 2-6.

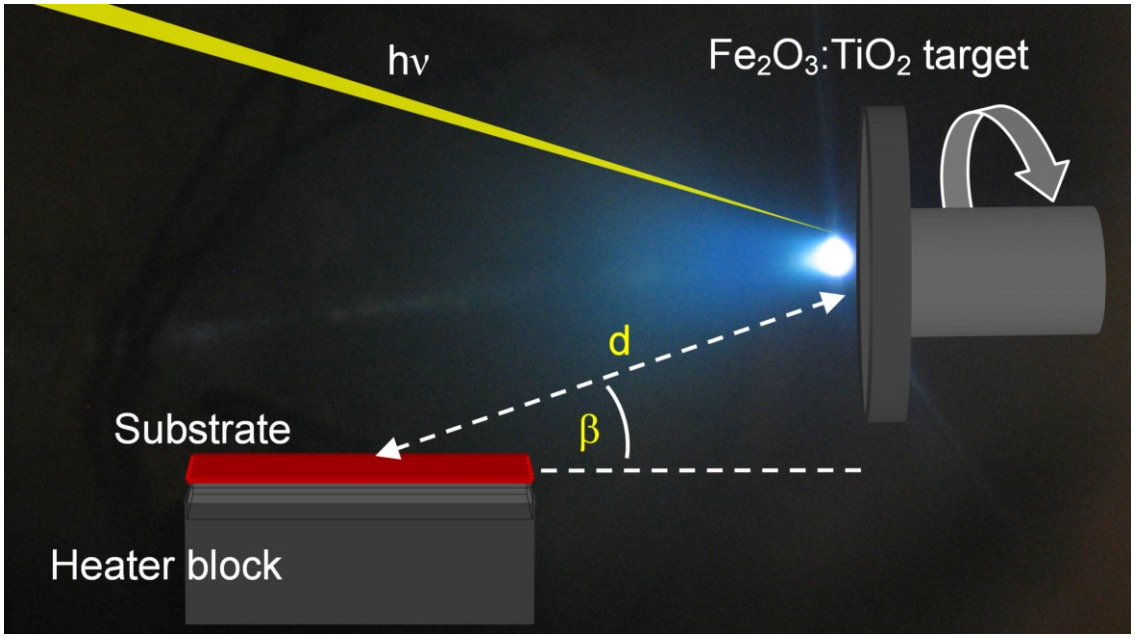

Figure 2-6 Schematic of the deposition geometry overlayed onto a photograph of an ablation plasma and its optical emission (d = 7.9 cm, β = 49° for all depositions).

2.6.3 Effect of post-deposition heat treatment on structure morphology

SEM imaging was performed for both as-deposited and heat-treated films. The SEM images shown in Figure 2-7 indicate the effect of the heat treatment process. The 23 °C sample shows the most dramatic morphology change upon annealing. This result suggests the as-deposited sample may contain significant void space, unresolved in the SEM imaging, which grows upon annealing as particles coalesce.

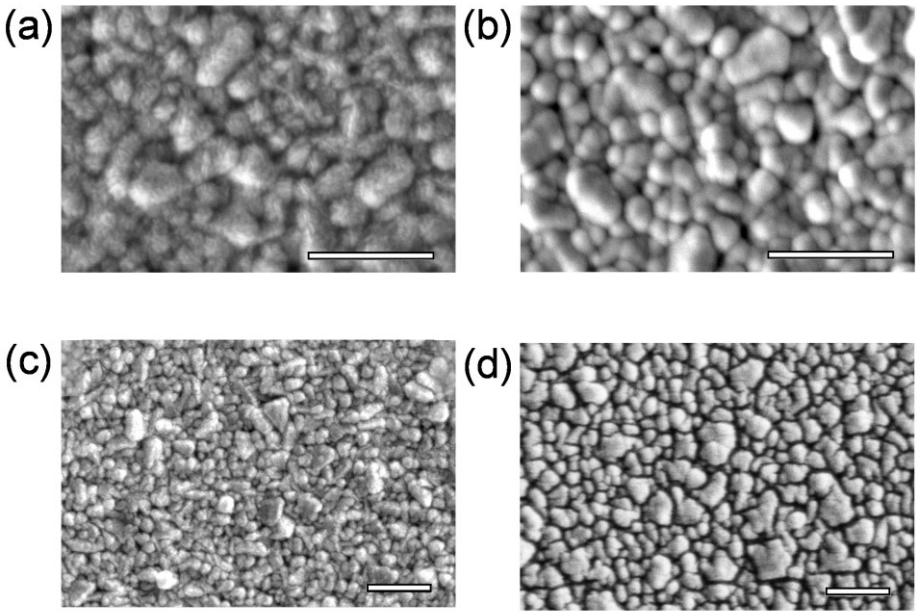

Figure 2-7 SEM images indicating the effect of annealing on film morphology: (a) 300 °C sample as deposited. (b) 23 °C sample as deposited. (c) 300 °C sample after heat treatment at 450 °C. (d) 23 °C sample after heat treatment at 450 °C. All scale bars indicate 1 μm.

2.6.4 References for Chapter 2 Appendix

1. H. Fujiwara, in: Spectroscopic Ellipsometry: Principles and Applications, (Wiley, West Sussex, UK, 2007).

2. G. E. Jellison and F. A. Modine, *Appl. Phys. Lett.* **69**, 371 (1996).

3. D. A. G. Bruggeman, *Ann. Phys. Leipzig* **24**, 636 (1935).

3 Metal oxide hetero-nanostructures for solar water splitting

Chapter 3 is an adaptation of a published article:

Coleman X. Kronawitter, Lionel Vayssieres, Shaohua Shen, Leijin Guo, Damon A. Wheeler, Jin Z. Zhang, Bonnie R. Antoun, and Samuel S. Mao, Energy Environ. Sci., 2011, 4, 3889-3899, DOI: 10.1039/C1EE02186A

The majority of the work in this chapter was supported by Sandia National Laboratories. Sandia National Laboratories is a multi-program laboratory managed and operated by Sandia Corporation, a wholly owned subsidiary of Lockheed Martin Corporation, for the U.S. Department of Energy's National Nuclear Security Administration under contract DE-AC04-94AL85000.

3.1 Abstract for Chapter 3

The previous chapter investigated nanostructured photoelectrodes known to possess transport property limitations. The substrate temperature was found to be a critical fabrication parameter, which is expected to be related to the strong influence the energy of adsorbed species has on film quality. Another technique to fabricate nanostructured materials onto substrates is the direct heteronucleation of crystals grown in solution. In Chapter 3, results are introduced for α-Fe_2O_3 fabricated by growth from aqueous solution, a technique which provides a method to bypass the strict fabrication requirement established in Chapter 2. A combination of chemical and physical techniques is also investigated to fabricate heterostructures with nanoscale dimensionality, the motivations for which are discussed in detail in this chapter.

Specifically a study of the design of all-oxide heterostructures for application in photoelectrochemical cells for solar water splitting is provided. Particular attention is paid to those structures which possess nanoscale feature dimensionality, as structures of this type are most likely to utilize the benefits afforded by the formation of oxide heterojunctions and likely to show functional behavior relating to the interfacial region. In the context of this discussion, a novel hetero-nanostructure array, based on quantum-confined and visible light-active iron(III) oxide nanostructures and their surface modification with tungsten(VI) oxide, is introduced. The heterostructure architecture is designed to combine the functionality of the constituent phases to address the primary requirements for electrodes enabling the efficient generation of hydrogen using solar energy: visible light activity, chemical stability, appropriate band edge characteristics, and potential for low-cost fabrication. Photoelectrochemical characterization for solar hydrogen/oxygen generation indicates the presence of unexpected minority carrier transfer dynamics within the oxide hetero-nanostructures, as observed additionally by ultrafast transient absorption spectroscopy.

This work involved some measurements from collaboration with researchers at University of California at Santa Cruz. Specifically it involved collaboration with Damon Wheeler and Jin Zhang in the UC Santa Cruz Department of Chemistry and Biochemistry.

3.2 Introduction to Chapter 3

Metal oxide heterostructures can be engineered to possess functional behavior that results both from the bulk properties of their constituent phases as well as from the emergent properties that relate directly to the electronic and atomic character of their interfaces. The study of oxide heterostructures has led to the discovery of a number of new and technologically promising interfacial phenomena, including magnetism from non-magnetic materials, [1] electronic conductivity from insulators,[2] and emergent ionic conductivity.[3]

In addition to their prospective application as electronic and magnetic device components, oxide heterostructures have been applied as photoactive components of photoelectrochemical (PEC) devices devoted to the clean and sustainable generation of hydrogen from water using sunlight. The motivation for these applications relates to diversity of cation oxidation states, crystal structures, and electronic configurations, and to the concomitant material properties, associated with oxides and especially with the oxides of the transition metals. Utilizing this diversity by combining dissimilar oxide materials allows for design of photoelectrodes specialized to perform the optical, electronic, and chemical functions required of PEC solar water splitting cells.

This perspective focuses on the design of all-oxide heterostructure photoanodes whose function is to enable the photo-oxidation of water, a critical and performance-limiting half reaction in the overall splitting of water to produce hydrogen and oxygen gas.[4] Particular attention is paid to those heterostructures with nanoscale dimensionality, as structures of this type are most likely to utilize the benefits afforded by the formation of oxide heterojunctions and likely to show functional behavior relating to the interfacial region. For detailed analyses of alternative designs, readers are referred to the comprehensive and ever-expanding literature of this field, which most recently includes books,[5] general and comprehensive reviews,[6,7] including progress in α-Fe_2O_3 electrodes,[8,9] discussions of composite systems incorporating catalytic phases,[10] and summaries of the use of nanomaterials,[11] among others.

3.3 Motivation for water oxidation at nanoscale oxide heterostructure photoanodes

3.3.1 Oxide nanostructures

The in-depth consideration of physical processes that occur on nanometer length scales is the defining principle guiding advances in the next generation of solar energy conversion technologies.[12] The application of nanoscience to solar energy conversion appears to represent a pivotal step toward implementing cost-effective energy conversion schemes.[5,6,13,14,15,16,17] Recent notable contributions in this area include the in-depth study of Si nanowire arrays for photovoltaics [18, 19] the fabrication of efficient dendritic α-Fe_2O_3 nanostructures for water oxidation,[8] and the use of plasmonic resonance modes to enhance PEC performance.[20] Most important to the success of these endeavors is the design of new materials, structures, or

architectures that can utilize a fast-growing understanding of nanoscale optoelectronic phenomena, and which can potentially bypass or surpass certain constraints that arise from consideration of conventional materials for this application.

Metal oxide nanomaterials in particular have been extensively investigated for application to solar energy conversion for their diversity of optical properties, electronic and ionic transport properties, chemical and thermal stability, ease of fabrication, and relative low cost. When integrated into solar energy conversion devices, single-crystalline one-dimensional (1-D) metal oxide structures optimize crucial operation processes by increasing optical path lengths and providing direct electronic carrier transport pathways. Aligned oxide nanostructures can now be fabricated onto large-area substrates using controllable and inexpensive techniques.[21]

Photoactive oxide nanomaterials – those with suitable bandgaps to absorb visible light – are stable when irradiated and biased in most chemical environments, and are therefore compatible with a number of PEC device configurations for solar electricity and renewable fuel production. This includes semiconductor-based PEC cells for water splitting or electricity generation[22] as well as dye-[23] and quantum dot-sensitized[12] solar cells. However, no single photoactive metal oxide material has proven to possess the required optoelectronic properties to efficiently convert solar light energy into electrical or chemical energy; although recent promising results indicate progress in this direction.[24]

3.3.2 Oxide heterostructures

A summary of the various motivations for design of oxide heterostructures for solar water oxidation is presented in Figure 3-1. As has been established in the decades of research in tandem photovoltaics, placing in series multiple optical absorbers has the potential to dramatically increase the overall conversion efficiencies of solar energy conversion devices. Because of the known thermodynamic requirements[7] for the photo-oxidation of water, it is likely a successful heterostructure will involve successive absorption of UV and visible (blue, green, and yellow) light.

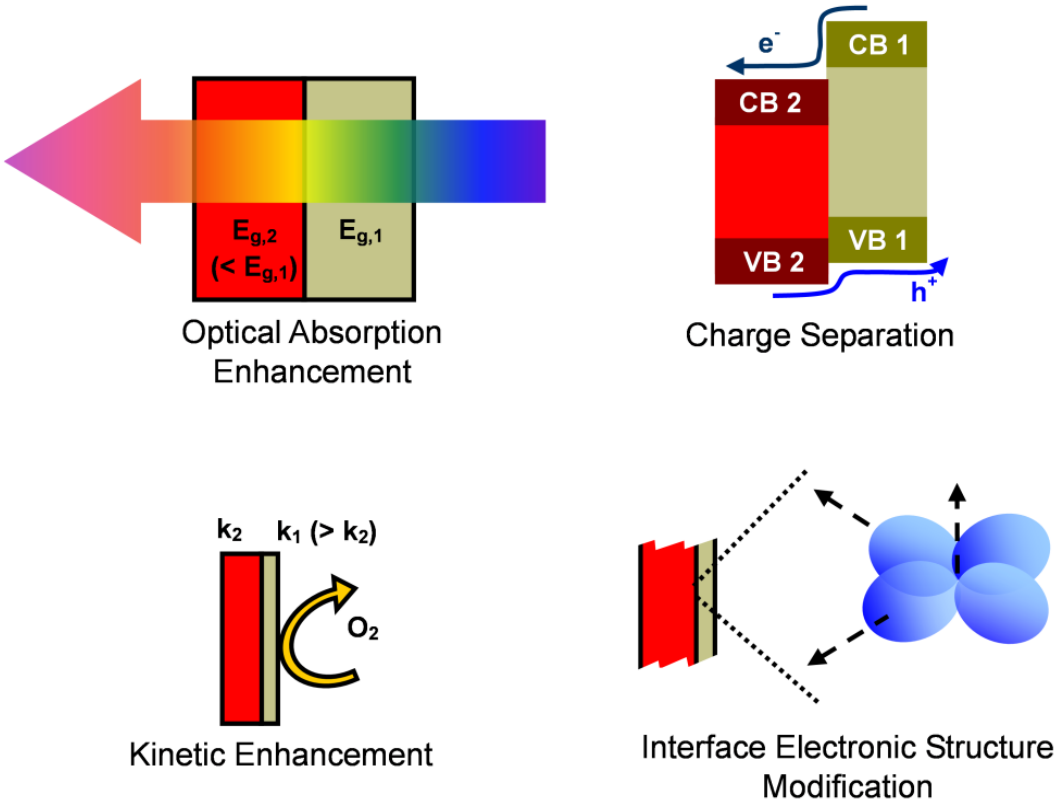

Figure 3-1 Illustrations depicting the primary processes responsible for performance enhancements in oxide heterostructure photoelectrodes.

Optical absorption enhancements effected by multiple bandgaps translate to conversion efficiency enhancements only if the band structure alignments permit efficient utilization of photoexcited charges. In solid-state nanostructured photovoltaic devices, heterostructures comprised of photoactive semiconductors exhibiting Type II band offsets are utilized to promote the efficient separation of photogenerated charges under irradiation.[25] Similarly, in dye- and quantum dot-sensitized solar cells, heterojunctions of transparent oxides with differing electron affinities are utilized to suppress detrimental back reactions (or charge recombination). By directing charges to lower energy states physically separated from the photoexcited dye or quantum dots, this technique has led to efficiency enhancements in both nanoparticulate[26] and nanorod[27] configurations.

Band offsets among photoactive oxides can promote charge separation if the constituent phases and their junctions provide the necessary conduction pathways for efficient operation of the electrochemical cell. Establishing efficient conduction paths in oxide heterostructure photoanodes is complicated generally by the orbital composition of most relevant oxides' occupied electronic structures: valence band edges are primarily of O 2*p* character, resulting in little deviation in ionization potential among the oxides.[28] Their common orbital character creates difficulty in establishing valence band offsets that facilitate hole separation during

operation of the oxide heterostructure photoanode. However, because the oxides' conduction bands are generally cationic in character,[28] this observation contrasts with that found for electron transfer across heterojunctions. The recent development of highly efficient Cu_2O-based heterostructure photocathodes[29] highlights the additional versatility provided by energy bands whose chemical character is primarily cationic.

There is considerable evidence available suggesting that the surface modification of oxide photoanodes with ultrathin oxide coatings has the potential to affect enhanced kinetics for water oxidation at the oxide-electrolyte interface. Ultrathin coatings permit electron tunneling, passivate dangling bonds, or possess electronic structures that differ from corresponding bulk structures. These configurations potentially alleviate restrictions associated with incompatible band alignments.

Finally, it is suggested here that the fabrication of oxide hetero-nanostructures possessing high interfacial areas is likely to enable the development of materials with entirely new electronic structures, with associated electronic and optical properties and thus technological potential. As will be elaborated upon later in this report, the powerful combination of nanoscience and oxide interface engineering may potentially lead to development of new interface-property-driven electrode structures.

3.4 Discussion of selected recent systems

There is considerable content in the literature that suggests the benefits described above indeed are associated with performance enhancements for oxide photoanodes in PEC cells. Table 3-1 provides a summary of selected recent systems from the literature that highlight these findings. The table also includes the charge transfer among oxide phases suggested in the study. This summary is by no means comprehensive and is meant solely as an introduction to the recent research efforts dedicated to the design of oxide heterostructures for this application.

3.5 Nanoscale architectures

Various heterostructure architectures possessing nanoscale feature dimensionality show promise to effectively utilize the benefits described above. The concept of extremely thin-absorbers,[30] as established for photovoltaic devices, has been successfully applied in designs for oxide heterostructure photoanodes. In short, by placing the absorbing phase in intimate contact with a nanostructured conductive substrate, this technique permits the use of materials with small carrier diffusion lengths but large optical absorption lengths. Glasscock [31] fabricated and characterized core-shell nanorod ZnO-α-Fe_2O_3 heterostructures using a combination of aqueous chemical synthesis and vapor phase deposition. Their characterization revealed the presence of α-$Fe_2O_3 \rightarrow$ ZnO electron transfer during irradiation, and showed some long wavelength conversion enhancements associated with the architecture. The analysis suggested a significant energy barrier for electron injection from α-Fe_2O_3 into ZnO, which is consistent with expectations considering ZnO's greater electron affinity. Sivula *et al.*[32] utilized a two-step atmospheric pressure CVD process to produce WO_3-α-Fe_2O_3 heterostructures, which showed PEC enhancements at weakly absorbing long wavelengths, which was directly attributed to the presence of the nanostructured WO_3 substrate. Oblique-angle physical vapor deposition, which

enables fabrication of nanostructured films using ballistic species transport and self-shadowing effects, has recently been used to fabricate WO_3-TiO_2 core-shell nanostructures.[33] Charge transfer between the phases was observed and was associated with overall efficiency enhancements. A related nanoscale architecture was previously achieved by coating TiO_2 nanotubes with WO_3 by electrochemical deposition.[34]

WO_3 and $BiVO_4$ were combined in a recent work by Su *et al*.[35] to efficiently utilize both the complimentary optical absorption of these materials and charge separation ability associated with their junction. Because the valence band edge of $BiVO_4$ contains contributions from Bi *s* states, it is situated at higher energies than that of WO_3, and therefore provides an efficient mechanism for the separation of photogenerated holes during photanode operation. Their results showed considerable enhancements are associated with the heterostructure configuration. Nanoparticle heterostructures comprised of α-Fe_2O_3 and $CoAl_2O_4$ nanoparticles have shown PEC performance enhancements over bare p-type $CoAl_2O_4$.[36] It was speculated that the differing conductivity types of the nanoparticles, organized in three dimensions, facilitated charge separation under irradiation.

Table 3-1 Summary of selected recent oxide heterostructure systems discussed in this report.

Heterostructure	Description	Fabrication methods	Suggested charge transfer		Ref.
			Electron	Hole	
α-Fe_2O_3 – $CoAl_2O_4$	Nanoparticle composite	Doctor blading	α-Fe_2O_3 → $CoAlO_4$	$CoAlO_4$ → α-Fe_2O_3	36
α-Fe_2O_3 – TiO_2	Bilayer film	Thermal growth; CVD	TiO_2 → α-Fe_2O_3	α-Fe_2O_3 → TiO_2	41
α-Fe_2O_3 – WO_3	Bilayer film	Sol-gel	WO_3 → α-Fe_2O_3	none	40
WO_3 – α-Fe_2O_3	Nanostructured composite	APCVD	α-Fe_2O_3 → WO_3	none	32
WO_3 – $BiVO_4$	Core-shell nanostructure arrays	Solvothermal technique; spin coating	$BiVO_4$ → WO_3	WO_3 → $BiVO_4$	35
WO_3 – $BiVO_4$	Bilayer film	Spin coating; polymer-assisted direct deposition	$BiVO_4$ → WO_3	WO_3 → $BiVO_4$	37,38
Fe_2O_3 – $SrTiO_3$	Bilayer film	Spin coating	$SrTiO_3$ → WO_3	WO_3 → $SrTiO_3$	39
WO_3 – TiO_2	Core-shell nanostructure arrays	Oblique-angle deposition	TiO_2 → WO_3	WO_3 → TiO_2	33
WO_3 – TiO_2	Coated nanotube arrays	Electrochemical anodization and deposition	none	none	34
ZnO – α-Fe_2O_3	Core-shell nanostructure arrays	Aqueous chemical synthesis; filtered arc deposition	α-Fe_2O_3 → ZnO	none	31

3.5.1 Bilayers

In systems not limited by charge transport, simple bilayer heterostructures provide an effective means to utilize the complimentary functionalities of metal oxides. WO_3 and $BiVO_4$ bilayers have been studied comprehensively,[37, 38] and in general these configurations permit the simultaneous utilization of the transport properties of WO_3 as well as the optical absorption properties of $BiVO_4$.[37] Similarly, Fe_2O_3 has been combined with the transparent wide-bandgap insulator $SrTiO_3$[39] for the purpose of charge separation, with consistent enhancements evident. WO_3-α-Fe_2O_3 bilayer films show enhancements associated with formation of their junction.[40] Interestingly, an electrode comprised of a 120 nm TiO_2 surface layer on thermally grown α-Fe_2O_3 was shown to exhibit energetic contributions from both phases.[41] In general, the simple geometries of bilayer heterostructures provide systems that are suitable for fundamental analyses of prospective photoanode materials and especially of the potential benefits of junction formation.

3.5.2 Ultrathin coatings

In a discussion of oxide heterostructures with nanoscale dimensionality it is worthwhile to comment on the influence of ultra-thin surface coatings, and especially on their influence on α-Fe_2O_3-based photoanodes. The poor water oxidation kinetics of α-Fe_2O_3 focuses attention on the modification of surface states, toward increasing rate constants associated with electron transfer from hydroxyl ions in solution. It was shown that the deposition of tungsten oxide species on the surface of α-Fe_2O_3 films increases the faradic rate constant for water oxidation.[42] More recently the α-Fe_2O_3 surfaces were passivated with ultrathin Al_2O_3[43] and Ga_2O_3[44] layers, which show consistent and positive effects on photoelectrochemical performance, including a cathodic shift of the photocurrent onset of α-Fe_2O_3. In general it can be expected that ultrathin coatings passivate surface states and therefore reduce the probability of electron-hole recombination associated with their presence. This is especially true for those oxides that are isostructural to α-Fe_2O_3.[44]

3.6 The α-Fe_2O_3-WO_3 system

3.6.1 Introduction to material system

The above discussion above describes the motivation and framework for developing effective oxide heterostructures with nanoscale dimensionality for efficient solar water oxidation. The present section introduces and discusses in this provided context recent experimental work from the authors' laboratories.

Tungsten(VI) oxide (tungsten trioxide, WO_3) and its slightly reduced form WO_{3-x} are intensely studied as solar energy materials for their significant photoactivity under UV and blue light irradiation. In PEC devices, nanostructured WO_3 films produce high photocurrents for water oxidation, and are compatible with a number of tandem designs based on multiple photosystems.[45,46] The material's ability to produce high, stable photocurrents for *sea water* splitting is considered an important discovery toward sustainable and economical solar fuel production.[47]

Alpha-phase iron(III) oxide (hematite, α-Fe_2O_3) is highly abundant in Earth's crust and is widely utilized by a number of established and global industries. Nanostructured α-Fe_2O_3 in particular has proven to be a highly functional metal oxide for a number of energy applications. It has received considerable attention as a solar energy conversion material because its bandgap is well-suited for solar photon absorption and its high ionization potential yields a valence band appropriately positioned to accept charges toward the oxidation of water. The extreme low cost and chemical stability of α-Fe_2O_3 make its implementation into solar energy conversion devices highly attractive for the development of economical solar electricity and fuel production.

Figure 3-2 provides an illustration depicting the hetero-nanostructure design. Depending on the fabrication conditions and application at hand, these anisotropic composites might be described as nanoparticle-sensitized, core-shell, or radial-junction structures. In the present case, both materials are photoactive under solar irradiation when applied as electrodes in a PEC cell, as indicated in the illustration and described later in this report. The arrays were fabricated through

application of a combination of aqueous chemical growth[48] and physical vapor deposition techniques (see Methods for details).

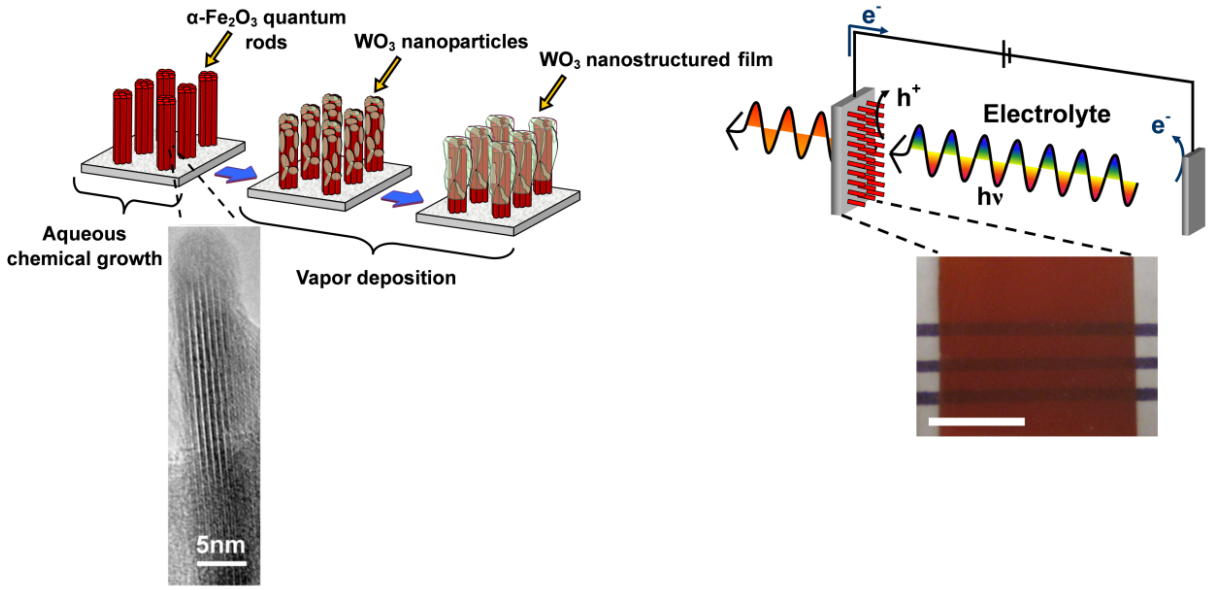

Figure 3-2 Illustration depicting the design of metal oxide hetero-nanostructure arrays and their application as photoanodes for photoelectrochemical cells. The HRTEM image shows an individual single-crystalline α-Fe_2O_3 quantum rod. The picture on the right shows the as-prepared sample (Scale bar indicates 1 cm).

3.6.2 Physical and optical characterization

The morphology of the arrays is examined through scanning electron microscopy and is presented in Figure 3-3a-e. Figure 3-3a shows the α-Fe_2O_3 nanorods produced by the hydrolysis-condensation and dehydration process.[48] The width of these rod bundles is approximately 50 nm and their length is approximately 800 nm. As indicated in the HRTEM image in Figure 3-2, they consist of 3-5 nm-diameter single crystals whose electrons are quantum-confined in the lateral dimension, which manifests as a cathodic shift (vs SHE) of the conduction band and a bandgap blue-shift.[49] They provide a very efficient pathway for both majority carriers (direct pathway along the vertically oriented rods) and minority carriers (hole diffusion length match with the quantum rod lateral dimensions).[49] The structures after modification with WO_3 are displayed in Figure 3-3b-d. The large internal surface area is maintained and the diameter of the structures increases with increasing deposition time indicating that the rods are coated with a thin layer of WO_3 during exposure to the deposition source. Similar coatings resulting from nanorod exposure to laser ablation plasmas have previously been observed for a ZnO-ZnSe system.[50] Figure 3-3e shows a cross sectional view of the structures after extended exposure. There is a slight gradient in thickness along the length of the rod, which is attributed to shadowing effects commonly encountered in vacuum deposition techniques.

The optical and structural properties of the hetero-nanostructures deposited onto 2.3 mm thick transparent conductive fluorinated tin oxide-coated soda lime glass (SnO_2:F/glass) are displayed

in Figure 3-3f and Figure 3-3g. All samples are deep red and transparent to lower-energy visible light (see representative sample photograph in Figure 3-2). The UV-vis-near IR spectrum of the hetero-nanostructures is presented in Figure 3-3h. The main absorption transition around 600 nm matches closely to those of the α-Fe_2O_3 nanorods,[51] which is consistent with expectations considering the larger bandgap of WO_3. x-ray diffractograms (Figure 3-3h) indicate the presence of three distinct crystal phases: orthorhombic WO_3, trigonal Fe_2O_3 (hematite), and the tetragonal SnO_2 (cassiterite) substrate.

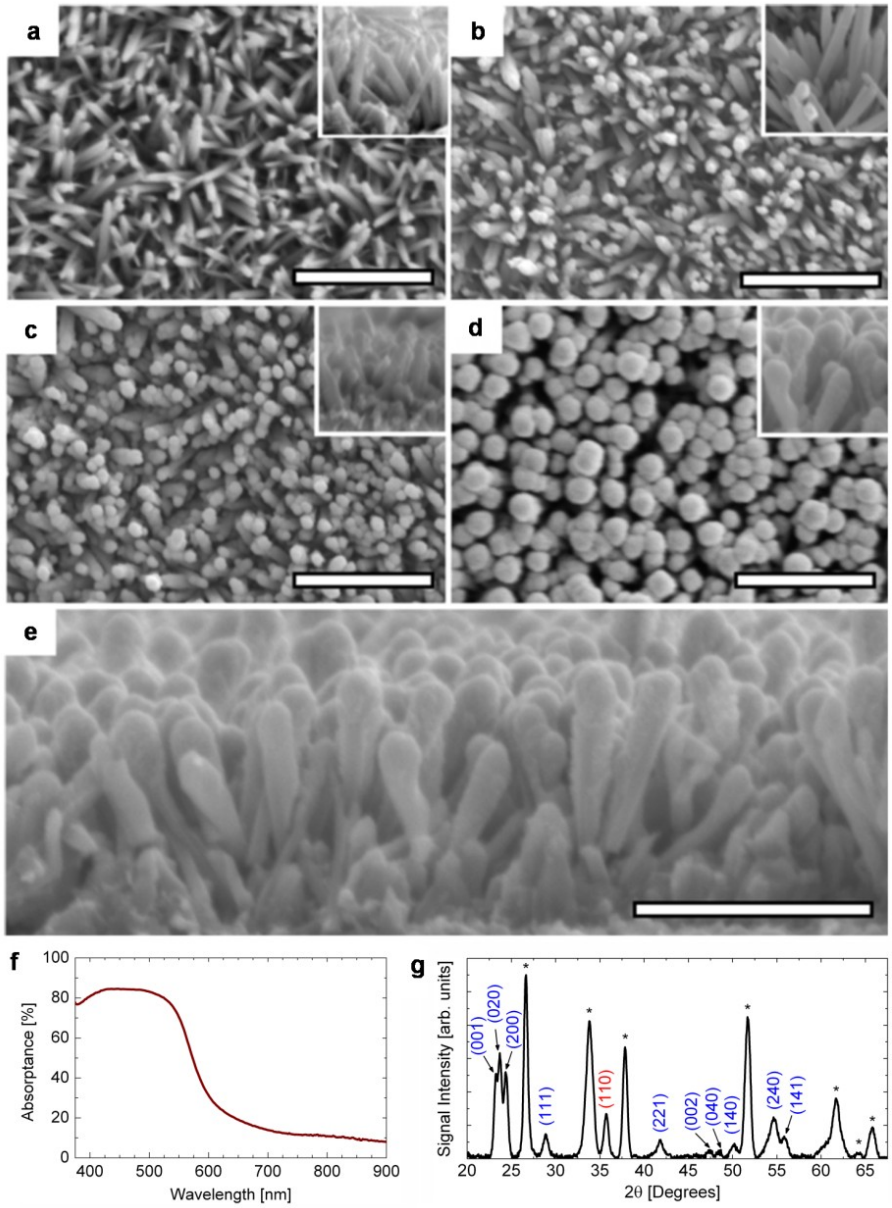

Figure 3-3 (a) SEM images of α-Fe_2O_3 arrays as fabricated by aqueous chemical growth. (b)-(d) SEM images of arrays modified by WO_3 for increasing deposition times, indicating the evolution of the structure morphology. (e) SEM Cross-sectional view of hetero-nanostructure array after longest deposition time. All scale bars indicate 1 µm. Insets provide cross-sectional views at identical magnification. (f) UV-vis-near IR optical absorptance of α-Fe_2O_3-WO_3. (g) x-ray diffraction pattern of the hetero-nanostructure array indicating the presence of orthorhombic WO_3 (blue), trigonal Fe_2O_3 (red), and tetragonal SnO_2 substrate (*).

3.6.3 Photoelectrochemistry

The samples have been applied as photoelectrodes in PEC cells for solar hydrogen generation. For this application, the interest in this system lies in the complimentary functionality offered by the two components. When the electrode is applied as an anode in a PEC cell for water photoelectrolysis, photogenerated holes participate in the water oxidation reaction and electrons travel to the back contact and enter the external circuit. The faradic rate constant for electron transfer from hydroxyl ions at the WO_3 surface is orders of magnitude greater than at the α-Fe_2O_3 surface (r_{WO3}= 10^3-10^4 cm s^{-1}; $r_{\alpha\text{-}Fe2O3}$= 0.1-1 cm s^{-1}),[52] due to the superior kinetics of charge injection into O 2*p* bands. The modification of α-Fe_2O_3 film surfaces with tungsten oxide species has been shown previously to increase the faradic rate constant for water oxidation.[42] The hole diffusion length in WO_3 has been estimated to be about 150 nm,[53] two orders of magnitude higher than that estimated for α-Fe_2O_3, 2-4 nm[54]. Despite these advantages, the theoretical maximum water splitting efficiency of WO_3 remains low due to insufficient overlap between its optical absorption and the solar spectrum. The bandgap of α-Fe_2O_3 on the other hand is nearly ideal, which results in a theoretical efficiency of 12.9 %.[55] The ultrafine α-Fe_2O_3 nanorods utilized in this study were first designed and fabricated by Vayssieres *et al*. with the small hole diffusion length of α-Fe_2O_3 in mind; their photoelectrochemistry has been documented.[51,56]

The hetero-nanostructure arrays and the bare α-Fe_2O_3 electrodes were studied in a two-electrode configuration for solar hydrogen generation. Figure 3-4a shows chopped-light current-potential behavior in an aqueous 0.5 M NaCl solution with solar-simulated 100 mW cm^{-2} AM 1.5G-filtered (1 sun) irradiation; Figure 3-4b provides an incident photon conversion efficiency (IPCE) spectrum. The sodium chloride solution is chosen for its similarity to the composition of filtered sea water; under these conditions the thermodynamically favorable electrochemical reactions are the hydrogen, oxygen (and potentially chlorine at high bias) gas evolution reactions. No sacrificial reagents are employed and the solution is neutral. All PEC results presented indicate that the arrays behave as photoanodes in these electrolytic conditions; that is, a positive photocurrent is observed at applied anodic potential.

These PEC data suggest that a significant quantity of holes originating from visible-light excitations is extracted before recombining with electrons traveling to the back contact. This is confirmed in the IPCE spectrum, which shows spectral response beyond 550 nm. Considering the transparency of WO_3 to visible light (E_{gap} ~ 3 eV), these low energy excitations must occur either in the α-Fe_2O_3 core, or at intra-bandgap defect, surface, or interface states in WO_3. The electrode operation is discussed below in the context of its physical design and its potential for possessing anomalous electronic characteristics.

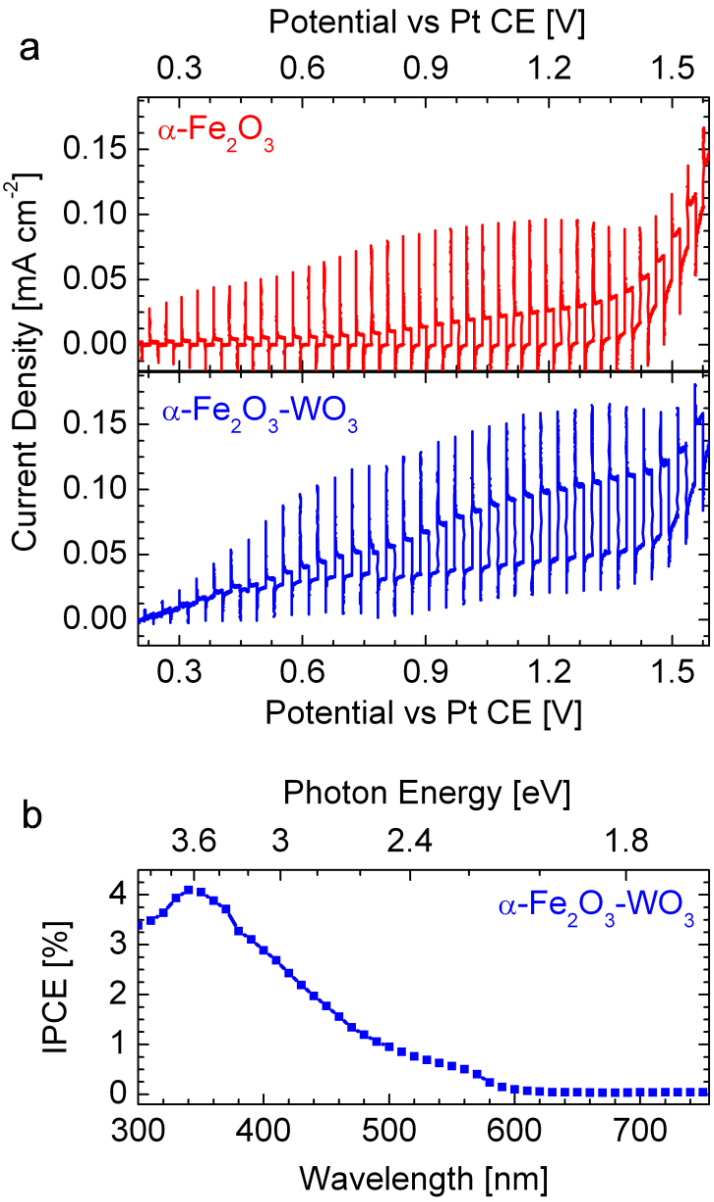

Figure 3-4 Photoelectrochemical characterization in aqueous 0.5 M NaCl solution: (a) Photocurrent-potential curve under chopped (0.2 s^{-1}), 100 mW cm^{-2} AM 1.5G-filtered solar-simulated irradiation. Potential applied vs a Pt CE. (b) IPCE spectrum with +1 V applied versus a Pt counter electrode. Data correspond to arrays fabricated as those in Figure 3-3c.

The hetero-nanostructure architecture demands electron transport through the α-Fe_2O_3 rods in order for the PEC cell to register photocurrent in the external circuit. Conduction band electron transport between the layers is therefore a topic of interest. Results in previous reports of α-Fe_2O_3-WO_3 composite photoanodes suggest electron transfer occurs in either direction under applied anodic potential.[32,40] Understanding of the band alignment in the present system is complicated by the quantum confinement effect in the α-Fe_2O_3 rods (Reference 49 indicates the electron affinity is near 0 V vs SHE).

Simultaneously, the oxidation reaction must occur in order to limit the recombination of free carriers, and therefore holes must be present at the hetero-nanostructure-liquid interface to accept charges from electrolyte species. From the viewpoint of bulk semiconductor physics, it is expected that there is an energy barrier of ca. 0.5 eV[57] for hole injection from α-Fe_2O_3 into WO_3, due to the energetic difference between O 2*p* orbitals, of which the valence band of WO_3 is comprised, and the Fe *d* levels at which holes arrive at the α-Fe_2O_3 surface (it is likely that holes arrive at the surface in a band of e_g levels, which are expected to be the highest occupied orbitals in α-Fe_2O_3[52]). The observation of photoactivity originating from visible light excitations could involve phenomena directly related to the nanoscale architecture. Indeed, at the length scales considered here, the interfacial region is expected to play an important role in the electronic band construction. In transition metal oxide heterostructures, interface electronic orbital reconstruction has been reported by a number of mechanisms, depending on the precise nature of the chemical bonds at the interface.[58] Considering the very high density of interface states in this system, owing to the nanoscale particle dimensions, it is feasible the valence band consists of hybridized orbitals with character resulting from both metal oxides and their surface configurations. The electronic character of the α-Fe_2O_3-WO_3 interface is expected to be extremely complex, and depend on several interface system properties, including charge transfer and orbital hybridization. Understanding these interface properties requires intense experimental investigations, the strategies for which are being studied in the authors' laboratories.[59]

Alternatively, due to the physical dimensions of the α-Fe_2O_3 structures (ca. 5 nm lateral dimension[49]) and thin WO_3 layers, quantum-mechanical tunneling processes must be considered for hole extraction from the core. The transfer of holes from α-Fe_2O_3 to an electrolyte through TiO_2, which also has a valence band edge derived from O 2*p* orbitals, was reported as early as 1982[41] and was attributed to a tunneling process. Reference 41 also suggests that band banding at the semiconductor-liquid interface could potentially extend through both phases in heterostructure photoelectrodes. If this is the case during operation of the present electrodes, depletion effects and upward band banding could assist in overcoming energy barriers for charge transfer from α-Fe_2O_3 to the electrolyte. It is unknown to what extent band banding exists in the α-Fe_2O_3-WO_3 electrodes; numerous previous studies suggest these effects are absent in nanostructured electrodes in contact with electrolytes.[60,61,62] Exciting work is currently being conducted in this area: a recent study from Augustynski and coworkers[63] suggests that during operation proton intercalation induces a structural change in mesoporous WO_3 electrodes, which results in a core-shell structure.

In the PEC configurations studied above, the electrode photocurrent response is remarkably similar to those found in previous studies of α-Fe_2O_3 nanorod arrays.[51,56,64] In addition, the photoelectrochemical characterization instrumentation employed was not precise enough to identify differences among samples with varying WO_3 thickness. Indeed, these PEC performance similarities most likely result from the current-limiting effect of the undoped α-Fe_2O_3 core, which is expected to be highly resistive.[65] These observations suggest that more in-depth optoelectronic characterization techniques are required to elucidate the complex charge transfer processes present in quantum-confined metal oxide hetero-nanostructures containing *d*-shell electrons. To this end the hetero-nanostructures' carrier dynamics were examined by ultrafast transient absorption spectroscopy.

3.6.4 Ultrafast transient absorption spectroscopy

The ultrafast carrier dynamics of α-Fe_2O_3 thin films, single crystals, and nanoparticle suspensions have been comprehensively examined.[66,67,68,69] It is observed that intraband carrier thermalization occurs on extremely fast times scales (< 150 fs;[66] < 75 fs[68]). Transient absorption signals at longer times are therefore attributed to relaxation of excited electrons to a dense manifold of electronic states within the bandgap and valence band, resulting from both intrinsic defects and surface states.[66] However, the assignment of transient absorption signals to specific physical correlates in this complex material system must be conducted in the context of all available information. This includes the many studies performed over the past few decades,[66,67,68,69,70] including several recent advances,[71,72] with numerous signal assignments proposed. In general the analysis is complicated by the *d-d* transitions present over spectral ranges commonly probed. Analyses of carrier dynamics of α-Fe_2O_3 nanomaterials is complicated in addition by high densities of surface states, which may introduce new decay pathways.

Of particular relevance to the present analysis is a recent report from Durrant and colleagues,[72] which describes the use of a hole-scavenging sacrificial chemical to determine the correspondence of the transient absorption signal at 580 nm to unoccupied valence band states (holes) in α-Fe_2O_3. The following discussion is presented in the context of this and other studies of excited carrier dynamics in related material systems.

The samples were pumped with 540 nm (2.29 eV) 130 fs pulses, which excite the α-Fe_2O_3 core near the weak Fe $3d \rightarrow 3d$ transition.[5] The transient absorbance spectrum of a representative α-Fe_2O_3-WO_3 sample is presented in Figure 3-5a at 500 fs after excitation. Absorption difference signals at various probe energies reflect the populations of electronic states with corresponding absorption energies after excitation. A broad distribution of absorbance signals over the studied wavelength range is evident at this delay time. Spectra of this type have been previously observed in femtosecond relaxation studies of iron oxide particulate suspensions.[68] These studies concluded that because the electron relaxation processes possess both a fast (~1 ps) and slower (~10 ps) decay over the entire probe spectrum, they may correspond to a common physical process – for instance, the capture of electrons by oxygen-deficient centers of Fe^{3+}.[68] As observed below, all relaxation processes exhibit both a sub-picosecond fast component as well as a longer component extending to hundreds of picoseconds.

Figure 3-5b-e show the normalized transient absorption signals for α-Fe_2O_3 and α-Fe_2O_3-WO_3 at two probe wavelengths, 579.31 nm (2.14 eV) and 674.23 nm (1.84 eV), in two time regimes. For both energies, there is an ultrafast rise in signal intensity limited by the laser pulse. Examination of the transient absorption at the picosecond time scale (Figure 3-5b,c) reveals the fast components of the kinetics for both probe energies are very similar before and after modification with WO_3. Because the time signatures of the signals' rise and decay overlap at this scale, the corresponding fast physical processes apparently occur irrespective of the presence of surface modification.

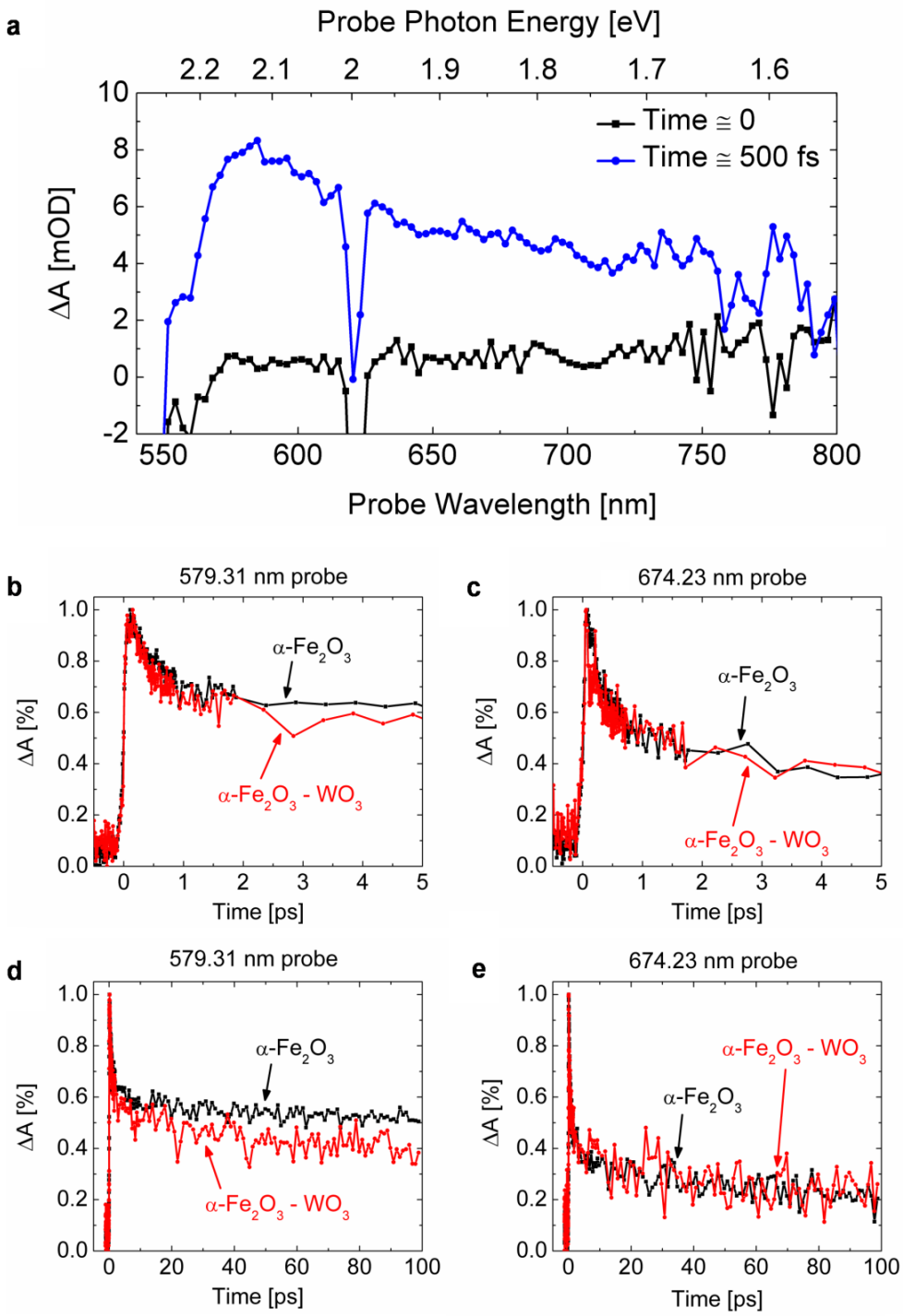

Figure 3-5 Ultrafast transient absorption spectroscopy for hetero-nanostructure electrodes: (a) Transient difference absorbance spectra for α-Fe_2O_3-WO_3 before excitation (black squares) and 500 fs after excitation (blue circles). Transient absorption signals for α-Fe_2O_3 (black) and α-Fe_2O_3-WO_3 (red) at the picosecond time scale for 579.31 nm probe (b) and 674.23 nm probe (c) and the sub-nanosecond time scale for 579.31 nm probe (d) and 674.23 nm probe (e).

Additional information is provided by the transient absorption at longer time scales (Figure 3-5d,e). For all probe wavelengths examined, following the initial fast process, there is a slow process that persists to beyond 100 ps. The most notable feature of these data is that the normalized transient absorption signal at 579.31 nm decays at a faster rate for α-Fe_2O_3-WO_3 than for α-Fe_2O_3. Considering that the transient absorption signal signifies the occupation of an electronic state at a given delay time, a faster destruction of the absorption signal at 579.31 nm may suggest a faster destruction (removal) of unoccupied states (holes) from the probed system. It is observed that the accelerated decay is nonexistent for the lower energy transition recorded at 674.23 nm. Alternatively, it is possible the decays represent a trapping process, and the introduction of the WO_3 phase enhances the trapping rate of electrons within a particular range of corresponding probe energies. Trapped electrons in this case possess a low extinction coefficient, which manifests as an attenuation of the associated probe signal.

Given the knowledge that α-Fe_2O_3 nanomaterials possess many midgap states, associated with both the *d* levels and high surface areas, the wavelength dependence could describe migration of photoexcited electrons from conduction bands into shallow levels and deep traps. In this case, the associated recombinations evolve over the spectral range probed.

Upon examination of the decay kinetics over the complete probe spectrum, it is found that the signals' attenuation difference upon creation of a α-Fe_2O_3-WO_3 interface is determined by the energetic position of the corresponding electronic state. Larger probe energies, near the bandgap of α-Fe_2O_3, exhibit the largest signal difference upon creation of an α-Fe_2O_3-WO_3 interface. Indeed, the aforementioned study on operating α-Fe_2O_3-based PEC cells[72] indicates that the removal of surface-trapped holes from α-Fe_2O_3 corresponds to decay in 580 nm absorption after excitation. Adoption of this assignment in the present study suggests that modification of α-Fe_2O_3 nanostructures with WO_3 promotes the extraction of surface-trapped holes on picosecond time scales.

These observations, when connected to the PEC results and band structure descriptions provided above, indicate the possible existence of anomalous carrier transport dynamics upon photoexcitation of the hetero-nanostructures.

3.7 Electronic structure of heterostructure interfaces

A number of the device performance enhancements associated with the use of nanomaterials relate directly to high surface areas and high densities of surface electronic states. Oxide hetero-nanostructures possess high *interfacial* areas, which can similarly be expected to contribute significantly to their electronic structures and therefore performance of electronic devices into which they are integrated.

The mechanisms by which oxide heterostructure interfaces are found to possess emergent functionality has been recently discussed[73] in a summary of the variety of physical phenomena associated with their fabrication. The summary proposes several strategies to tune the interface system's degrees of freedom, including charge transfer, epitaxial strain, symmetry breaking, electrostatic coupling, and frustration.[73] In addition to those effects isolated at interfaces, it is noted that several phenomena extend well away from interfaces. These phenomena include

unscreened Coulomb interactions as well as relaxations toward bulk properties away from the interface, which result in gradients of structure, polarization, and magnetization properties.

In the oxides of the transition metals, the *d* orbital character and occupancy critically influences the interaction of metal ions, and by extension the physical properties of these materials. Recent experiments conducted in the authors' laboratories[59] indicate that the formation of heterostructures comprised of titanium oxide and iron oxide nanomaterials, both of which are intensely investigated for photoelectrochemical applications, results in a number of modifications to the orbital character of the interface. Most importantly, it was found that the *d* orbitals in the interfacial region were enriched with electrons, which has a number of implications for devices utilizing transitions to and from their associated electronic states. In addition, through examination of the oxygen site environment, these studies provided evidence that the interface possessed an emergent degree of *p-d* orbital hybridization that was directly associated with formation of the heterojunction. These results provide confirmation of applicability of the principles of transition metal oxide interface engineering to the design of oxide heterostructure photoelectrodes for solar water splitting cells.

3.8 Conclusions from Chapter 3

A perspective on the design of oxide heterostructure photoanodes for solar water oxidation has been presented. Performance enhancements can be associated with increased optical absorption, efficient charge separation across heterojunctions, kinetic advantages, and potentially with the engineering of interface electronic characteristics.

The demonstration of the successful combination of large-scale chemical and vapor phase synthesis techniques for the fabrication of vertically oriented metal oxide hetero-nanostructures without template, surfactant or applied fields toward solar energy conversion is of direct relevance to optimized (doped) nanostructured oxide materials. These results suggest that through this novel nanoscale architecture it is possible to engineer interesting or unexpected interfacial minority carrier transport properties for PEC applications of metal oxide hetero-nanostructures. The constituent oxides are highly functional nanomaterials for a number of applications and as such the hetero-nanostructure array is expected to display further functionalities, as well as to pave the way to cost-effective, large scale, hetero-nanostructure devices for solar energy conversion.

3.9 Methods

The fabrication procedure of arrays in this work consists of application of a combination of solution chemistry and physical vapor deposition techniques. The α-Fe_2O_3 nanorod arrays were first fabricated onto SnO_2:F-coated glass (FTO; Pilkington TEC7) following the procedure for hydrolysis-condensation described in detail in reference 48. For PEC characterization, the samples were annealed in air 700 °C. The WO_3 layer was fabricated by deposition of species from pulsed laser ablation of a rotating (10 rpm) pressed polycrystalline WO_3 target in O_2 ambient (reactive pulsed laser deposition) using a Lambda Physik LPX 200 KrF Excimer Laser (248 nm). A stainless steel chamber was evacuated to a base pressure about 10^{-4} torr, after which O_2 gas (industrial grade) was flowed through the evacuated chamber for 30 minutes at 18 sccm,

as set by a mass flow controller, to replace residual gases. The α-Fe_2O_3/FTO sample was mounted on a substrate holder using conductive Ag paste. Deposition occurred at a laser fluence of ~ 1 J cm^{-2} per pulse with pulse frequency of 9 Hz for various times. Figure 3-3b-e show samples from deposition times of 5, 10, 16, and 16 minutes, respectively. The O_2 pressure during deposition was approximately 4×10^{-3} torr as measured by a pirani pressure gauge. Before deposition the target was ablated for a several minutes at the deposition laser parameters to remove any contaminants from the target surface, during which the entire substrate was masked with a mechanical shutter. Throughout deposition the sample was maintained at 100 °C using a resistance heater and thermocouple embedded in the substrate holder. After deposition the chamber was sealed and the sample was allowed to cool to room temperature in the quiescent low-pressure O_2 ambient. After the sample was removed it was annealed in air at 400 °C for 2 hours (the ramp rate to 400 °C was approximately 1.5 °C /min).

3.9.1 Physical characterization

Scanning electron microscopy (SEM) images were obtained with a Hitachi environmental field emission scanning electron microscope (Model S-4300SE/N) with an accelerating voltage of 3-5 kV, operating in secondary electron detection mode.

Spectral transmittance and reflectance measurements were taken on the α-Fe_2O_3-WO_3/SnO_2:F/glass samples with a Perkin Elmer Lambda Spectrophotometer fitted with an integrating sphere over the wavelength range 375 nm to 900 nm at a wavelength interval of 2 nm. The sample was irradiated from the α-Fe_2O_3-WO_3 surface. The spectral absorptance was obtained by solution of the equation $A_\lambda = (100 - R_\lambda - T_\lambda) - A_{\lambda,FTO}$.

x-ray diffraction data were obtained with Cu Kα radiation from a commercial diffractometer.

3.9.2 Photoelectrochemical characterization

The electrolyte was prepared with 18.1 MΩ-cm water with 0.5 M NaCl (Sigma Aldrich; 98%). An electrical contact was made to the SnO_2:F electrode with a conductive silver paste and copper wire. Photoelectrochemical measurements were made in an open pyrex cell fitted with 3 mm thick quartz window. A 1 cm^2 masked-off, sealed area of the sample was irradiated with a 300 W Xe bulb solar simulator with adjustable power settings through an AM 1.5G filter (Oriel; 81092). The light intensity at the sample location in the photoelectrochemical cell was 100 mW cm^{-2} as measured by a power detector (Newport; 70284). No correction was made for the optical absorption of the 4 cm of electrolyte between the quartz window and sample location. A potentiostat (Pine Instruments Bipotentiostat) was used to measure electrochemical data in a two-electrode setup using a coiled Pt wire counter electrode. N_2 gas was continuously bubbled in solution and directly over the Pt counter electrode before and during the experiment to remove any dissolved O_2 and therefore suppress the reduction of dissolved O_2 at the counter electrode. For current-potential measurements, the potential scan was anodic (in the positive direction) and at a rate of 5 mV s^{-1}, with the light mechanically chopped every ten seconds. To measure IPCE spectrum, a monochromator was used to select wavelengths (10 nm interval) from the chopped (5 Hz) output of a 70 W Xe bulb solar simulator. The incident photon flux at each wavelength

was measured by diverting a portion of the beam with a beam splitter into a calibrated silicon photodiode.

3.9.3 Ultrafast transient absorption spectroscopy

The ultrafast laser system is based on a Quantronix femtosecond laser system,[74] consisting of an Er-doped fiber oscillator, a regenerative/multi-pass amplifier, and a diode-pumped, Q-switched, second harmonic Nd:YLF pump laser (527 nm, 10 W capacity). Before injection into the amplifier, chirped pulse amplification is performed to temporally stretch, amplify, and recompress the initial short pulse, resulting in a pulse near its original duration, albeit with a vastly higher energy level (sub-nJ raised to mJ). After amplification, the as-generated fundamental (795 nm) is beam-split to generate both a white light continuum (WLC) probe pulse as well as feeding a tunable optical parametric amplifier (OPA) consisting of two delay stages: a signal pre-amplification stage and a power amplification stage. The output of the OPA was passed through wavelength separators in order to achieve a tunable pump wavelength. The system operates at 750 Hz repetition rate.

The final output was ca. 130 fs pulses centered at 540 nm excitation wavelength which was attenuated with neutral density filters. The pump beam was overlapped spatially and temporally with the WLC probe beam at the sample. The time delay between the pump and probe beams was controlled by a translation stage with 1 μm resolution. Each sample was tested for four cycles to achieve a lower-noise average response.

3.10 References for Chapter 3

1. A. Brinkman, M. Huijben, M. van Zalk, J. Huijben, U. Zeitler, J. C. Maan, W. G. van der Wiel, G. Rijnders, D. H. A. Blank, and H. Hilgenkamp, *Nature Mat*. **6**, 493 (2007).
2. A. Ohtomo and H.Y. Hwang, *Nature* **427**, 423 (2004).
3. J. Garcia-Barriocanal, A. Rivera-Calzada, M. Varela, Z. Sefrioui, E. Iborra, C. Leon, S. J. Pennycook, and J. Santamaria*, Science* **321**, 676 (2008).
4. L. Duan, L. Tong, Y. Xu, and L. Sun, *Energy Environ. Sci.* **4**, 3296 (2011).
5. *On Solar Hydrogen & Nanotechnology*, Ed: L. Vayssieres, John Wiley & Sons, Singapore, 2009.
6. X. Chen, S. Shen, L. Guo, and S. S. Mao, *Chem. Rev.* **110**, 6503 (2010).
7. M. G. Walter, E. L. Warren, J. R. McKone, S. W. Boettcher, Q. Mi, E. A. Santori, and N. S. Lewis, *Chem. Rev.* **110**, 6446 (2010).
8. Y. Lin, G. Yuan, S. Sheehan, S. Zhou, and D. Wang, *Energy Environ. Sci.* **4**, 4862 (2011).
9. K. Sivula, F. Le Formal, and M. Grätzel, *ChemSusChem* **4**, 432 (2011).
10. J. Sun, D. K. Zhong, and D. R. Gamelin, *Energy Environ. Sci.* **3**, 1252 (2010).

11. Y. Lin, G. Yuan, R. Liu, S. Zhou, S. W. Sheehan, and D. Wang, *Chem. Phys. Lett.* **507**, 209 (2011).

12. A. J. Nozik, *Nano Lett*. **10**, 2735 (2010).

13. H. A. Atwater and A. Polman, *Nature Mat*. **9**, 205 (2010).

14. P. V. Kamat, *J. Phys. Chem. C* **111**, 2834 (2007).

15. *Nanostructured and Photoelectrochemical Systems for Solar Photon Conversion,* Eds: M. D. Archer, A. J. Nozik*,* Imperial College Press, London, 2008.

16. X. Chen and S. S. Mao, *Chem. Rev.* **107**, 2891 (2007).

17. H. G. Park and J. K. Holt, *Energy Environ. Sci.* **3**, 1028 (2010).

18. M. C. Putnam, S. W. Boettcher, M. D. Kelzenberg, D. B. Turner-Evans, J. M. Spurgeon, E. L. Warren, R. M. Briggs, N. S. Lewis, and H. A. Atwater, *Energy Environ. Sci.*, **3**, 1037 (2010).

19. M. D. Kelzenberg, S. W. Boettcher, J. A. Petykiewicz, D. B. Turner-Evans, M. C. Putnam, E. L.Warren, J. M. Spurgeon, R. M. Briggs, N. S. Lewis, and H. A. Atwater, *Nature Mat.* **9**, 239 (2010).

20. I. Thomann, B. A. Pinaud, Z. Chen, B. M. Clemens, T. F. Jaramillo, and M. L. Brongersma, *Nano Lett.* **11**, 3440 (2011).

21. L. Vayssieres, A. Hagfeldt, and S. -E. Lindquist, *Pure Appl. Chem.* **72**, 47 (2000).

22. N. S. Lewis, *J. Electroanal. Chem.* **508**, 1 (2001).

23. M. Grätzel, *Inorg. Chem.* **44**, 6841 (2005).

24. X. Chen, L. Liu, P. Y. Yu, and S. S. Mao, *Science* **331**, 746 (2011).

25. H. Zhong, Y. Zhou, Y. Yang, C. Yang, and Y. Li, *J. Phys. Chem. C* **111**, 6538 (2007).

26. H. J. Snaith and C. Ducati, *Nano Lett.* **10**, 1259 (2010).

27. N. O. V. Plank, I. Howard, A. Rao, M. W. B. Wilson, C. Ducati, R. S. Mane, J. S. Bendall, R. R. M. Louca, N. C. Greenham, H. Miura, R. H. Friend, H. J. Snaith, and M. E. Welland, *J. Phys. Chem. C* **113***,* 18515 (2009).

28. H. H. Kung, H. S. Jarrett, A.W. Sleight, and A. Ferretti, *J. Appl. Phys.* **48**, 2463 (1977).

29. A. Paracchino, V. Laporte, K. Sivula, M. Grätzel, and E. Thimsen, *Nature Mat*. **10**, 456 (2011).

30. K. Ernst, A. Belaidi, and R. Könenkamp, *Semicond. Sci. Technol.* **18**, 475 (2003).

31. J. A. Glasscock, PhD Thesis, University of New South Wales, Australia, 2008, 1-220.

32. K. Sivula, F. Le Formal, and M. Grätzel, *Chem. Mater.* **21**, 2862 (2009).

33 W. Smith, A. Wolcott, R. C.Fitzmorris, J. Z. Zhang, and Y. Zhao *J. Mater. Chem.* **21**, 10792 (2011).

34. J. H. Park, O. O. Park, and S. Kim, *Appl. Phys. Lett.* **89**, 163106 (2006).

35. J. Su, L. Guo, N. Bao, and C. A. Grimes, *Nano Lett.* **11**, 1928 (2011).

36. K. -S. Ahn, Y. Yan, M. -S. Kang, J. -Y. Kim, S. Shet, H. Wang, J. Turner, and M. Al-Jassim, *Appl. Phys. Lett.* **95**, 022116 (2009).

37. S. J. Hong, S. Lee, J. S. Jang, and J. S. Lee, *Energy Environ. Sci.* **4**, 1781 (2011).

38. P. Chatchai, Y. Murakami, S. -y. Kishioka, A. Y. Nosaka, and Y. Nosaka, *Electrochim. Acta* **54**, 1147 (2009).

39. Y. Wang, T. Yu, X. Chen, H. Zhang, S. Ouyang, Z. Li, J. Ye, and Z. Zou*, J. Phys. D: Appl. Phys.* **40**, 3925 (2007).

40. W. Luo, T. Yu, Y. Wang, Z. Li, J. Ye, and Z. Zou, *J. Phys. D: Appl. Phys.* **40**, 1091 (2007).

41. F. -T. Liou, C. Y. Yang, and S. N. Levine, *J. Electrochem. Soc*. **129**, 342 (1982).

42. T. Kishi and M. Aritsuka, *Surf. Coat. Tech.* **34**, 345 (1998).

43. F. Le Formal, N. Tétreault, M. Cornuz, T. Moehl, M. Grätzel, and K. Sivula, *Chem. Sci*. **2**, 737 (2011).

44. T. Hisatomi, F. Le Formal, M. Cornuz, J. Brillet, N. Tétreault, K. Sivula, and M. Grätzel, *Energy Environ. Sci*. **4**, 2512 (2011).

45. J. Augustynski, G. Calzaferri, J. C. Courvoisier, and M. Grätzel, in *Proc. of the 11th World Hydrogen Energy Conference*, Eds: T. N. Veziroglu, C. J. Winter, J. P. Baselt, and G. Kreysa, Stuttgart, 1996, 2379.

46. E. L. Miller, R. E. Rocheleau, and X. M. Deng, *Int. J. Hydrogen Energy* **28**, 615 (2003).

47. J. Augustynski, R. Solarska, H. Hagemann, and C. Santato in *Proc. SPIE,* **6340**, Ed. L. Vayssieres*, SPIE Press,* Bellingham, 2006, 63400J-1.

48. L. Vayssieres, N. Beermann, S.-E. Lindquist, and A. Hagfeldt, *Chem. Mater.* **13**, 233 (2001).

49. L. Vayssieres, C. Sathe, S. M. Butorin, D. K. Shuh, J. Nordgren, and J. Guo, *Adv. Mater.* **17**, 2320 (2005).

50. K. Wang, J. Chen, W. Zhou, Y. Zhang, Y. Yan, J. Pern, and A. Mascarenha, *Adv. Mater.* **20**, 3248 (2008).

51. N. Beermann, L. Vayssieres, S. -E. Lindquist, and A. Hagfeldt, *J. Electrochem. Soc.* **147**, 2456 (2000).

52. M. P. Dare-Edwards, J. B. Goodenough, A. Hamnett, and P. R. Trevellick, *J. Chem. Soc., Faraday Trans. 1***79**, 2027 (1983).

53. M. A. Butler, *J. Appl. Phys.* **48**, 1914 (1977).

54. J. H. Kennedy and K. W. Frese, *J. Electrochem. Soc.* **125**, 709 (1978).

55. A. B. Murphy, P. R. F. Barnes, L. K. Randeniya, I. C. Plumb, I. E. Grey, M. D. Horne, and J. A. Glasscock, *Int. J. Hydrogen Energy* **31**, 1999 (2006).

56. T. Lindgren, H. Wang, N. Beermann, L. Vayssieres, A. Hagfeldt, and S. -E. Lindquist, *Sol. Energy Mat. & Sol. Cells*, 2002, **71**, 231-243.

57. M. Grätzel, *Nature* **414**, 338 (2001).

58. J. Chakhalian, W. Freeland, H. -U. Habermeier, G. Cristiani, G. Khaliullin, M. van Veenendaal, and B. Keimer, *Science* **318**, 1114 (2007).

59. C. X. Kronawitter, J. R. Bakke, D. A. Wheeler, W. -C. Wang, C. Chang, B. R. Antoun, J. Z. Zhang, J. Guo, S. F. Bent, S. S. Mao, and L. Vayssieres, *Nano Lett*. **11**, 3855 (2011).

60. J. Nelson, *Phys. Rev. B* **59**, 15374 (1999).

61. F. Cao, G. Oskam, G. J. Meyer, and P. C. Searson, *J. Phys. Chem.* **100**, 17021 (1996).

62. I. Cesar, K. Sivula, A. Kay, R. Zboril, and M. Grätzel, *J. Phys. Chem. C* **113**, 772 (2009).

63. A. Królikowska, P. Barczuk, R. Jurczakowski, and J. Augustynski, *J. Electroanal. Chem.* **662**, 229 (2011).

64. Y. Ling, G. Wang, D. A. Wheeler, J. Z. Zhang, and Y. Li, *Nano Lett.* **11**, 2119 (2011).

65. F. J. Morin, *Phys. Rev.* **93**, 1195 (1964).

66. N. J. Cherepy, D. B. Liston, J.A. Lovejoy, H. Deng, and J. Z. Zhang, *J. Phys. Chem. B* **102**, 770 (1998).

67. A. G. Joly, J. R. Williams, S. A. Chambers, G. Xiong, W. P. Hess, and D. M. Laman, *J. Appl. Phys.* **99**, 053521 (2006).

68. V. A. Nadtochenko, N. N. Denisov, V. Y. Gak, F. E. Gostev, A. A. Titov, O. M. Sarkisov, and V. V. Nikandrov, *Russ. Chem. Bull. Int. Ed*. **51**, 457 (2002).

69. Y. P. He, Y. M. Miao, C. R. Li, S. Q. Wang, L. Cao, S. S. Xie, G. Z. Yang, B. S. Zou, and C. Burda, *Phys. Rev. B* **71**, 125411 (2005).

70. N. M. Dimitrijevic, D. Savic, O. I. Micic, and A. J. Nozik, *J. Phys. Chem.* **88**, 4278 (1984).

71 A. J. Cowan, C.J. Barnett, S.R. Pendlebury, M. Barroso, K. Sivula, M. Gratzel, J.R. Durrant, and D.R. Klug, *J. Am. Chem. Soc.* **133**, 10134 (2011).

72. S. R. Pendlebury, M. Barroso, A. J. Cowan, K. Sivula, J. Tang, M. Grätzel, D. Klug, and J. R. Durrant, *Chem. Commun.* **47**, 716 (2011).

73. P. Zubko, S. Gariglio, M. Gabay, P. Ghosez, and J. -M. Triscone, *Annu. Rev. Condens. Matter Phys.* **2**, 141 (2011).

74. R. J. Newhouse, H. Wang, J. K. Hensel, D. A. Wheeler, S. Zou, and J. Z. Zhang, *J. Phys. Chem. Lett.* **2**, 228 (2011).

4 Engineering impurity distributions in photoelectrodes for solar water oxidation

Chapter 4 is an adaptation of a published article:

Coleman X. Kronawitter, Zhixun Ma, Dongfang Liu, Samuel S. Mao, and Bonnie R. Antoun, Engineering impurity distributions in photoelectrodes for solar water oxidation, *Adv. Energy Mater.* **2**, 52 (2012).

The majority of the work in this chapter was supported by Sandia National Laboratories. Sandia National Laboratories is a multi-program laboratory managed and operated by Sandia Corporation, a wholly owned subsidiary of Lockheed Martin Corporation, for the U.S. Department of Energy's National Nuclear Security Administration under contract DE-AC04-94AL85000.

4.1 Abstract for Chapter 4

Chapter 3 provided a detailed description of the use of oxide hetero-nanostructures in solar water oxidation photoanodes. Designs for these composite electrodes attempt to combine the complementary properties of dissimilar oxides, including optical absorption, transport, and kinetic properties. Chapter 4 builds on these concepts, but attempts to accomplish this goal through the use of a single oxide phase.

This chapter introduces and experimentally verifies the conceptual framework for the design of solar water oxidation photoelectrodes based on the spatially inhomogeneous doping of metal oxide nanostructures. Optical absorption and electronic conduction can be decoupled and optimized by spatially segregating the functional impurity species that facilitate their associated physical processes. The nanostructure regions possess functional specificity that is established by their chemical composition and three-dimensional geometry, which includes volume, orientation with respect to the direction of light propagation, as well as proximity to the semiconductor-liquid interface. Experimental results indicate optical absorption at visible wavelengths and the related water oxidation conversion efficiencies can be enhanced by physically distributing absorbing crystallites along the direction of light propagation while maintaining their close proximity to the oxide-water interface. An optimization pathway based on these results, analogous to the well-known optimization procedures for excitonic photovoltaic devices, is suggested.

4.2 Introduction to Chapter 4

The distinction between electricity and fuel use in analyses of global power consumption statistics highlights the critical importance of establishing efficient synthesis techniques for solar fuels—those chemicals whose bond energies are obtained through conversion processes driven

by solar energy.[1] Photoelectrochemical (PEC) processes show potential for the production of solar fuels because of their demonstrated versatility in facilitating optoelectronic and chemical conversion processes.[2] Tandem PEC-photovoltaic modular configurations for the generation of hydrogen from water and sunlight (solar water splitting) provide an opportunity to develop a low-cost and efficient energy conversion scheme.[3,4] The critical component in devices of this type is the PEC photoelectrode, which must be optically absorptive, chemically stable, and possess the required electronic band alignment with the electrochemical scale for its charge carriers to have sufficient potential to drive the hydrogen and oxygen evolution reactions. After many decades of investigation, the primary technological obstacle remains the development of photoelectrode structures capable of efficient conversion of light with visible frequencies, which is abundant in the solar spectrum.[5] Metal oxides represent one of the few material classes that can be made photoactive and remain stable to perform the required functions.[6,7] This report presents a strategy to decouple the crucial optical absorption and electronic transport processes required for operation of metal oxide photoelectrodes by spatially segregating the functional impurity concentrations that facilitate their associated physical processes.

One technique to sensitize metal oxides to visible light is to introduce dopants that are associated with visible-light-active electronic transitions.[8,9] If dopant species are introduced in low concentration, below the substitutional limit in the host oxide lattice, optical spectroscopy measurements of films and particle suspensions (typical photoelectrode and photocatalyst configurations) commonly indicate weak shoulders associated with dopant-induced light absorption relative to the host's band-edge absorption.[10] This observation relates to the comparably lower density of states of absorbing impurity levels within the host oxide band structure: because the solubilities of many dopants of interest are restricted to a few atomic percent,[8] for nearly equivalent cross sections dopant-induced absorption is expected to be an inherently weaker process than absorption directly affected by the host oxide band structure. Heavily doping beyond the substitutional limit will assist further in sensitization, but with an associated sacrifice of crystallographic order in the surrounding lattice.

Consequently, in order to achieve optical thickness at these weakly absorbing wavelengths, the path length within the electrode structure must be increased, which for conventional film-based electrodes requires the fabrication of physically thick structures. The use of thick films, however, is problematic because of the generally poor transport of carriers in metal oxides, and especially carriers associated with isolated impurity states. The disparity between absorption lengths and transports lengths in oxide materials of interest for this application is addressed generally in the growing literature dedicated to the use of nanotechnologies for solar PEC hydrogen generation.[7]

These observations suggest that doping traditional metal oxide photoelectrodes presents the unacceptable situation where many free carriers generated by visible light excitations recombine before reaching the rear contact or reacting electrochemically at the oxide-liquid interface. Consequently, a viable strategy to enhance the conversion efficiencies of doped metal oxide-based photoelectrodes should be to decouple the optical absorption and electronic conduction processes that occur during their operation. In order to accomplish this, the electrode architecture must be designed such that the associated physical phenomena are segregated, while maintaining spatial register among the facilitating structure regions.

Fortunately, the technological implementation of weakly absorptive materials with poor charge transport properties has been comprehensively addressed in the various designs for metal-oxide-containing excitonic photovoltaic devices.[11] In these devices, organic dyes[12] or semiconductor nanocrystals[13] are intimately contacted with media whose operational purpose is to selectively accept (or separate) and transport photogenerated charges for collection in an external circuit. This configuration has also been applied toward the photoelectrochemical generation of hydrogen in electrolytes containing sacrificial reagents to considerable success.[14] If the concept is applied toward the fabrication of metal oxide photoelectrodes for water splitting an analogy can be drawn between the sensitizer phase and a doped, visible-light-active oxide crystal, in that both of these materials are optically absorptive in the spectral range of interest but efficiently transport charges only over short physical distances. Deposition onto nanostructured substrates permits the use of absorber layers with small physical thickness but large optical thickness (as realized for example in extremely-thin-absorber photovoltaic cells[15] and α-Fe_2O_3 photoanodes[16,17]). If the substrate is of the same character as the sensitizer phase, the conceptual outcome of this application is a single-phase, oxide nanostructure that is inhomogeneously doped to perform the optoelectronic conversion processes relevant to the oxidation of water using solar energy. The isostructural nature of the absorbing and conducting regions in this case has the potential to yield low concentrations of interface recombination centers, which has significant consequences on the overall conversion efficiencies of PEC devices.

4.3 Results and Discussion

The concept is presently demonstrated with ZnO nanostructures doped in core regions with shallow Al donor levels for enhanced electronic conduction and in the near-surface volume with intragap Ni impurity states for increased optical absorption. However, the strategy is quite general and can be applied to numerous oxides and impurities; additional experiments were conducted with photoactive nitrogen impurities in place of nickel, with similar, albeit less-pronounced, PEC performance enhancements evident. Figure 4-1provides electron microscopy images of the complete structures as well as a schematic of the proposed operating mechanisms within the oxide structure described later in this report; its composition is discussed in detail below. The change in morphology upon introduction of ZnO:Ni is shown in Figure 4-6.

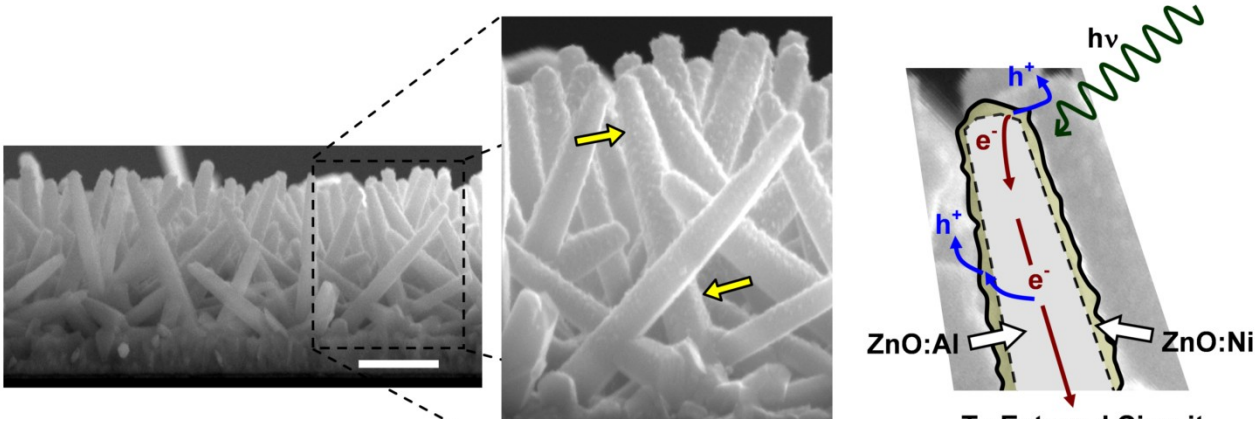

Figure 4-1 Scanning electron microscopy images of ZnO nanostructure arrays, with yellow arrows highlighting doped crystallites distributed approximately 1.5 μm along the direction of light propagation. White scale bar indicates 1 μm. Right hand side provides a schematic of idealized operating mechanisms overlayed onto the tip of an individual nanostructure.

Substitutional Al is a shallow donor in the ZnO nanocrystal lattice and is associated with large increases electronic conductivity, which results from an order of magnitude increase in carrier concentration.[18] The ionization energy of Al states has been measured to be approximately 90 meV.[19] It is therefore identified as a suitable dopant to facilitate enhanced electronic conduction to the rear contact during PEC operation.

Visible light sensitization on the other hand involves the introduction of impurity states deeper within the bandgap of ZnO. Substitutional impurities on the cation site can be used to functionally sensitize ZnO crystals if they introduce impurity levels or bands that are situated at potentials meeting the thermodynamic requirement for water oxidation. The requirement is met by a number of transition metal impurities; the mechanism by which these impurities sensitize ZnO to visible wavelengths will be discussed later in this report.

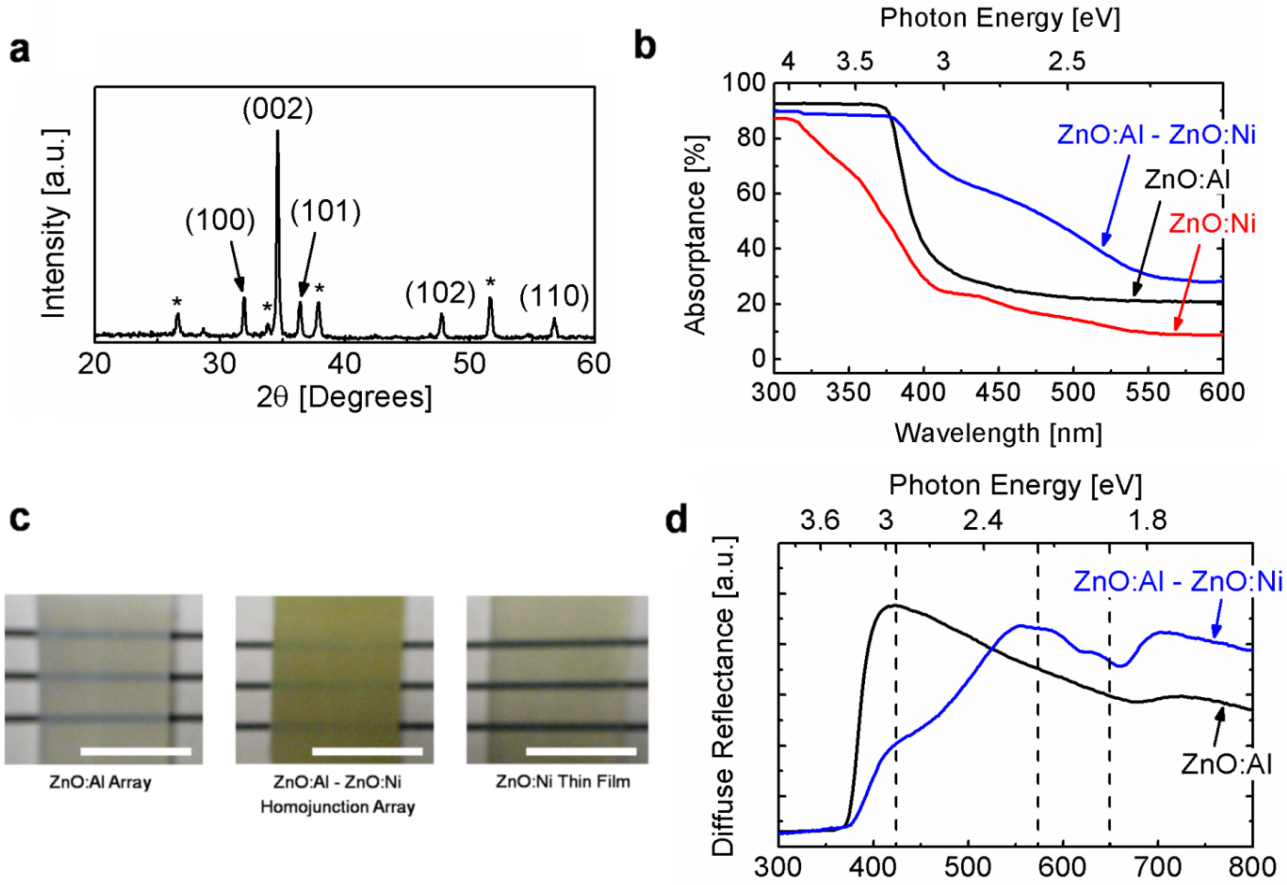

Figure 4-2 Structural and optical characterization of ZnO nanostructure arrays with and without ZnO:Ni modification: (a) x-ray diffraction pattern of final ZnO nanostructure array. Hexagonal ZnO (wurtzite) is indexed; tetragonal SnO_2 (cassiterite) substrate peaks indicated by *. (b) Absorptance spectra ($A_\lambda = 100 - T_\lambda - R_\lambda$) of ZnO/FTO/glass structures. (c) Phtographs of ZnO:Al array (left), ZnO:Al – ZnO:Ni array (middle), and ZnO:Ni thin film (right). White scale bars indicate 1 cm. (d) Diffuse reflectance spectra; dashed lines electronic transitions established in the literature for Ni(II) with tetrahedral symmetry in the ZnO lattice (see main text for details).

An x-ray diffraction pattern (Figure 4-2a) after fabrication indicates the presence of hexagonal ZnO and the tetragonal SnO_2 substrate (FTO). The ZnO is highly (002)-textured, which results from the c-axis alignment of nanostructures normal to the substrate. The small unlabeled peaks around 26° and 56° were present in all ZnO samples regardless of dopant composition, and are tentatively attributed to a contamination artifact from the fabrication procedure.

The optical absorptance spectra of ZnO nanostructure arrays deposited onto FTO substrates with and without the introduction of crystallites doped with Ni are shown in Figure 4-2b. The absorption features beyond 400 nm are associated with a change in sample color from transparent-white to green (see sample photographs in Figure 4-2c), which is consistent with previous reports.[20] A reference ZnO:Ni thin film, deposited under identical conditions directly onto the FTO substrate, is also included in Figure 4-2b and Figure 4-2c. Comparison of these

optical properties highlights the dramatic increase in optical thickness at visible wavelengths that is associated with the nanostructured homojunction architecture.

The broad absorption features at long wavelengths overlap with transitions associated with tetrahedrally coordinated Ni(II) in the ZnO lattice. Examination of the diffuse reflectance spectra for ZnO:Al and ZnO:Al-ZnO:Ni on FTO/glass substrates in Figure 4-2d provides additional resolution for these transitions. The dashed lines in this figure indicate the known electronic transitions associated with Ni(II) with tetrahedral symmetry (the transitions at 2.14 eV and 1.89 eV correspond to $^3T_1(F) \rightarrow {}^3T_1(P)$ for $Ni^{2+}_{tet}: 3d^8$).[20,21] The plot indicates reflectance features at these wavelengths that are introduced along with Ni-doped ZnO crystallites, which suggest a tetrahedral coordination of Ni(II).

Photoelectrochemical characterization of the ZnO/FTO electrodes in aqueous 0.5 M Na_2SO_4 provides confirmation of the concept's successful application toward visible-light-driven solar water splitting. Current-potential curves (Figure 4-3a) indicate a monotonic photocurrent increase with applied anodic potential until the onset of dark current, which suggests effective charge separation at the semiconductor-liquid junction.[22] Insertion of a UV filter in the optical path, which eliminates wavelengths below 410 nm, causes a moderate decrease in photocurrent response. The magnitude of the contribution of UV-driven photoactivity to total activity is explained by the comparably small UV photon flux available in solar (simulated) light (~5% of spectral intensity). Amperometric (current-time) measurements with application of color filters shown in Figure 4-3b indicate the portion of total photocurrent driven by visible light. In these conditions approximately 44% of total photocurrent originates from wavelengths beyond 410 nm; 4.4% originates from beyond 510 nm. Similar analyses of ZnO electrodes without Ni indicate the photocurrent is almost completely UV-driven (see Figure 4-12).

The incident photon conversion efficiency (*IPCE*) at visible wavelengths for front-side irradiation and with +1 V applied versus a Pt counter electrode is presented in Figure 4-3c. There is a marked decrease (*ca*. 4 times) of UV photoactivity upon addition of ZnO:Ni species (see Figure 4-11), which can be understood by observation that all photoholes originating from UV excitation must pass through impure visible-light-active crystals at the ZnO-water interface. Efficiency losses of this type can be minimized through the general optimization of electrode architecture, as discussed below.

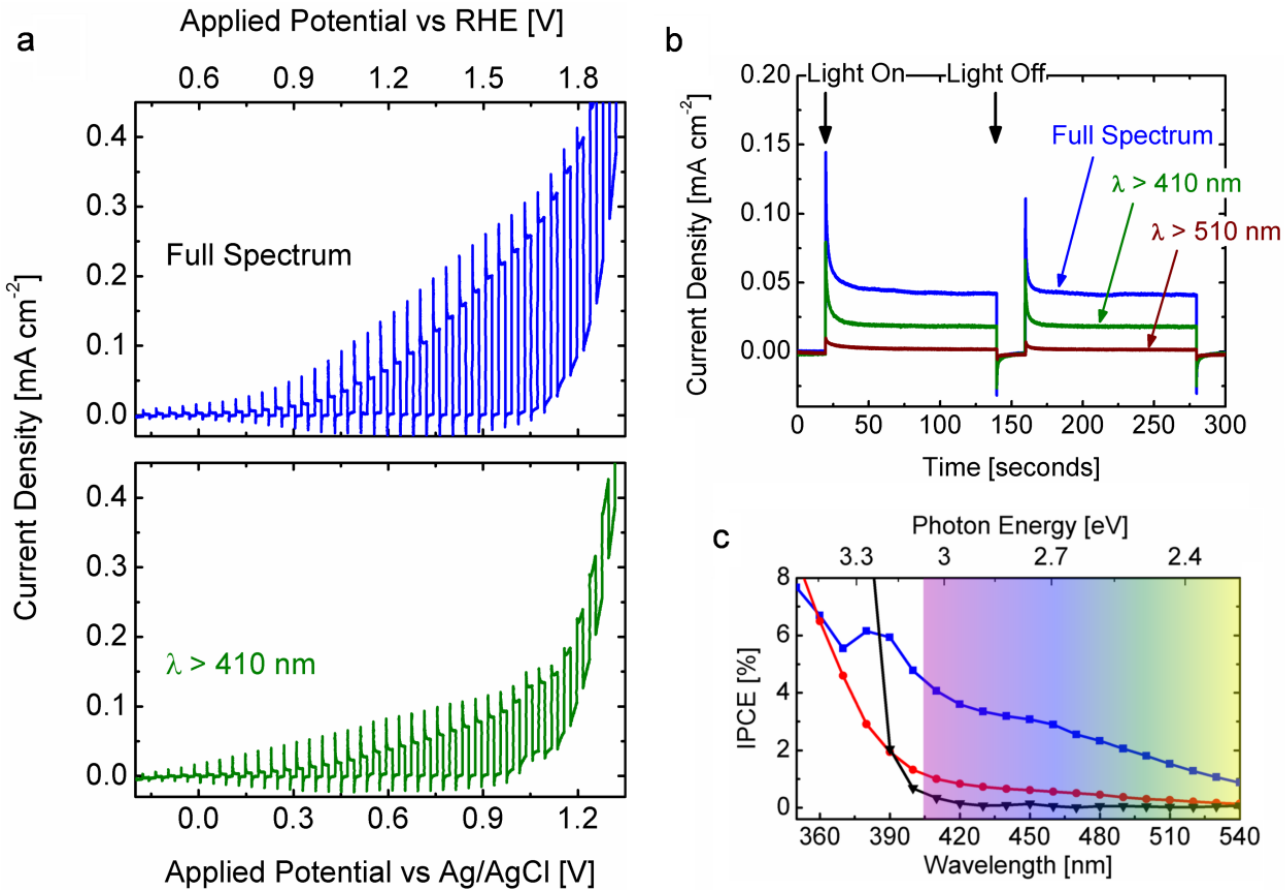

Figure 4-3 Photoelectrochemical characterization of ZnO electrodes in 0.5 M Na2SO4: (a) Current density-potential curve under chopped AM 1.5G-filtered 100 mW cm-2 solar-simulated irradiation with and without application of a UV filter. (b) Amperometric (current-time) measurement at 0.6 V versus Ag/AgCl with chopped AM 1.5G-filtered 100 mW cm-2 irradiation, with application of wavelength filters. (c) Incident photon conversion efficiency at visible wavelengths for ZnO:Al-ZnO:Ni homojunction array (blue squares), ZnO:Ni thin film (red circles), and ZnO:Al nanorod array (black triangles), with +1 V applied versus a Pt counter electrode

.

To investigate the effect of the homojunction architecture on visible-light-driven water oxidation efficiency, the *IPCE* spectrum of a dense ZnO:Ni thin film deposited under identical conditions is compared to the nanostructured homojunction array. Presented in Figure 4-3c, these data indicate that approximately a three-fold enhancement in conversion efficiencies for solar-abundant visible wavelengths is achieved by distributing the absorptive species normal to the substrate and along the direction of light propagation. It is determined that the design effectively shifts the spectral photocurrent response of ZnO electrodes toward lower energies abundant in the solar spectrum.

D. Fichou *et al.* examined the spectral photocurrent contribution toward water oxidation of isovalent Mn^{2+}, Co^{2+}, and Ni^{2+} dopants in ZnO polycrystalline photoanodes.[20] It was suggested that visible light photoactivity originated from *d-d* transitions within the dopant ion, with subsequent charge transfer into the ZnO band structure. In this interpretation, photoelectrons originating from impurity $3d^n$ excitations were transferred to the ZnO conduction band (Zn $4s^0$ orbitals); holes were transported to the ZnO-electrolyte interface in a defect band and were electrochemically active in a buffered Na_2SO_4 solution.

More recently however, work from D. R. Gamelin and coworkers[23-26] has unambiguously determined that charge transfer states are required to generate observable photocurrents associated with transition metal dopants in ZnO. Based on these previous analyses of ZnO:Co[24] and ZnO:Ni,[23] excitations with wavelengths near 430 nm can be assigned to an acceptor-type ionization, where an electron is promoted to the dopant *d*-shell orbitals from ZnO-based donor orbitals of the valence band.[24] If the ZnO lattice is considered a ligand of the dopant ion, these transitions fit the general description of ligand-to-metal charge transfer transitions. The excited state of the charge transfer transition in this case is a valence band hole Coulombically bound to a Ni^+ dopant ion. This can be deduced from the numerous previous analyses of isovalent transition metal dopants in ZnO and other II-VI semiconductor lattices.[23,24,26,27] These references suggest the excitation can be described as

$$Ni^{2+} + hv \rightarrow Ni^{+} + h^{+}_{VB}. \qquad (4\text{-}1)$$

The bound carrier generated from this excitation should possess a hydrogen-like wavefunction[23] and a potentially large orbital radius,[27] but one which is reduced relative to a free hole. In the context of this assignment, it is clear that the efficient utilization of valence band charge transfer transitions for solar water oxidation will require the use of thin doped regions that are located in close proximity to the electrolyte.

Based on these optical and photoelectrochemical data and the literature cited in this article, some conclusions can be drawn regarding the electronic band structures of the inhomogeneously doped nanostructures. The carrier transfer under irradiation, confirmed by the above photoelectrochemical characterization, was depicted schematically in the right hand side of Figure 4-1. The band diagram in Figure 4-4 reflects the theoretical understanding of photoanode operation established in the literature[28] but is augmented by the literature-derived electronic states matching the profiles in the structures.

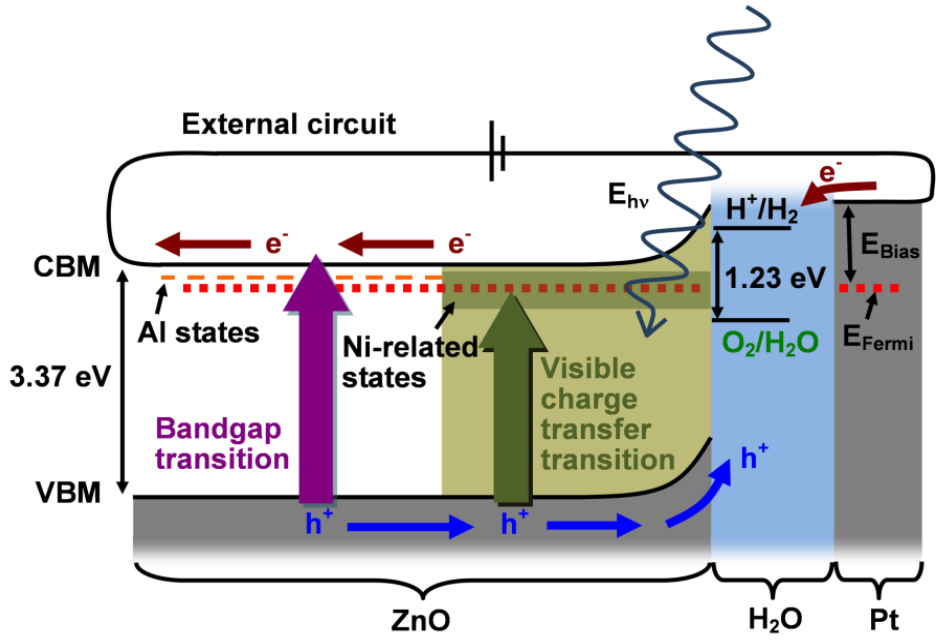

Figure 4-4 Idealized energetics of the functional homojunction nanostructures demonstrated in this study. Note that surface/interface and other defect states are likely to be present but are omitted in the diagram as they were not studied experimentally. Relative positions of electronic states are schematic but based on literature values (see main text).

In order to investigate the nature of the observed efficiency enhancements at visible wavelengths, the internal quantum efficiency, or absorbed photon conversion efficiency, of the samples were calculated. These efficiencies were calculated through the following equations:

$$T_{measured} = T_1 \times T_2 \times \ldots T_n \tag{4-2}$$

$$T_{\lambda,\,film} = \frac{T_{\lambda,\,measured}}{T_{\lambda,\,substrate}} \tag{4-3}$$

$$A_\lambda = ln\left(T_{\lambda,\,film}\right) \tag{4-4}$$

$$LHE_\lambda = 1 - e^{A_\lambda} \tag{4-5}$$

$$APCE_\lambda = \frac{IPCE_\lambda}{LHE_\lambda}. \tag{4-6}$$

Where T_n is the transmittance of a component in the layered structure, $T_{\lambda,film}$ is the transmittance of the film, corrected for the substrate as from equations 4-2 and 4-3, A_λ is the absorbance, LHE_λ is the light harvesting efficiency, and $APCE_\lambda$ is the absorbed photon conversion efficiency,. The *LHE* and *APCE* as calculated from the above equations are plotted in Figure 4-5. The magnitudes of the *APCE* values increase dramatically for wavelengths where there is little light absorption, which results in oscillations in the curves corresponding to those in the *LHE* spectra.

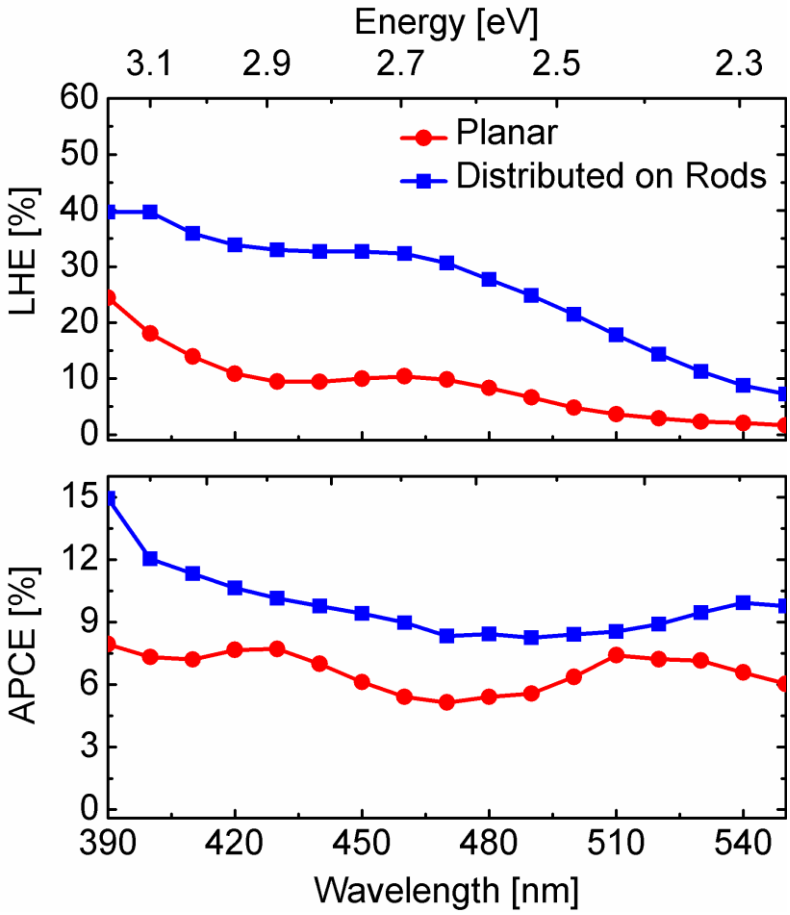

Figure 4-5 Light harvesting efficiency (top panel) and absorbed photon conversion efficiency (bottom panel) as defined in the main text. Blue squares correspond to efficiencies when ZnO:Ni is distributed on nanorods along the direction of light propagation; red circles correspond to those for a planar ZnO:Ni thin film

These curves indicate that both the *LHE* and *APCE* at visible wavelengths are increased by distributing ZnO:Ni vertically along the direction of light propagation. The variation in the *APCE* values over this spectral range may indicate differences in intrinsic escape probabilities for photogenerated electrons and holes.[24] Longer wavelength excitations may correspond to alternative excitations, such as those related to metal-to-ligand charge transfer transitions, which have different branching ratios for charge separation in their excited states. The transitions could be sensitized by an optical absorption band near 2.9 eV, which would tend to flatten the *IPCE* curve relative to the *APCE* curve. In Figure 4-5, the oscillations in *APCE* are present in both

planar and distributed configurations, which suggests they are related to the electronic structure of the material itself. More in-depth analyses of the material's electronic structure would be required to elucidate the nature of these transitions.

This observation of enhanced *LHE* and *APCE* provides confirmation of the proposed benefits of the homojunction architecture discussed above: greater *LHE* suggests an enhancement in optical absorption and greater *APCE* at visible wavelengths suggests an enhancement in charge separation. Because the thickness of the photoactive layer is reduced by distributing species over a larger surface area substrate, the design facilitates shorter carrier transport path lengths to phases where carrier extraction occurs. This result may also suggest that electrons excited from charge transfer transitions within the ZnO bandstructure are more easily transferred to the ZnO:Al phase than to the SnO_2:F substrate.

In an optimized photoelectrode, the dopant profiles within the structures should be tailored to maximize conversion efficiency, which depends on, among other quantities, the free electron mobility and concentration, minority carrier (hole) transport length, and extinction coefficient. The metal oxide's feature dimensions should be constructed to maximize both the spectral overlap of optical absorption with the terrestrial solar flux and quantity of photogenerated minority carriers reaching the oxide-water interface.

As part of an initial effort toward design optimization, the optical functions of a ZnO:Ni thin film were approximated by a combined ellipsometry-reflectometry technique (see Appendix for Chapter 4 for details), the results of which are consistent with previous measurements of metal-doped ZnO films.[29] These analyses accurately determine the complex refractive index and associated spectral absorption coefficient of the film. The light penetration depths determined by this spectral quantity (Figure 4-10) suggest that the optimal structure dimension in the direction of light propagation is on the order of several micrometers, which could be reduced by accounting for the significant light scattering effects associated with irradiation of nanowire arrays.[30]

Here again a close analogy can be drawn to the design of dye-sensitized solar cells, which require dye molecule adsorption over several micrometers of porous structure to achieve optical thickness.[12] Careful analyses of SEM images such as those in Figure 4-1 indicate the absorptive crystallites are distributed for as long as 1.5 μm along the direction of light penetration. The demonstrated efficiency enhancement in Figure 4-3c is conceptually similar to the dramatic enhancement evident in dye-sensitized solar cells when planar TiO_2 dye adsorption substrates are replaced with nanostructured TiO_2.[31] It is suggested that an optimization route for fabrication of efficient homojunction nanostructures of this type is analogous to maximization of dye loading in dye-sensitized solar cells—optimization requires the select doping of the near-surface volume of porous nanostructures over several micrometers.

There is in fact an all (electro)chemical route to the fabrication of metal oxide homojunction nanostructure arrays of the type described above. Chemical growth of ZnO and TiO_2 structures with very large aspect ratios have been reported by various techniques.[32-34] In addition, electrochemical deposition has successfully been employed in the literature to obtain conformal deposition of films into deeply-structured substrates.[15] Doped metal oxide films are routinely

fabricated by electrodeposition.[35] A two-step (electro)chemical process is therefore proposed for the fabrication of high-aspect ratio metal oxide homojunction nanostructure arrays. Such a process is expected to accomplish fabrication at low temperatures, which suggests compatibility with low-cost and flexible substrates. Experiments of this type are currently underway in the authors' laboratories. Additional future work includes the in-depth analysis of the long-term stability of the dopants and their concentration profiles under operating conditions, a theoretical prediction of the optimal electrode three-dimensional geometry based on known material properties, as well as an analysis of optimal material systems suitable for this technique.

4.4 Conclusions from Chapter 4

This report has introduced and experimentally verified the conceptual framework for the design of solar water oxidation photoelectrodes based on the spatially inhomogeneous doping of metal oxide nanostructures. Optical absorption and electronic conduction can be decoupled and optimized by spatially segregating the functional impurity species that facilitate their associated physical processes. The nanostructure regions possess functional specificity that is established by their chemical composition and three-dimensional geometry, which includes volume, orientation with respect to the direction of light propagation, as well as proximity to the semiconductor-liquid interface. Experimental results indicate optical absorption at visible wavelengths and the related water oxidation conversion efficiencies can be enhanced by physically distributing absorbing crystallites along the direction of light propagation while maintaining their close proximity to the oxide-water interface. An optimization pathway based on these results, analogous to the well-known optimization procedures for excitonic photovoltaic devices, has been suggested.

4.5 References for Chapter 4

1. N. S. Lewis and D.G. Nocera, *Proc. Nat. Acad. Of Sciences* **103,** 15729 (2006).
2. N. S. Lewis, *J. Electroanalytical Chem.* **508,** 1 (2001).
3. J. Augustynski, G. Calzaferri, J. C. Courvoisier, and M. Grätzel, in *Proc. of the 11th World Hydrogen Energy Conference* (Eds: T. N. Veziroglu, C. J. Winter, J. P. Baselt, and G. Kreysa), Stuttgart, 1996, 2379.
4. E. L. Miller, R. E. Rocheleau, and X. M. Deng, *Int. J. Hydrogen Energy* **28,** 615 (2003).
5. Walter, M. G., E. L Warren, J. R. McKone, S. W. Boettcher, Q. Mi, E. A. Santori, and N. S. Lewis, *Chem. Rev.* **110,** 6446 (2010).
6. B. D. Alexander, P. J. Kulesza, I. Rutkowska, R. Solarskac, and J. Augustynski, *J. Mater. Chem.* **18,** 2298 (2008).
7. *On Solar Hydrogen & Nanotechnology*, (Ed: L. Vayssieres), Wiley, Singapore, 2009.
8. M. A. Malati and W. K. Wong, *Surface Technology* **22,** 305 (1984).
9. K. Rajeshwar, *J Appl. Electrochem*. **37,** 765 (2007).
10. Z. Zou, J. Ye, K. Sayama, and H. Arakawa, *Nature* **414,** 625 (2001).
11. B. A. Gregg, *J. Phys. Chem. B* **107,** 4688 (2003).

12. M. Grätzel, *Inorg. Chem.* **44,** 6841 (2005).

13. A. J. Nozik, *Nano Lett.* **10,** 2735 (2010).

14. G. Wang, X. Yang, F, Qian, J. Z. Zhang, and Y. Li, *Nano Lett.* **10**, 1088 (2010).

15. K. Ernst, A. Belaidi, and R. Könenkamp, *Semicond. Sci. Technol.* **18**, 475 (2003).

16. J. Glasscock, P. R. F. Barnes, I. C. Plumb, A. Bendavid, and P. J. Martin, in *Proc. of SPIE, the International Society for Optical Engineering* (Ed. L. Vayssieres), 2006, *6340*, 63400N.

17. K. Sivula., F. Le Formal, and M. Grätzel, *Chem. Mater.* **21,** 2862 (2009).

18. R. Könenkamp, K. Boedecker, M. C. Lux-Steiner, M. Poschenrieder, F. Zenia, C. Levy-Clement, and S. Wagner, *Appl. Phys. Lett.* **77,** 2575 (2000).

19. H. P. He, Tang, Z. Z. Ye, L. P. Zhu, B. H. Zhao, L. Wang, and X. H. Li, *Appl. Phys. Lett.* **90,** 023104 (2007).

20. D. Fichou, J. Pouliquen, J. Kossanyi, M. Jakani, G. Campet, and J. Claverie, *J. Electroanal. Chem.* **188,** 167 (1985).

21. H. A. Weakliem, *J. Chem. Phys.* **36,** 2117 (1962).

22. X. Yang, A. Wolcott, G. Wang, A. Sob, R. C. Fitzmorris, F. Qian, J. Z. Zhang, and Y. Li, *Nano Lett.* **9,** 2331 (2009).

23. D. A. Schwartz, N. S. Norberg, Q. P. Nguyen, J. M. Parker, and D. R. Gamelin, *J. Am. Chem. Soc.* **125,** 13205 (2003).

24. W. K. Liu, G. Mackay Salley, and D. R. Gamelin, *J. Phys. Chem. B* **109,** 14486 (2005).

25. K. R. Kittilstved, W. K. Liu, and D. R. Gamelin, *Nature Mater.* **5,** 291 (2006).

26. C. A. Johnson, T. C. Kaspar, S. A. Chambers, G. Mackay Salley, and D. R. Gamelin, *Phys. Rev. B.* **48,** 8672 (1993).

27. J. M. Noras and J. W. Allen, *J. Phys. C.: Solid St. Phys.* **13,** 3511 (1980).

28. A. J. Nozik and R. Memming, *J. Phys. Chem.* **100,** 13061 (1996).

29. A. Mendoza-Galván, C. Trejo-Cruz, J. Lee, D. Bhattacharyya, J. Metson, P. J. Evans, and U. Pal, *J. Appl. Phys.* **99,** 014306 (2006).

30. M. D. Kelzenberg, S. W. Boettcher, J. A. Petykiewicz, D. B. Turner-Evans, M. C. Putnam, E. L.Warren, J. M. Spurgeon, R. M. Briggs, N. S. Lewis, and H. A. Atwater, *Nature Mater.* **9,** 239 (2010).

31. M. Grätzel, *Nature* **414,** 338 (2001).

32. M. Law, L. E. Greene, J. C. Johnson, R. Saykally, and P. Yang, *Nature Mater.* **4,** 455 (2005).

33. X. Feng, K. Shankar, O. K. Varghese, M. Paulose, T. J. Latempa, and C. A. Grimes, *Nano Lett.* **8,** 3781 (2008).

34. G. K. Mor, K. Shankar, M. Paulose, O. K. Varghese, and C. A. Grimes, *Nano Lett.* **6,** 215 (2006).

35. T. F. Jaramillo, S.-H. Baeck, A. Kleiman-Shwarsctein, K.-S. Choi, G. D. Stucky, and E.W. McFarland, *J. Comb. Chem.* **7,** 264 (2005).

4.6 Appendix for Chapter 4

4.6.1 Extended morphology characterization

4.6.1.1 *Top-down images of ZnO:Al-ZnO:Ni system*

Top-down scanning electron microscopy (SEM) images of the rod arrays before and after modification with ZnO:Ni are provided in Figure 4-6.

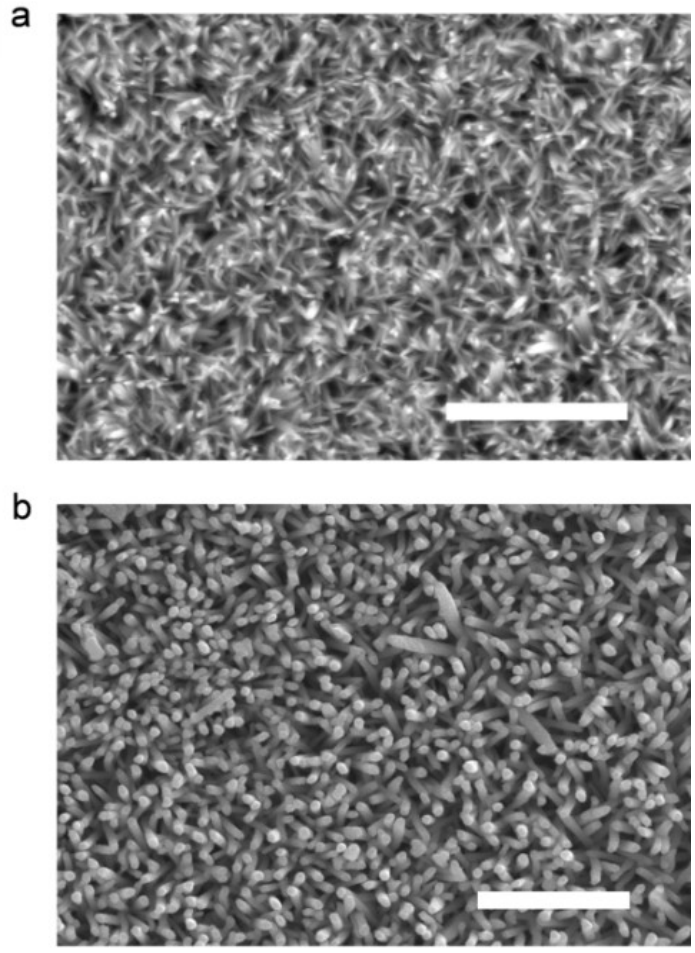

Figure 4-6 Top-down SEM images of ZnO nanorod arrays before (a) and after (b) modification with ZnO:Ni. White scale bars indicate 2.5 μm

4.6.1.2 *Effect of substrate temperature on morphology of pulsed laser deposited coating*

Additional experiments were conducted where the substrate temperature was maintained at 100 °C and 300 °C during pulsed laser deposition onto the nanostructured ZnO substrate. These experiments were not standardized, but are intended to give a rough understanding of the effect of deposition temperature of surface morphology. It is evident in Figure 4-7 and Figure 4-8 that there is a significant difference in morphology for the two temperatures. The film deposited at 100 °C (Figure 4-7) has considerable roughness and is generally distributed toward the tops of rods. The film deposited at 300 °C (Figure 4-8) is smooth, and it appears that crystals are distributed along the length of the rod, which can perhaps be attributed to increased diffusion of deposited species on the substrate.

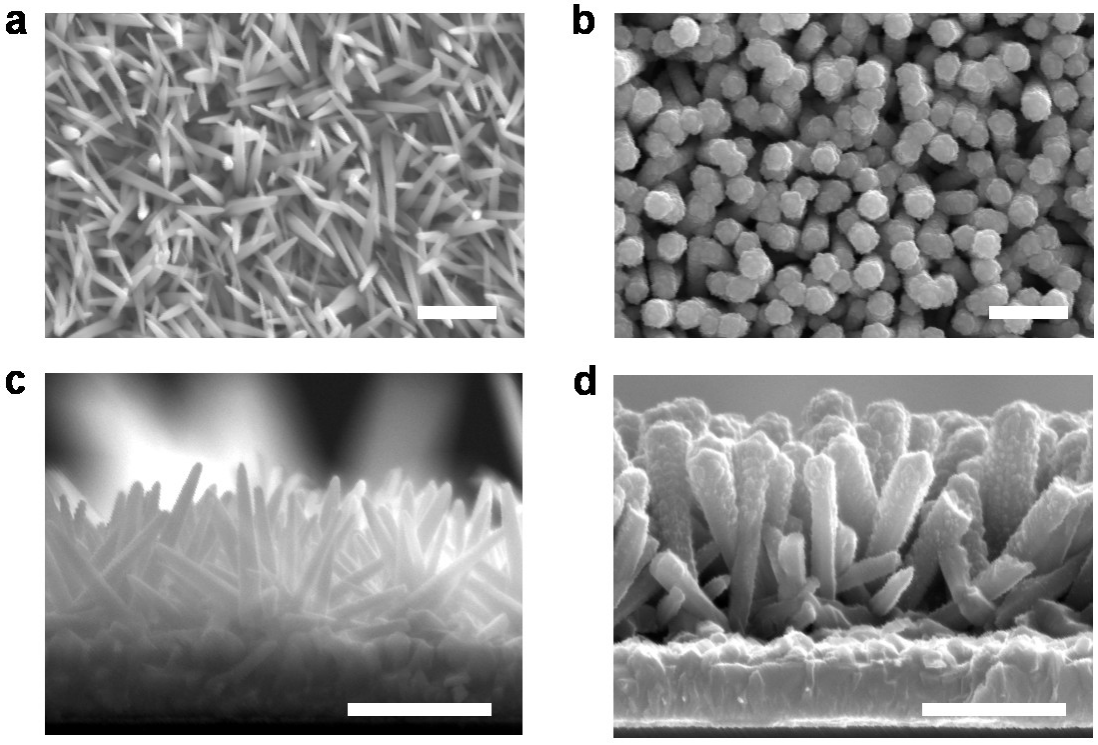

Figure 4-7 Morphology of pulsed laser deposited material at substrate temperature of 100 ºC. Top-down (a and b) and cross-sectional (c and d) SEM images of ZnO nanorod arrays before (a and c) and after (b and d) pulsed laser deposition. White scale bars indicate 1 μm.

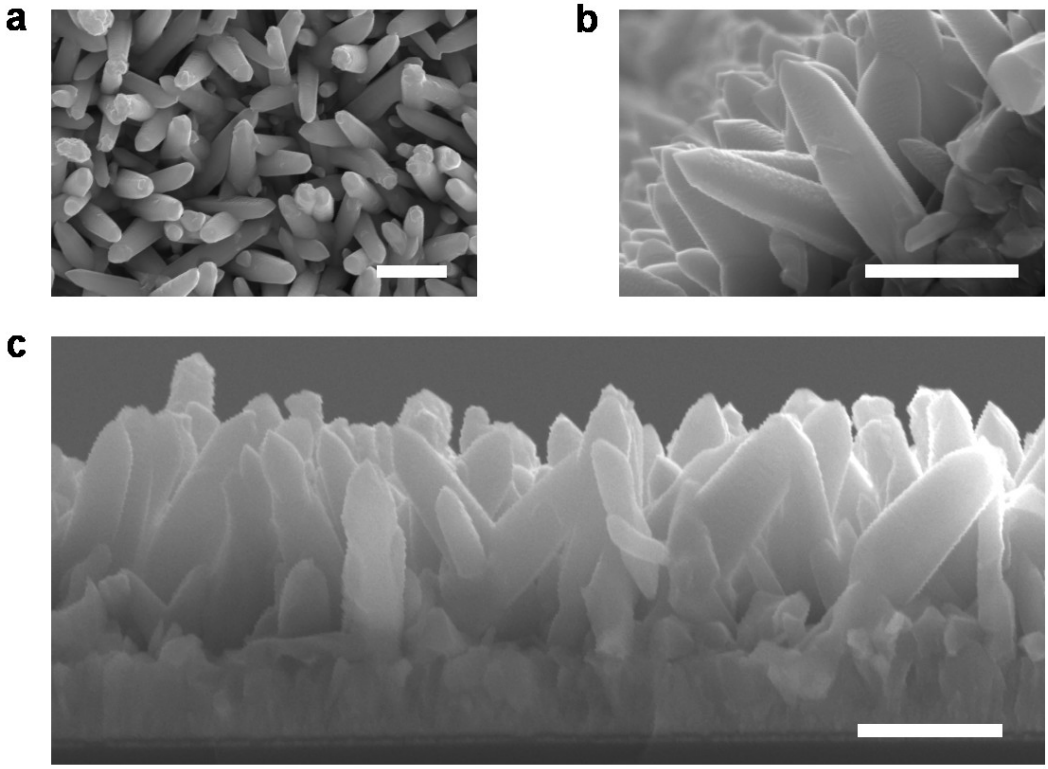

Figure 4-8 Morphology of pulsed laser deposited material at substrate temperature of 300 ºC. Top-down (a), tilted (b), and cross-sectional (c) SEM images of ZnO nanorod arrays after pulsed laser deposition. White scale bars indicate 1 μm.

4.6.2 Experimental details

4.6.2.1 *Fabrication*

Al-doped ZnO nanorod arrays were fabricated by electrochemical deposition in a three-electrode cell employing a Pt wire counter electrode, silver/silver chloride (Ag/AgCl) reference electrode (Pine Instruments; in 4 M KCl; separated from the electrolyte by a porous frit), and FTO (Pilkington; TEC7) working electrode contacted to a Cu wire with conductive Ag paste. Before deposition, FTO/glass substrates were sequentially sonicated in acetone, ethanol, and water for 15 minutes each. Deposition occurred for 0.5-1hr at 90 °C and at -0.9 V vs. Ag/AgCl in an aqueous (18.1 MΩ-cm water) electrolyte containing 1-6 mM zinc nitrate hexahydrate ($Zn(NO_3)\cdot 6H_2O$; 98%; Aldrich) and methenamine ($C_6H_{12}N_4$; Mallinckrodt Chemicals) as described by Vayssieres,[1] and 1-5 μM aluminum chloride ($AlCl_3$; 99.999%; Aldrich).

The arrays were modified by species generated from the pulsed laser ablation of pressed polycrystalline targets in O_2 and N_2 ambients. ZnO and NiO targets were selectively ablated in the presence of oxygen (or mixture of oxygen and nitrogen for ZnO:N deposition) and species from the resulting plasma were deposited onto the ZnO:Al/FTO samples as prepared by electrochemical deposition. The pressure during deposition was 3-5 mtorr as measured by a pirani pressure gauge mounted on the chamber. The samples presented in the main text were

maintained at 200 °C, using a resistive heater and a thermocouple probe embedded in the substrate holder. The laser fluence at the target surface (pulse energy, spot size) and target-substrate distance were selected such that a uniform film could be deposited over several square centimeters.

4.6.2.2 *Physical characterization*

Scanning electron microscopy (SEM) images were obtained with a Hitachi environmental field emission scanning electron microscope (Model S-4300SE/N) operating in secondary electron detection mode.

Spectral transmittance and diffuse reflectance measurements were taken on the ZnO/FTO/glass samples with a Perkin Elmer Lambda Spectrophotometer fitted with an integrating sphere at a wavelength interval of 2 nm. The sample was irradiated at the front surface. The spectral absorptance was obtained by solution of the equation $A_\lambda = 100 - R_\lambda - T_\lambda$, and no correction was made for the substrate.

x-ray diffraction (XRD) measurements were performed on a Siemens D5000 diffractometer with Cu Kα radiation.

4.6.2.3 *Photoelectrochemical characterization*

All electrolytes were prepared with 18.1 MΩ-cm water. The electrolyte for all PEC measurements was prepared as 0.5 M sodium sulfate (Na_2SO_4; > 99 % ACS grade; Sigma Aldrich); pH ≈ 6.8.

Photoelectrochemical measurements were acquired in an open pyrex cell fitted with a quartz window. A 1 cm^2 masked-off, sealed area of the sample was irradiated with a 300 W Xe lamp solar simulator with adjustable power settings through an AM 1.5*G* filter (Oriel; 81092). The light intensity at the sample location in the photoelectrochemical cell was 100 mW cm^{-2} as measured by a power detector (Newport; 70284). No correction was made for the optical absorption of the ~ 4 cm of electrolyte between the quartz window and sample location. A potentiostat (Pine Instruments Bipotentiostat) was used to measure electrochemical data in a 3-electrode setup using a Ag/AgCl reference electrode (Pine Instruments) and a coiled Pt wire counter electrode. The reversible hydrogen electrode (RHE) potential was calculated as $E_{RHE} = E_{Ag/AgCl} + 0.1976 + 0.057 \cdot pH$. N_2 gas was continuously bubbled in solution and directly over the Pt counter electrode before and during the experiment to remove any dissolved O_2 and therefore suppress the reduction of O_2 at the counter electrode. For current-potential measurements, the potential scan was anodic (in the positive direction) and at a rate of 5 mV s^{-1}, with the light mechanically chopped at 0.2 Hz. For the UV filters employed, the transmission of light below the cut-off is below ~1%; ~10% of intensity is absorbed for wavelengths above the cut-offs.

For *IPCE* measurements, +1 V was applied versus a Pt foil located 1 cm from the irradiated portion of the sample. No correction was made for ohmic losses in the electrolyte. N_2 was bubbled in solution before measurements but experimental constraints did not permit bubbling during measurement. *IPCE* measurements were obtained on a quantum efficiency measurement

system employing a Xe lamp, monochromator (5 nm FWHM, 10 nm interval), and light chopper (5 Hz), with a portion of the beam diverted to a photodiode. Data points represent averages of 6 measurements of 5 second sampling periods per wavelength. The system was calibrated before measurement using a NIST-calibrated Si photodiode.

4.6.3 Ellipsometry-reflectometry

The optical functions of the ZnO:Ni discussed in the main text were approximated by a combined ellipsometry-reflectometry technique performed with a commercial thin film metrology system (Scientific Computing International; FilmTek Par 3000 SE). During deposition of ZnO:Ni a small (001) Si substrate was mounted approximately 1 cm from the area later probed by photoelectrochemical (PEC) measurements. The ellipsometric parameters psi and delta were measured on this sample at 70º incidence and over the wavelength range 350-1050 nm at 0.25 nm intervals. The specular reflection spectrum was recorded at 0º (normal) incidence over the range 280 nm to 1050 nm at 0.25 nm intervals. The measured quantities are indicated in Figure 4-9a, as labeled in the figure legend.

The Tauc-Lorentz relation formulated by Jellison and coworkers[2] was used over the entire wavelength range to model the optical functions of the ZnO/Si structure. This dispersion relation forces the extinction coefficient $k(E)$ to be zero at photon energies less than the optical gap and permits a reduction in $k(E)$ as $E \rightarrow \infty$. However, the parameterization only describes interband transitions and cannot resolve Urbach tails or isolated defect transitions associated with impurity levels.[2] Strictly speaking the dielectric function of ZnO has differing extraordinary and ordinary components. As a first approximation, this analysis assumes the optical properties are isotropic and produces *effective* optical functions. This technique has been previously applied to similar material systems.[3]

The Bruggeman EMA relation[4] was used to model the surface region with mixed dielectric functions. A surface roughness layer was modeled as a 50 % - 50 % mixture of the ZnO layer and void space (air). The native oxide layer on the Si substrate was modeled using the Cauchy relations[5] with literature values included in the software package. The structure used for simulation with labeled thicknesses determined by the regression analysis is summarized in Figure 4-9b. A scanning electron microscopy (SEM) image of the ZnO/Si structure's cross section is provided in Figure 4-9c, which is consistent with the proposed model.

The simultaneous fitting of polarization-dependent reflections at two angles is expected to provide a high degree of accuracy for determination of thicknesses and complex refractive indices of multi-layer structures, and the combined technique assists in avoidance of multiple solutions. The measurement simultaneously probes intensity (reflectometry) and polarization changes (ellipsometry) in reflected light.

The simulated quantities based on this analysis are indicated in Figure 4-9a. The analysis resulted in a close correlation among experimental and simulated values, yielding a correlation coefficient of $R^2 = 0.9996$. Attempts to add additional physical accuracy through the introduction of additional oscillators and inter-mixing among layers resulted in unacceptable standard errors

associated with their fitting. The parameterizations are presented below in equations 4-7 though 4-12 and Table 4-1and Table 4-2.

(a)

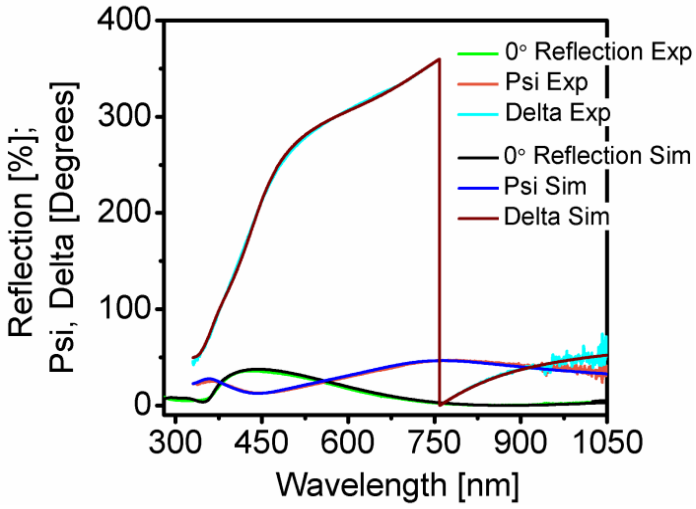

(b)

50% ZnO – 50% Void	**19.27 ± 0.30 nm**
ZnO	**105.75 ± 0.47 nm**
SiO_2	**1.23 ± 0.36 nm**
Si	

(c)

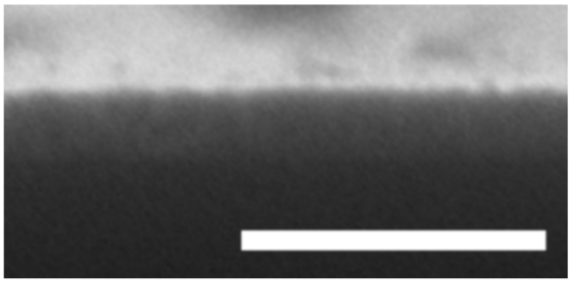

Figure 4-9 (a) Experimental (Exp) and simulated (Sim) values for reflection measured at normal incidence and ellipsometric parameters psi and delta measured at 70° incidence. (b) Multi-layer structure employed for simulation of ellipsometry-reflectrometry data, with thickness and composition quantities determined by the regression analysis. (c) Cross-section SEM image of the ZnO/Si structure. White scale bar indicates 500 nm.

4.6.3.1 *SiO_2 layer; Cauchy*

$$n_\lambda = A_n + \frac{B_n}{\lambda^2} + \frac{C_n}{\lambda^4} \qquad (4-7)$$

$$k_\lambda = A_k + \frac{B_k}{\lambda^2} + \frac{C_k}{\lambda^4} \qquad (4-8)$$

Table 4-1 Values for Cauchy relations used for simulation of SiO_2.

Cauchy	
Parameter	**Value**
A_n	1.447849
B_n	3.41 x 10^{-3}
C_n	2.05 x 10^{-5}
A_k	2.86 x 10^{-19}
B_k	1.23 x 10^{-19}
C_k	6.56 x 10^{-21}

$$\varepsilon_2(E) = \sum_j^m \frac{A_j^2 (E_{center})_j \upsilon (E - E_g)^2}{\left[E^2 - (E_{center})_j^2\right]^2} \cdot \frac{1}{E} \qquad E > E_g \qquad (4-9)$$

$$\varepsilon_2(E) = 0 \qquad E \le E_g \qquad (4-10)$$

$$\varepsilon_1(E) = \varepsilon_\infty + \frac{2}{\pi} P \int_{E_g}^{\infty} \frac{\xi \varepsilon_2(\xi)}{\xi^2 - E^2} d\xi \qquad (4-11)$$

Table 4-2 Fitted values for Tauc-Lorentz parameterization and associated standard errors.

Tauc-Lorentz		
Parameter	**Value**	**Standard**
ε_∞	3.320	0.009
E_g	1.393	0.061
A	1.818	0.054
E_{center}	3.83	0.011
υ	0.627	0.012

4.6.3.2 *Surface layer; Bruggeman EMA*

$$\sum_{i=1}^{m} f_i \frac{\varepsilon_i - \varepsilon_{eff}}{\varepsilon_i + 2\varepsilon_{eff}} = 0$$

$$\sum_{i=1}^{m} f_i = 1 \qquad f_1 = 0.5, \quad f_2 = 0.5 \qquad (4-12)$$

Where f_1 is the fraction of ZnO, f_2 is the fraction of void space.

The dielectric function of ZnO:Ni determined by this analysis is presented in Figure 4-10a. The absorption coefficient, calculated from the modeled extinction coefficient, and its reciprocal, which assuming homogeneity is equal to the mean light penetration depth in the film, is plotted in Figure 4-10b.

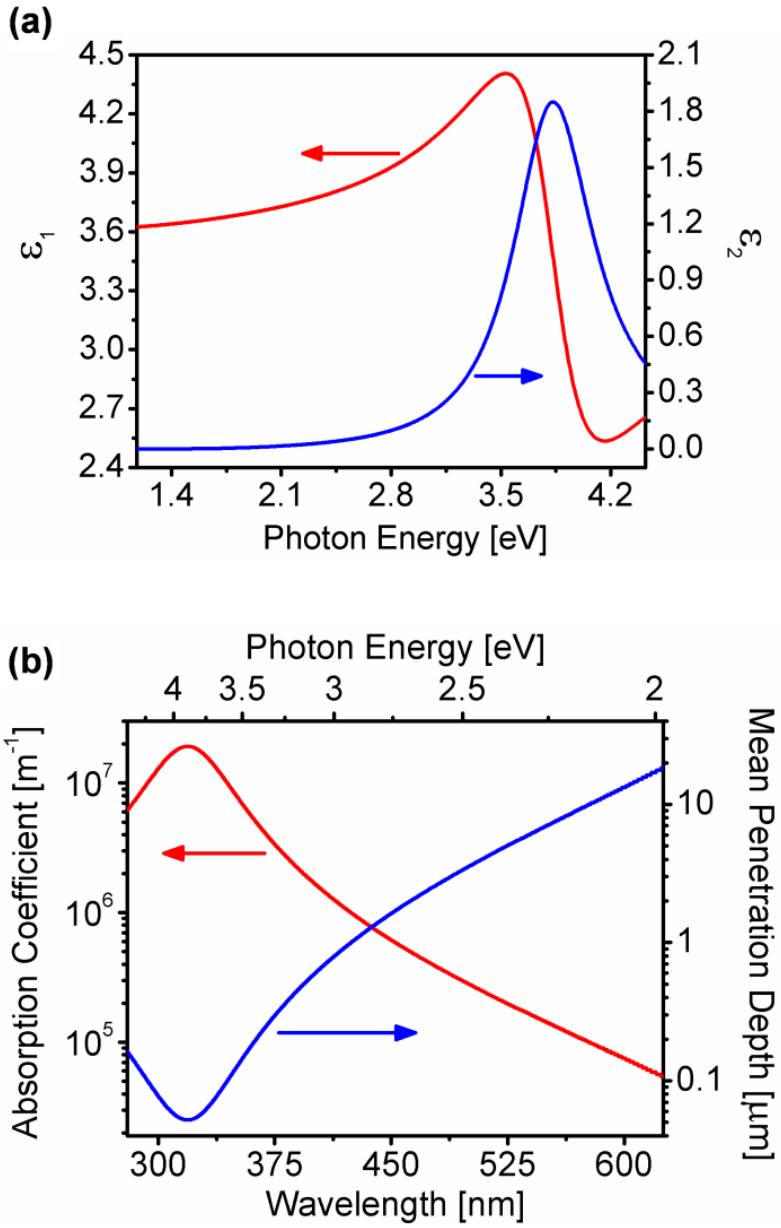

Figure 4-10 Complex dielectric function, $\varepsilon_1 + i\varepsilon_2$, as determined by ellipsometry-reflectometry regression analysis. (b) Spectral absorption coefficient and its reciprocal, the mean light penetration depth, for a ZnO:Ni thin film.

4.6.4 Complete IPCE spectra for ZnO:Al-ZnO:Ni system

The complete *IPCE* spectra for the ZnO:Al and ZnO:Al-ZnO:Ni system described in the main text is provided in Figure 4-11.

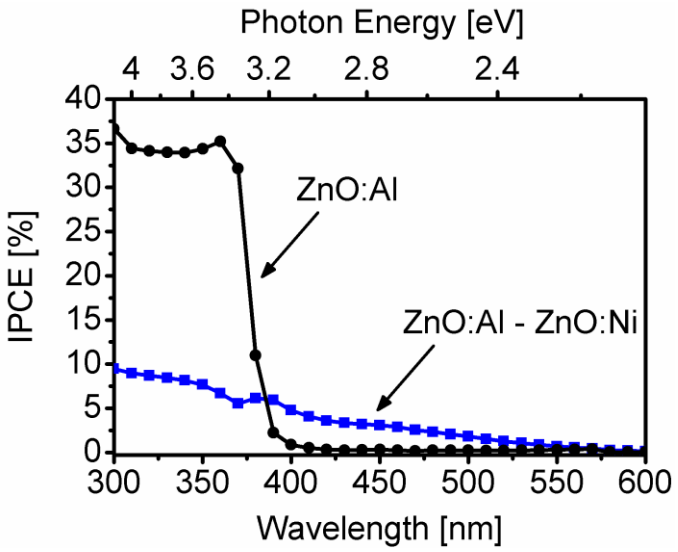

Figure 4-11 Complete spectra for incident photon conversion efficiencies for front-side irradiation of ZnO:Al – ZnO:Ni photoelectrodes, as described in the main text, in 0.5 M Na_2SO_4 with +1 V applied versus a Pt counter electrode.

4.6.5 Amperometric (current-time) measurement with color filters for ZnO:Al

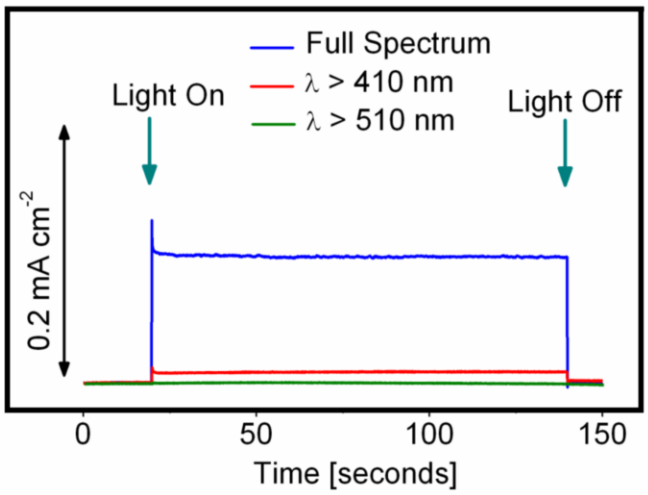

Figure 4-12 Amperometric current-time measurement for ZnO:Al with chopped AM 1.5*G*-filtered 100 mW cm^{-2} irradiation at 0.6 V vs Ag/AgCl, with application of color filters.

A color-filtered amperometric (current-time) measurement was performed on ZnO:Al without modification with Ni (Figure 4-12). As expected, the photocurrent is primarily driven by UV excitation, which is only present under full spectrum irradiation. Application of color filters reduces total photoactivity significantly, consistent with *IPCE* results.

4.6.6 Proof of concept for ZnO:Al-ZnO:N system

Several ZnO nanostructure configurations were examined in an attempt to optimize performance. In addition to that presented in the main text of Chapter 5 above, one promising configuration involves selectively doping the outer region of ZnO nanostructures with nitrogen.

Nitrogen and other anions (eg S, C) have emerged as important dopants for photoelectrochemical and photocatalytic applications utilizating wide band gap metal oxides.[6,7,8] It has recently been reported that nitrogen doping significantly enhances the conversion efficiency of ZnO nanowire array photoelectrodes in PEC cells.[9] Remarkably, in this case the quantum efficiency at UV wavelengths was improved by nitridization of ZnO.

The analysis of ZnO:Al - ZnO:N that follows corresponds to the SEM images presented in Figure 4-8. An x-ray diffraction pattern (Figure 4-13a) indicates hexagonal ZnO and tetragonal SnO_2, and small unlabeled peaks attributed to a contaminant during fabrication or characterization, which were also observed for other dopants examined (see main text). The nanostructures show less significant (002) alignment, which results from the lack of pre-deposition of ZnO nanocrystal seeds in this case. Figure 4-13b provides the spectral absorptance of ZnO nanostructure arrays before and after modification with ZnO:N at 300 °C. The broad absorption features beyond the band edge of ZnO result in a change in sample color from transparent-white to brown (Figure 4-13c). The visible-light absorption of ZnO:N is relatively featureless, which is consistent with previous observations of a distribution of N-related energy states above the bandgap, resulting in a broad absorption tail.[7]

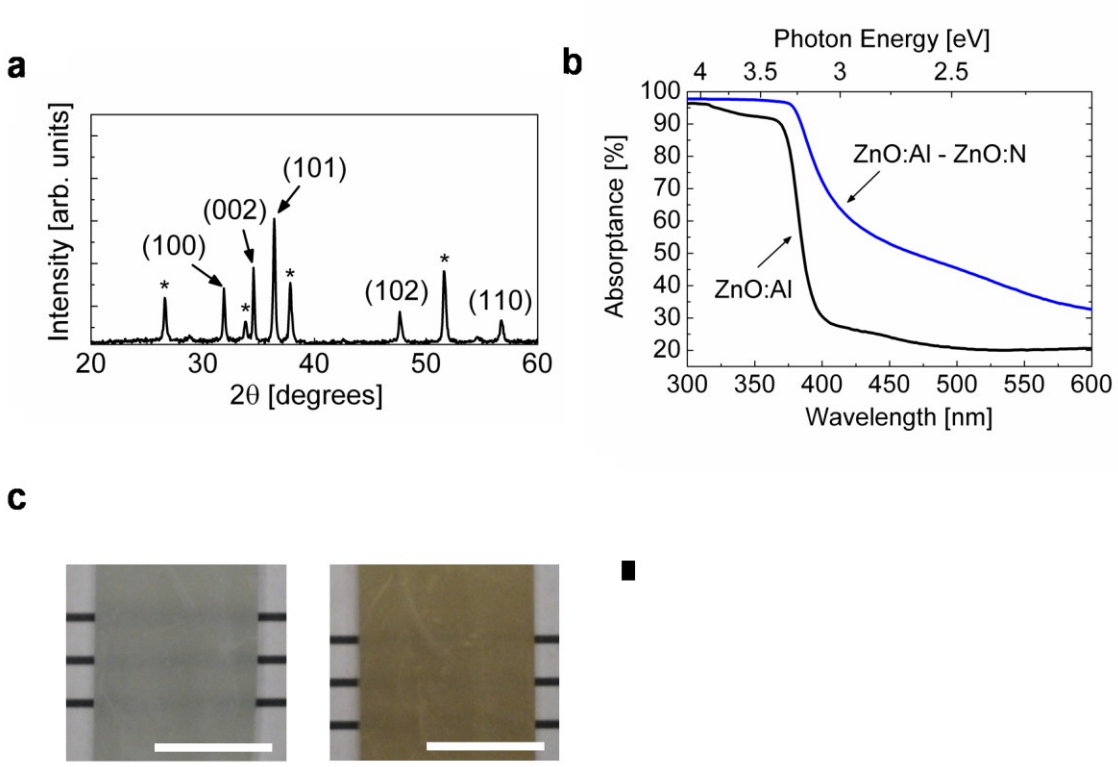

Figure 4-13(a) x-ray diffraction pattern of final ZnO nanostructure array. Hexagonal ZnO (wurtzite) is indexed; tetragonal SnO_2 (cassiterite) substrate peaks indicated by *. (b) Absorptance spectra ($A_\lambda = 100 - T_\lambda - R_\lambda$) of ZnO/FTO/glass structures before and after modification with ZnO:N, (c) Photographs of samples before and after modification. White scale bars indicate 1 cm.

Incident photon conversion efficiency (IPCE) spectra for electrodes with N doping are presented in Figure 4-14. There is a marked decrease in UV activity, as is expected considering all photoholes originating from UV excitation must pass through the defect ZnO:N crystallites. The visible-light enhancement is indicated in Figure 4-14b. Although the IPCE values at visible wavelengths approach the resolution limit of the measurement instrument, the visible light enhancement result was repeatable. This suggests the successful charge transfer of photoelectrons originating from N-induced states through the homojunction structure. The reason for the low conversion efficiency that results from N doping is unclear at present. It is expected that optimization of this structure, as described in the main text, will contribute to development of promising visible-light-active homojunction nanostructure arrays for this application.

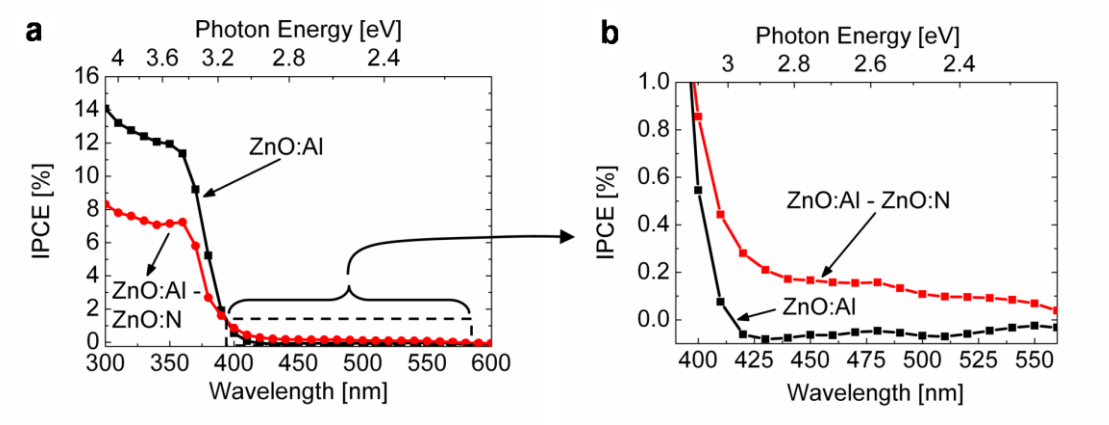

Figure 4-14 Incident photon conversion efficiency for front-side irradiation of ZnO:Al – ZnO:N photoelectrodes in 0.5 M Na_2SO_4, with +1 V applied versus a Pt counter electrode: (a) complete spectra and (b) resolved spectra indicating visible light conversion efficiency enhancement.

4.6.7 References for Chapter 4 Appendix

1. L. Vayssieres, *Adv. Mater.* **15**, 464 (2003).
2. G. E. Jellison and F. A. Modine, *Appl. Phys. Lett.* **69**, 371 (1996).
3. A. Mendoza-Galván, C. Trejo-Cruz, J. Lee, D. Bhattacharyya, J. Metson, P. J. Evans, and U. Pal, *J. Appl. Phys.* **99,** 014306 (2006).
4. D. A. G. Bruggeman, *Ann. Phys. (Leipzig)* **24**, 636 (1935).
5. H. Fujiwara, in: Spectroscopic Ellipsometry: Principles and Applications, (Wiley, West Sussex, UK, 2007)
6. R. Asahi, T. Morikawa, T. Ohwaki, K. Aoki, and Y. Taga. *Science* **293**, 269-271 (2001).
7. T. Lindgren, J. M. Mwabora, E. Avendaño, J. Jonsson, A. Hoel, C.-G. Granqvist, and S.-E. Lindquist, *J. Phys. Chem. B* **107**, 5709 (2003).
8. K.-S. Ahn, Y. Yan, S.-H. Lee, T. Deutsch, J. Turner, C. E. Tracy, C. L. Perkins, and M. Al-Jassim, *J. Electrochem. Soc.* **154**, B956 (2007).
9. X. Yang, A. Wolcott, G. Wang, A. Sobo, R.C. Fitzmorris, F. Qian, J. Z. Zhang, and Y. Li, *Nano Lett.* **9**, 2331 (2009).

5 Electron enrichment in 3*d* transition metal oxide hetero-nanostructures

Chapter 5 is an adaptation of a published article:

C.X. Kronawitter, J.R. Bakke, D.A. Wheeler, W.-C. Wang, C. Chang, B.R. Antoun, J.Z. Zhang, J.-H. Guo, S.F. Bent, S.S. Mao, and L. Vayssieres, Electron enrichment in 3d transition metal oxide hetero-nanostructures, *Nano Lett*., **11**, 3855 (2011).

The majority of the work in this chapter was supported by Sandia National Laboratories. Sandia National Laboratories is a multi-program laboratory managed and operated by Sandia Corporation, a wholly owned subsidiary of Lockheed Martin Corporation, for the U.S. Department of Energy's National Nuclear Security Administration under contract DE-AC04-94AL85000.

5.1 Abstract for Chapter 5

The previous chapters investigated photoelectrode designs based on oxide materials whose properties meet many of the requirements for efficient water photo-oxidation. Some of the most important features of these designs, especially those discussed in Chapters 3 and 4, involve the interfacial regions of dissimilar oxides. The separation of photo-excited carriers is driven by gradients of electrochemical potential, which can emerge at junctions of electronically and chemically distinct materials. These final chapters investigate photoelectrodes from the perspective of their electronic structure. These analyses were made possible by soft x-ray spectroscopy measurements conducted at the Advanced Light Source. The analysis of electronic structure measurements is intended to contribute to a more fundamental understanding of oxide photoelectrodes.

Direct experimental observation of spontaneous electron enrichment of metal *d* orbitals in a new transition metal oxide heterostructure with nanoscale dimensionality is reported. Aqueous chemical synthesis and vapor phase deposition are combined to fabricate oriented arrays of high-interfacial-area hetero-nanostructures comprised of titanium oxide and iron oxide nanomaterials. Synchrotron-based soft x-ray spectroscopy techniques with high spectral resolution are utilized to directly probe the titanium and oxygen orbital character of the interfacial region's occupied and unoccupied densities of states. These data demonstrate the interface to possess electrons in Ti 3*d* bands and an emergent degree of orbital hybridization that is absent in parent oxide reference crystals. The carrier dynamics of the hetero-nanostructures are studied by ultrafast transient absorption spectroscopy, which reveals the presence of a dense manifold of states, the relaxations from which exhibit multiple exponential decays whose magnitudes depend on their energetic positions within the electronic structure.

This work involved collaboration with researchers at Stanford University, University of California at Santa Cruz, the Advanced Light Source, and National Institute for Materials Science. Specifically it involved collaboration with Jonathan Bakke and Stacey Bent at Stanford University, Damon Wheeler and Jin Zhang at UC Santa Cruz, Wei-Cheng Wang and Jinghua Guo at the Advanced Light Source, and Lionel Vayssieres at the International Center for Materials NanoArchitectonics, National Institute for Materials Science, Tsukuba, Japan.

5.2 Introduction to Chapter 5

The interfaces of oxide heterostructures provide a rich and diverse platform for the discovery and study of unique emergent electronic phenomena, which enables development of new multifunctional materials for several proposed oxide-based electronic device technologies.[1] Oxide interface engineering represents a new materials fabrication strategy, which, given a greater degree of fundamental understanding, could permit the manipulation of the energetic and behavioral specificity of electrons.[2,3] Here we report the direct experimental observation of electron enrichment of 3*d* orbitals in the interface of a new transition metal oxide heterostructure system based on junctions of titanium oxide and hematite nanomaterials. Further examination of the interface orbital character reveals evidence of an emergent degree of *p-d* hybridization that is absent from reference parent crystals. These findings and their consequences represent a convergence of nanoscience and oxide interface engineering, two highly influential and technologically promising fields within materials science and chemistry.

Concurrent to the exciting advances[1] in oxide interface engineering, the recent applications of nanoscience to electronic device components, most notably those for solar energy conversion devices, have led to the utilization of a number of physical properties and phenomena that will potentially reduce system fabrication costs and increase overall conversion efficiencies.[4,5,6] These practices, which are emblematic of third generation solar cells, include the engineering of quantum confinement effects,[4] plasmonic resonance modes,[7] intermediate bands,[8] high specific surface areas,[9] and overall optimization of device architectures in relation to operational processes including light absorption and carrier transport.[10] The benefits of hetero-nanostructures, or those structures which contain junctions of dissimilar nanomaterials, can similarly be utilized for a broad range of applications for emerging optoelectronic devices. This includes the suppression of detrimental interfacial back-reactions[11] and the separation of photogenerated charges[12] in photovoltaic devices as well as more advanced applications such as the direct manipulation of light-matter-spin interactions for quantum information processing.[13]

In the context provided by these emerging fields, oxide nanostructures, and indeed oxide hetero-nanostructures, show unique potential to address the strict optical and electronic material properties required by the photoactive components of solar energy conversion devices. Photoelectrochemical (PEC) solar technologies in particular stand to benefit from the engineering of oxide hetero-nanostructures, as their enabling photoelectrodes often require great chemical stability as well as a high degree of specialization with respect to optical absorption, charge transfer, and chemical reactivity.[5] The large oxidative potential resulting from the high ionization energies of most metal oxides is most importantly applied for the photoelectrochemical oxidation of water, a critical step in the sustainable and clean generation of solar fuels such as hydrogen.[5, 14] Here we demonstrate that oxide hetero-nanostructure

engineering presents an opportunity to fabricate entirely new materials that possess emergent or unexpected surface and interfacial properties.

5.3 Description of hetero-nanostructure array

The oxide hetero-nanostructure arrays presently investigated were fabricated through a combination of aqueous chemical synthesis[15] and atomic layer deposition[16,17] (see Experimental Methods for details). Briefly, beta-phase iron(III) oxyhydroxide (β-FeOOH, akaganeite) rod structures were grown directly from an aqueous precursor salt solution by hydrolysis-condensation and heteronucleation onto fluorinated tin(IV) oxide-coated glass (SnO_2:F, FTO) substrates, as described in reference 18. Annealing (above 450ºC) of the vertically aligned β-FeOOH rod arrays resulted in a phase transformation to alpha-phase iron(III) oxide (α-Fe_2O_3, hematite).[18] The α-Fe_2O_3 is organized into bundles of 3-5 nm single crystalline rods whose electrons are quantum-confined in the lateral dimension.[19] Following this, nanocrystalline Ti_xO_y was deposited directly at the α-Fe_2O_3 surface at 150 ºC by atomic layer deposition (ALD), a monolayer-by-monolayer growth technique.[16] The resulting structures, which are notated herein as Ti_xO_y-Fe_2O_3, were investigated by synchrotron-based soft x-ray spectroscopy techniques as well as by ultrafast transient absorption spectroscopy. These advanced characterization techniques, which probe the material at atomic length scales and ultrafast time scales, provide a description of the system's band structure and its densities of localized surface and interface states.

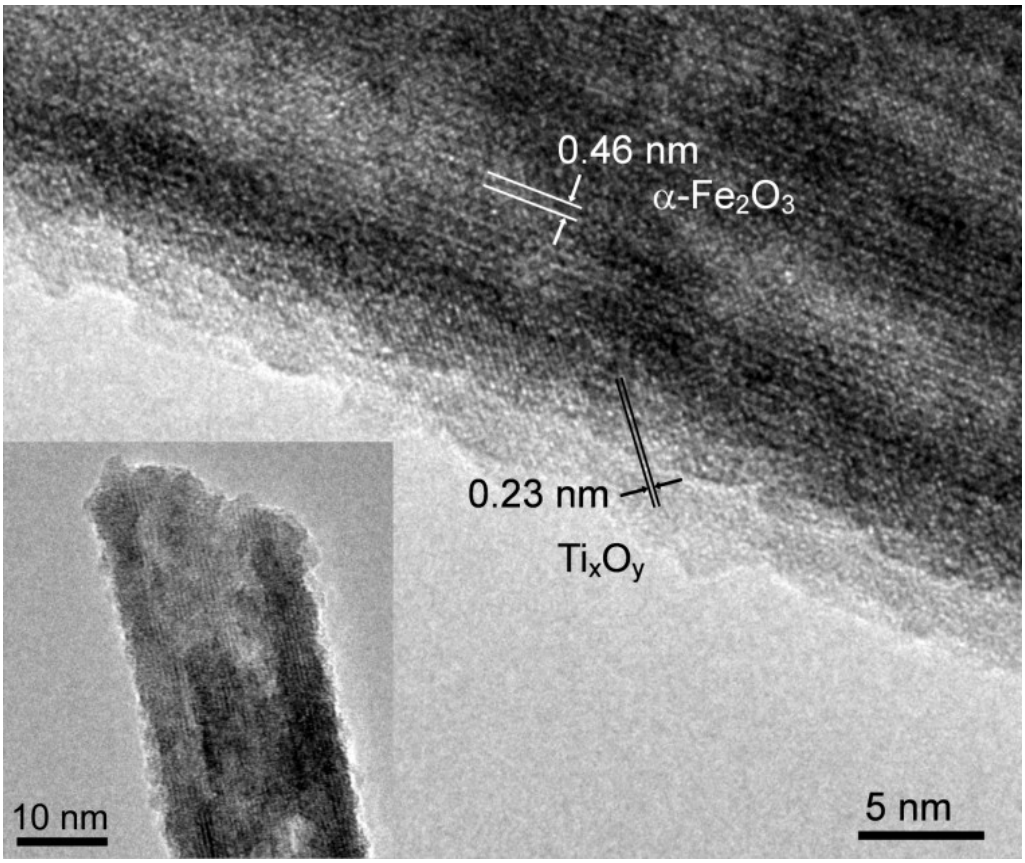

Figure 5-1 Transmission electron microscopy image of the Ti_xO_y-Fe_2O_3 hetero-nanostructure interface, with lattice fringes evident. Inset provides a lower resolution image of the tip of a complete structure.

.

Transmission electron microscopy (TEM) images of representative structures are presented in Figure 5-1. The complete structure displayed in the inset terminates with an uneven surface, which is indicative of bundles of ca. 5 nm diameter rods, as reported previously.[15,18] The Ti_xO_y structures are visible with lighter contrast on the surface and are distributed conformally along the length of the rod. Heterostructures comprised of α-Fe_2O_3 and stoichiometric TiO_2 have previously been fabricated, mainly for photoelectrochemical[20] and photocatalytic[21] applications. TiO_2 nanotubes containing α-Fe_2O_3 crystals, which share a common configuration with the present structures, albeit on longer length scales, have been fabricated with similar applications in mind.[22]

By probing with high spectral resolution the unoccupied and occupied densities of states, synchrotron-based x-ray spectroscopy techniques enable detailed analyses of the orbital characteristics of nanomaterials.[23] Of particular interest to the present study is the system's interfacial electronic structure: that is, the character and occupancy of *d* orbitals at the interface.

For this reason results for total electron yield mode, which has a probe depth of ca. 5 nm^2 and therefore for this structure directly measures the interface, are considered.

5.4 Ti L-edge x-ray absorption

The unoccupied electronic structure of Ti_xO_y-Fe_2O_3 hetero-nanostructures was examined by x-ray absorption spectroscopy (XAS), a technique capable of monitoring a number of important characteristics of the system density of states. For instance, cation charge transfer phenomena across the interface, which can be monitored by XAS,[24] will change the overall occupancy of the hetero-nanostructures' metal 3*d* states, which is expected to have significant consequences on the carrier dynamics and thus on the overall performances of optoelectronic devices utilizing transitions to and from such states.

The titanium $L_{II,III}$-edge absorption spectrum for Ti_xO_y-Fe_2O_3 is presented in Figure 5-2a. Also included in Figure 5-2a are L-edge absorption spectra measured for three reference titania crystals: anatase TiO_2 ($3d^0$ electronic configuration), Tistarite (corundum) Ti_2O_3 ($3d^1$), and rock salt TiO ($3d^2$). Both the relative spectral intensities and line shapes of these signals contain information relating to the coordination of Ti in the thin surface and interfacial region. The Ti L-edge absorption spectra of titanium oxides have been comprehensively documented.[25,26,27,28] The two sets of local maxima over this energy range can be assigned to excitations of Ti $2p_{3/2}$ (peaks *A* and *B*) and Ti $2p_{1/2}$ (peaks *C* and *D*) core levels into empty Ti 3*d* states.[23] These sets of peaks result from the core-hole spin-orbit splitting of the 2*p* levels.[27] The ligand field splits the final states into two levels possessing t_{2g} and e_g symmetry;[25] the energy difference between these sublevels is related, but not equal, to the field splitting energy.[29]

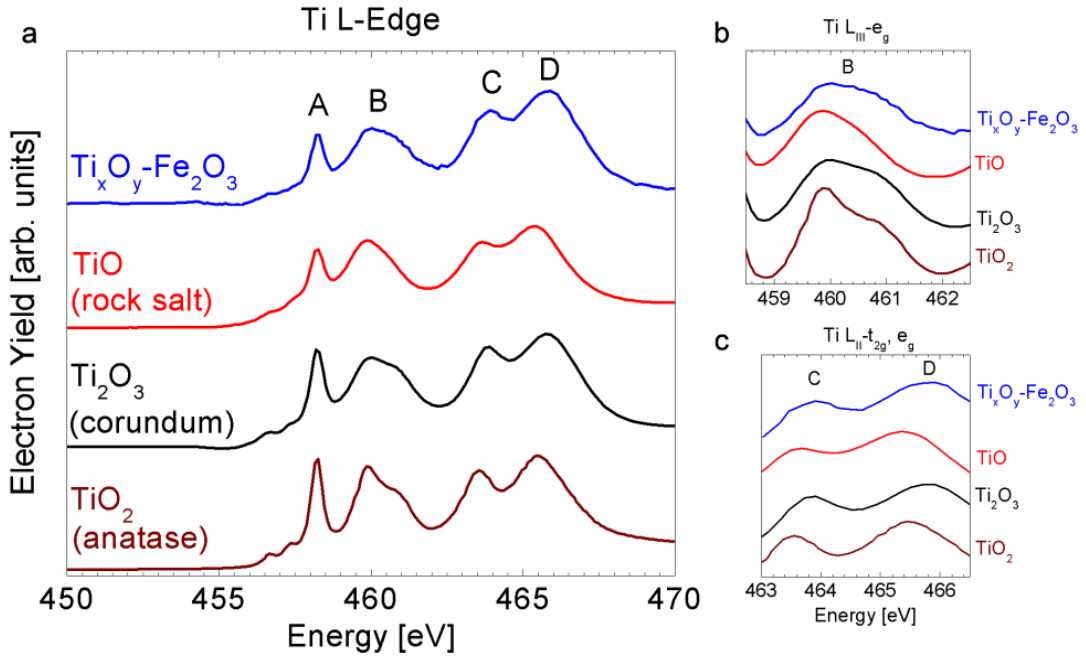

Figure 5-2Ti $L_{II,III}$-edge x-ray absorption spectra for Ti_xO_y-Fe_2O_3 and reference TiO (red), Ti_2O_3 (black), and TiO_2 (brown): (a) entire spectral range, (b) resolved spectral range for comparison of L_{III}-e_g peak centered near 460.5 eV (*B*), and (c) resolved spectral range for comparison of L_{II}-t_{2g} and e_g peaks (*C* and *D*). All curves are normalized to their respective intensities at peak *D*$L_{II,III}$-edge x-ray absorption spectra for Ti_xO_y-Fe_2O_3 and reference TiO (red), Ti_2O_3 (black), and TiO_2 (brown): (a) entire spectral range, (b) resolved spectral range for comparison of L_{III}-e_g peak centered near 460.5 eV (*B*), and (c) resolved spectral range for comparison of L_{II}-t_{2g} and e_g peaks (*C* and *D*). All curves are normalized to their respective intensities at peak *D*

.

First, it is to be noted that the broadening of peak *A* in Figure 5-2a, as well as the slight shoulder appearing at the low energy side of this edge, has previously been associated with a reduction in the oxidation state of the cation, and is indeed observed after the controlled reduction of Ti^{4+} surface species on TiO_2 single crystals.[30] The slight broadening of peak *A* and the red-shift of the L-edge absorption onset with respect to that for TiO_2 provides initial evidence of a Ti oxidation state lower than 4+ in Ti_xO_y-Fe_2O_3.

In order to understand the nature of the Ti_xO_y structure, it is helpful to consider the characteristics of the L_{III}-e_g peak (peak *B*), centered near 460.5 eV (Figure 5-2b). The line shape of the L_{III}-e_g peak is extremely sensitive to the local symmetry of the metal cations,[23] and therefore provides a signature of the bonding environment in the titania layer. In titania reference minerals the line shapes and intensities of the L_{III}-e_g peaks show diversity with respect to the cations' site environments.[26,31] Generally there are peaks observed between 459 eV and 462 eV, the origins of which have been considered through several theoretical frameworks.[31] In anatase TiO_2, the low-energy side of the peak dominates over the high-energy side, whereas in rutile TiO_2 the relative intensities are reversed.[25] Experimentally it is commonly determined that the

resolution of these peaks decreases with decreasing oxidation state. These trends are certainly confirmed in the present analysis, which show expected L_{III}-e_g line shapes with respect to crystal structure and Ti oxidation state. The doublet is completely absent in rock salt TiO. Interestingly, for the hetero-nanostructures investigated in this work the line shapes and intensity ratios of the L_{III}-e_g peak in Figure 5-2b most resemble those of Ti_2O_3.

The peaks labeled *C* and *D*, which originate from excitations of Ti $2p_{1/2}$ core levels into empty Ti 3*d* states, are resolved in Figure 5-2c. The relative intensities of these peaks as well as their line shapes again most closely resemble those of Ti_2O_3.

This observation of Ti_2O_3-like Ti coordination is reinforced by consideration of the substrate onto which the phase grows, α-Fe_2O_3: trigonal Ti_2O_3 is corundum-type and is therefore isostructural to α-Fe_2O_3. At the thickness considered here, on the order of 1 nm, substrate interactions are expected to play an important role in the evolution of the surface layer. Considering that ALD is a monolayer-by-monolayer growth technique, the Ti_2O_3-like L-edge spectrum is consistent with a crystal growth mechanism (presumably by domain matching epitaxy[32]) at the α-Fe_2O_3 surface.

5.5 O K-edge x-ray absorption

Oxygen K-edge absorption spectra, which probe the projected O *p* unoccupied density of states from core l*s* excitations, are presented for Ti_xO_y-Fe_2O_3 and reference crystals in Figure 5-3a. The O l*s* XAS spectra for all samples can be divided into two feature sets of interest: the local intensity maxima between 528 and 535 eV and those positioned at energies greater than 535 eV. The first set of features describe the oxygen 2*p* weight in the transition metal 3*d* band, and for all reference samples contains two peaks related to the t_{2g} and e_g symmetry bands.[33]

The conspicuous absence of any observable t_{2g}-e_g splitting for Ti_xO_y-Fe_2O_3 requires careful interpretation in light of previous O K-edge XAS studies of transition metal oxide systems.[33,34] The absence most likely indicates an interfacial charge transfer process, which is expected to be unique to the hetero-nanostructure architecture and its interfacial bonding arrangement. Notably, such phenomena change the occupancy of metal *d* states, which is directly reflected in the *p* unoccupied projected density of states in the presence of *p*-*d* hybridization. A completely filled t_{2g} orbital will be unavailable for the K-edge transition and will be absent in the O l*s* XAS spectrum. For example, in NiO (nominally d^8 configuration) the $2t_{2g}$ orbitals are completely occupied, which results in a single sharp feature in this spectral range,[33,34] similar to that observed for Ti_xO_y-Fe_2O_3. This argument is consistent with further analyses of *p*-*d* hybridization effects, as discussed below.

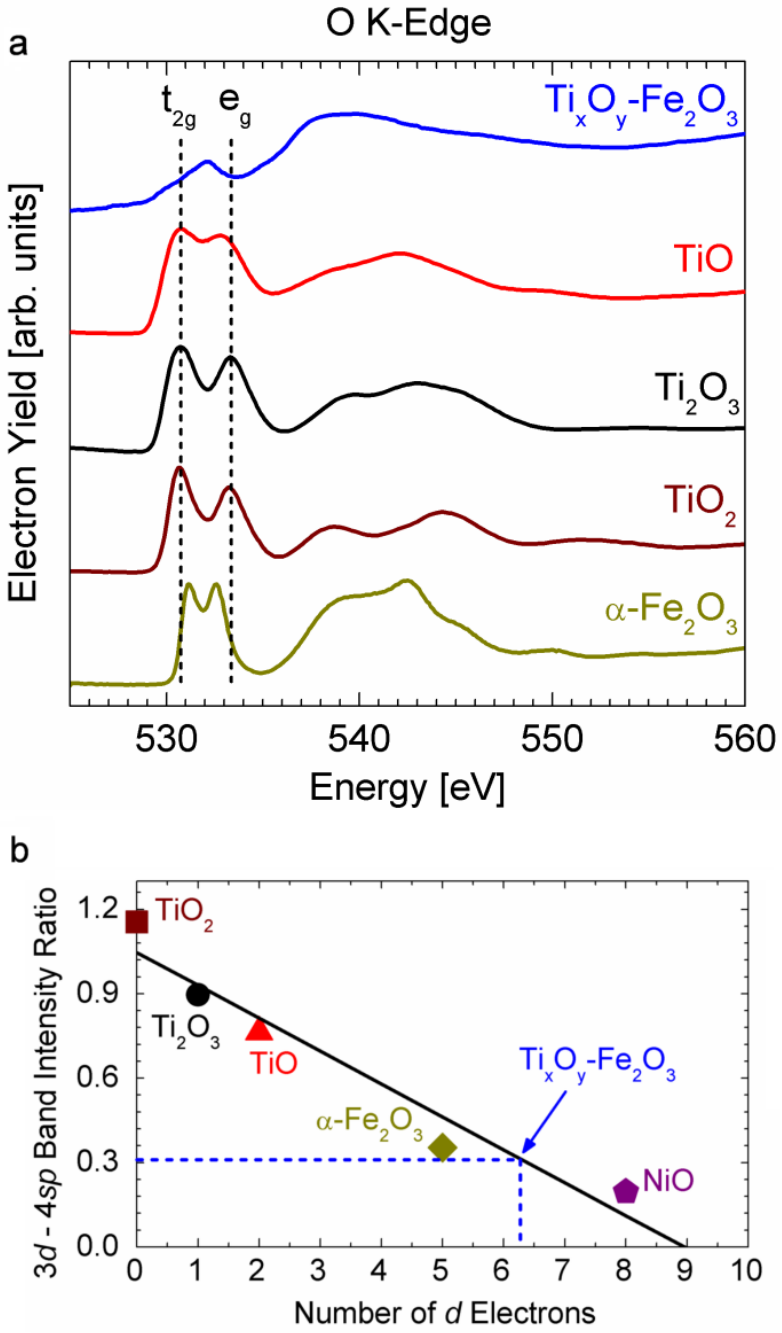

Figure 5-3 O K-edge x-ray absorption spectra for Ti_xO_y-Fe_2O_3 and reference crystals. Dotted lines indicate the positions of t_{2g} and e_g peak maxima for the TiO_2 reference. (b) The ratios of the integrated areas of the 3*d* bands to those of 4*sp* bands, plotted with respect to number of *d* electrons in reference crystals. Solid line indicates linear fit to reference data. At d^{10} the linear interpolation does not terminate at 0 because metal 3*d* orbitals shrink in late transition metal oxides, which diminishes experimentally observed *p*-*d* hybridization effects.[33]

Alternatively, an absence of observable splitting of this peak may relate to size effects and structural distortion present in the hetero-nanostructure. In α-Fe_2O_3 nanoparticles for instance, a similar absence was observed and was attributed to large densities of surface states and the presence of strain anisotropy, which results in a distortion of the oxygen site environment.[35] These features will tend to broaden the spectral signatures of crystal field splitting.

The features at energies greater than 535 eV are attributable to the hybridization of oxygen *p* states with metal 4*s* and 4*p* states.[33] The breadth of the spectral range of these features relates to the covalency of the bonding environment, and the features' line shapes reflect the octahedral symmetry present.[33]

The diversity of intensity ratios observed for the two bands (3*d* and 4*sp* bands) among the materials provides a framework for examining the extent of O *p* hybridization with the metal *d* band in the hetero-nanostructure's interfacial region. The importance of such an analysis lies in the relationship between orbital occupancy and the oxygen *p* character of the transition metal 3*d* band. For example, it is known[33] that the shapes and magnitudes of the 3*d* bands' contribution in oxygen 1*s* XAS spectra are heavily influenced by the presence of a filled e_g orbital in the ground state. This influence divides several defining characteristics of this band between the early- and late-transition-metal oxides.[33] In addition, Reference 33 suggests that a decrease in the relative intensity of the 3*d* band is dominantly caused by a reduction in the number of unoccupied 3*d* states available to mix with O 2*p* states. This suggestion predicts a linear relationship between the bands' intensity ratios and the number of holes. To illustrate this correlation in the present data, the ratios of the integrated areas of the 3*d* bands to those of the 4*sp* bands are plotted with respect to number of 3*d* electrons (Figure 5-3b). An additional ratio for NiO is included to provide a more complete set of electronic configurations. As expected, a linear relationship is observed among all reference samples. Extrapolation of a linear fit to these data indicates the measured intensity ratio in Ti_xO_y-Fe_2O_3 (0.313) corresponds to an intermediate degree of *p*-*d* hybridzation, greater than that found in d^5 oxides such as α-Fe_2O_3, and less than that found in d^8 oxides, such as NiO.[33] These hybridization observations provide additional evidence of the presence of an interfacial charge transfer process within the hetero-nanostructure, which alters the *d* orbital occupancy and which is reflected in the *p* unoccupied projected density of states.

5.6 Ti L-edge x-ray emission

The system's occupied electronic structure was probed by x-ray emission spectroscopy (XES). The presence of partially filled 3*d* bands, as discussed above, will be directly evident in L-edge emission spectra.

The Ti $L_{II,III}$-edge emission spectrum, which for 3*d* transition metals describes the filled portion of the 3*d*4*s* band, is provided in Figure 5-4. This figure also includes emission spectra recorded for the reference crystals discussed above, with their respective *d* electron count indicated. The emission spectrum for stoichiometric TiO_2, which shows a single intense peak, contrasts considerably with the other recorded spectra. This observation indicates a commonality among the occupied electronic structures of Ti_xO_y-Fe_2O_3, TiO, and Ti_2O_3, the latter two of which are known to possess partially filled Ti 3*d* bands. Reference 25, which is a comprehensive discussion of band structures from emission and absorption spectra of several transition metals and their

related compounds, provides an analysis of the $L_{II,III}$ emission spectra for titanium metal as well as six reference oxides of titanium. The peak labeled *A* in Figure 5-4 is attributed to a transition from the oxygen 2*p* band to a vacancy in the titanium L_{III} shell.[25] Peaks *B* and *C*, which are absent in the spectrum for stoichiometric TiO_2, predominantly represent transitions from occupied 3*d* states (Peak *B*: Ti 3*d*→Ti L_{III}; Peak *C*: Ti 3*d*→Ti L_{II}).[25] That these emissions exist in the Ti_xO_y-Fe_2O_3 spectrum provides direct confirmation of the presence of Ti 3*d* electrons in the hetero-nanostructure.

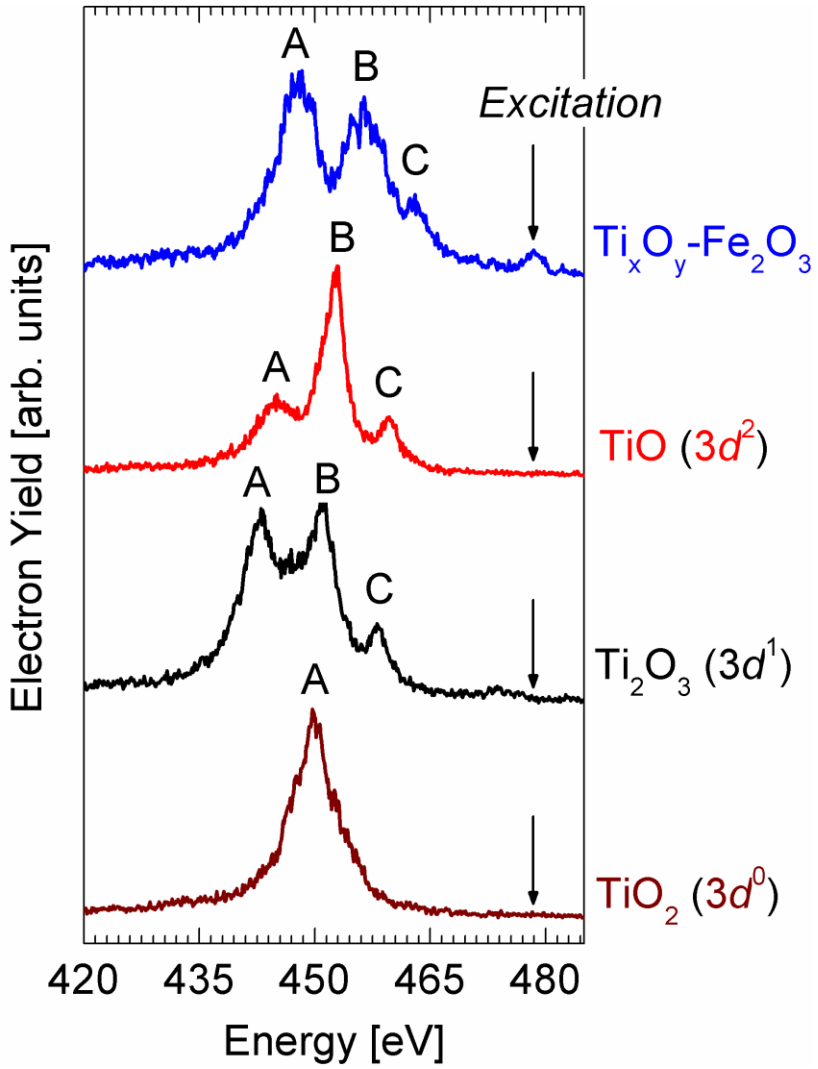

Figure 5-4 Ti $L_{II,III}$-edge x-ray emission spectra for Ti_xO_y-Fe_2O_3 and reference titania crystals with indicated electronic configurations.

.

The ability to engineer ultra-thin, electron-rich titanium oxides at low temperatures is of significant technological interest, considering the known macroscopic optical and electronic

properties of these materials. TiO, Ti_2O_3, the Magneli phases[36] Ti_4O_7 and Ti_5O_9, and novel Ti_3O_5[37], are all electrical conductors, due to their partially filled Ti 3*d* bands.[25] These electrical properties manifest in contrast to those of the oxides of heavier 3*d* metals, such as Fe and Ni, which are insulators at room temperature. In α-Fe_2O_3 for example, the 3*d* band is exceedingly narrow, which results in a high effective mass and low mobility for electrons.[38] In terms of their conduction, electrons in α-Fe_2O_3 3*d* bands are more accurately described as experiencing localized energy levels; in this crystal the 3*d* wave functions do not overlap and remain concentrated near the cation.[39] In the lower oxides of titanium, however, the 3*d* wave functions overlap sufficiently to form a conduction band. Ti_2O_3, whose Ti coordination is most likely mimicked in Ti_xO_y-Fe_2O_3, is of particular interest for solar device technologies: the former is semiconducting at room temperature and its presence enhances visible light activity of titania photocatalysts.[40] It is a conductive oxide[41] and it undergoes a semiconductor-semimetal transition near 120 ºC.[42]

5.7 O 2*p* orbital analysis

The O K-edge emission spectrum of Ti_xO_y-Fe_2O_3 was also studied; these data are plotted directly with absorption data in Figure 5-5. The energy distances between these features are equal to corresponding distances in the actual system density of states.[25] Examination of the first derivatives of these signals (Figure 5-5, bottom) provides a quantitative measure of the energy distance between occupied and unoccupied O 2*p* states in the interfacial region of Ti_xO_y-Fe_2O_3. Because the O 2*p* emission spectra red shifts for lower oxides of titanium,[25] this energy gap, as defined in the Figure 5-5, is found to 3.66 eV, greater than that for stoichiometric TiO_2.

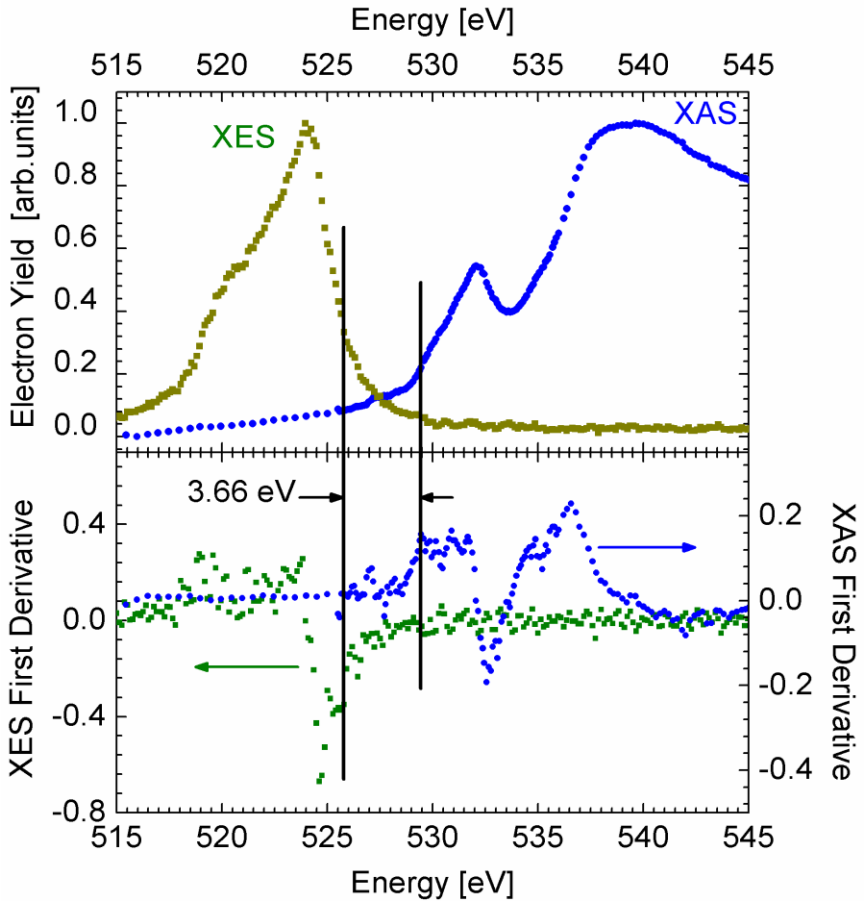

Figure 5-5 Combined O 1*s* x-ray emission and absorption spectra for Ti_xO_y-Fe_2O_3, with the first derivatives for each spectrum included for quantification of the energy difference between occupied and unoccupied *p* projected density of states.

5.8 Ultrafast transient absorption spectroscopy

Upon irradiation of α-Fe_2O_3 with energies exceeding the bandgap, free carrier creation and thermalization occurs on extremely fast time scales (< 150 fs;[43] < 75 fs[44]). Following this process, ultrafast transient absorption spectroscopy can be used to monitor the subsequent electron relaxation kinetics within the electronic structure of the system.[43,44,45,46] For this purpose, the Ti_xO_y-Fe_2O_3 was pumped with 540 nm (2.29 eV) 130 fs pulses, and the transient absorbance was collected over a broad range of probe energies. The resultant transient absorbance spectrum, collected 500 fs after excitation, is shown in Figure 5-6a (absorbance is plotted in terms of change in sample optical density). A spectral transient absorbance signal corresponds to carrier absorption with energy equivalent to the probe photon energy. By measuring these absorptions with time, the recombination dynamics are monitored on picosecond time scales.

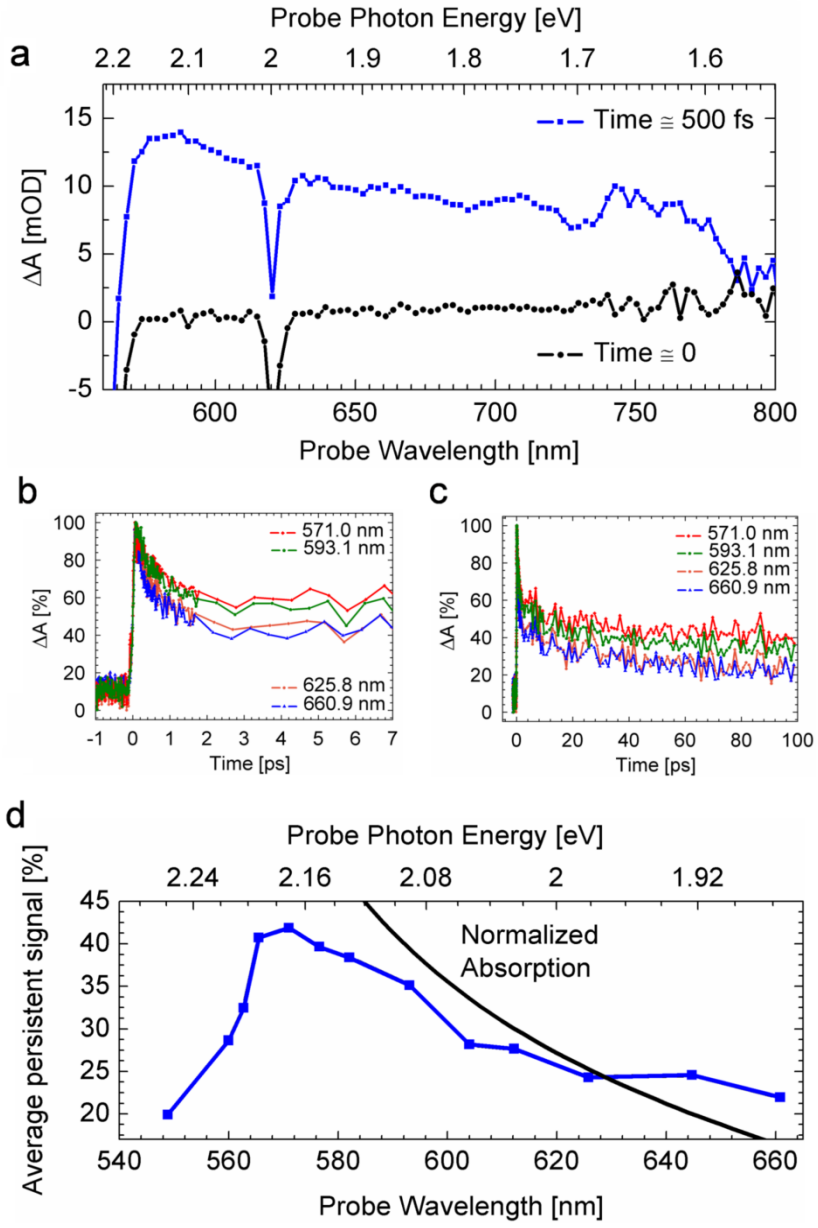

Figure 5-6 (a) Transient absorbance spectra before (black circles) and 500 fs (blue squares) after excitation. Normalized transient absorption signals for four representative probe wavelengths at ~1 ps (b) and ~10 ps (c) time regimes. (d) Transient absorption (averages of signals from 70 to 100 ps) after ultrafast excitation of Ti_xO_y-Fe_2O_3 array at various probe wavelengths (blue squares). Also included is the normalized steady-state absorption (black solid line), indicating the correlation of the transient data with the band edge.

.

Figure 5-6b and Figure 5-6c provide the system's normalized absorption transients at two time scales (0-7 ps and 0-100 ps) for representative probe energies. It is evident at ultrafast time scales

(Figure 5-6b) that relaxations from a broad range of states occur via a multiple exponential decay process. The fast decay component, which is commonly observed in iron oxides,[43] occurs within a few ps of the initial relaxation process. The longer component (Figure 5-6c) has a slower rate and persists to 100 ps and beyond. It is noted that the magnitudes of the decay processes depend on the probe energy, or in other words depend on the energetic position of the corresponding state.

In order to provide a quantitative measure of the spectral differences in decay magnitudes, the persistent absorption signal, defined as the average normalized absorption signal from 70 to 99 ps, was calculated. These values for several probe wavelengths are plotted in Figure 5-6d. Defined in this way, values of persistent absorption are a measure of the relative lifetimes of excited electrons in states with given energy signatures. It is shown in Figure 5-6 that the magnitudes of decay of electron relaxation processes depend on the energetic position of such states within the band structure. Interestingly, the maximum transient absorption signal, as averaged over this temporal range, was found to be near 570 nm, which is quite close to the bandgap of α-Fe_2O_3 and the measured band edge of the hetero-nanostructure array. To illustrate this correlation the normalized steady-state optical absorption is also included in Figure 5-6d (black line).

Previous transient absorption studies of α-Fe_2O_3 have attributed signals over this spectral range to absorption from trapped electrons, for example those electrons captured by surface Fe^{3+} species.[43,44] This argument is supported by the similar multiple exponential decay kinetics observed for a wide range of probe energies, which suggests these signals share a common physical origin.[44] Decay from these trap states is primarily nonradiative,[43] and is likely mediated by further interaction with lower-lying midgap states. Alternatively, those probe signals whose energies lie near the bandgap of α-Fe_2O_3 may relate to surface-trapped holes. A recent work[47] assigned transient absorption at 580 nm to holes in α-Fe_2O_3 photoanodes in operating PEC cells, which was corroborated by the utilization of interfacial hole scavenging chemicals.

Despite the context provided by these previous detailed investigations, the confident assignment of transient absorption signals to specific carriers in this material system remains obstructed by the complex nature of the constituent phases. Both phases contain high densities of localized *d* levels, associated with numerous optical transitions in the probed spectral range, as well as high densities of intrinsic and surface defect-induced trap states. Furthermore, the energetics of any previously observed surface trap states in α-Fe_2O_3 are expected to be influenced by the interfacial bonding environment in the hetero-nanostructure system. In addition, the known quantum-confinement effect in the α-Fe_2O_3[19] can potentially cause a spectral shift in the signatures of states electronically active in the relaxation process.

The detailed relationships of the system's carrier dynamics with those of α-Fe_2O_3 and titania crystals will be elucidated in a future investigation. However, this analysis has established the presence of a dense manifold of states, the relaxations from which exhibit multiple exponential decays. Decay magnitudes increase over the temporal range studied when corresponding probe energies deviate from energies near the measured band edge of Ti_xO_y-Fe_2O_3, which suggests there is some relationship between the excited carrier dynamics and the system band structure.

5.9 Conclusions from Chapter 5

This report has introduced a new transition metal oxide heterostructure containing junctions of iron oxide (hematite) and titanium oxide nanomaterials, which is readily organized in vertical arrays onto conductive substrates by a combination of inexpensive and scalable techniques. The orbital character of the interfacial region was analyzed by soft x-ray spectroscopies, which indicates the presence of a degree of *p-d* orbital hybridization that is absent from all reference crystals examined. Consideration of spectra relating to the Ti coordination environment suggests a structural relationship is established between the phases. The confirmed existence of Ti 3*d* electrons in the interface suggests the new hetero-nanostructure resulted in spontaneous electron enrichment and thus possesses a unique electronic structure, which likely translates to new emergent electronic properties. These macroscopic system properties are currently under investigation in our laboratories. It is foreseen that this fabrication strategy and the resultant novel materials will open new avenues to engineer the electrical and optical properties of transition metal oxide hetero-nanostructures, to specialize structures for critical applications of oxide electronics, most notably those for solar fuel generation and photovoltaics.

5.10 Experimental methods

5.10.1 Fabrication

The α-Fe_2O_3 nanorod arrays were first fabricated onto SnO_2:F-coated glass (FTO; Pilkington TEC7; 2.3 mm thickness) following the procedure described in reference 19. Ti_xO_y was deposited by ALD at 150 °C using the precursors $TiCl_4$ and H_2O.[48] The background flow rate was 80 SCCM N_2, and 15 cycles of Ti_xO_y were deposited with the pulsing sequence 3 s TiCl4, 60 s N_2 purge, 3 s H_2O, and 60 s N_2 purge. The TiO and Ti_2O_3 reference crystals were commercial powders (TiO: Alfa Aesar, 99.9%; Ti_2O_3: Alfa Aesar 99.8%). Anatase TiO_2 was prepared according to procedures in reference [49].

5.10.2 Soft x-ray spectroscopy

x-rays originate from an electronic transition between a localized core state and a valence state. Soft x-ray absorption spectroscopy provides information on the unoccupied electronic structure, and soft x-ray emission spectroscopy provides information on the occupied electronic structure. As a core state is involved, elemental selectivity is obtained because the core levels of different elements are well separated in energy, meaning that the involvement of the inner level makes this probe localized to one specific atomic site around which the electronic structure is reflected as a partial density-of-states contribution. The participation of valence electrons gives the method chemical state sensitivity and further, the dipole nature of the transitions gives particular symmetry information. The x-ray absorption and emission spectroscopy measurements were performed on Beamline 7.0.1 at the Advanced Light Source.

5.10.3 Ultrafast transient absorption spectroscopy

The ultrafast laser system is based on a Quantronix femtosecond laser system,[50] consisting of an Er-doped fiber oscillator, a regenerative/multi-pass amplifier, and a diode-pumped, Q-switched,

second harmonic Nd:YLF pump laser (527 nm, 10 W capacity). Before injection into the amplifier, chirped pulse amplification is performed to temporally stretch, amplify, and recompress the initial short pulse, resulting in a pulse near its original duration, albeit with a vastly higher energy level (sub-nJ raised to mJ). After amplification, the as-generated fundamental (795 nm) is beam-split to generate both a white light continuum (WLC) probe pulse as well as feeding a tunable optical parametric amplifier (OPA) consisting of two delay stages: a signal pre-amplification stage and a power amplification stage. The output of the OPA was passed through wavelength separators in order to achieve a tunable pump wavelength. The system operates at 750 Hz repetition rate.

The final output was ca. 130 fs pulses centered at 540 nm excitation wavelength which was attenuated with neutral density filters. The pump beam was overlapped spatially and temporally with the WLC probe beam at the sample. The time delay between the pump and probe beams was controlled by a translation stage with 1 μm resolution. Each sample was tested for four cycles to achieve a lower-noise average response.

5.11 References for Chapter 5

1. J. Mannhart and D. G. Schlom, *Science* **327**, 1607 (2010).
2. J. Chakhalian, J. W. Freeland, H.-U. Habermeier, G. Cristiani, G. Khaliullin, M. van Veenendaal, and B. Keimer, *Science* **318**, 1114 (2007).
3. P. Zubko, S. Gariglio, M. Gabay, P. Ghosez, and J.-M. Triscone, *Annu. Rev. Condense. Matter Phys.* **2**, 141 (2011).
4. A. J. Nozik, *Nano Lett*. **10**, 2735 (2010).
5. L. Vayssieres, *On Solar Hydrogen & Nanotechnology*; John Wiley and Sons: Singapore, 2009.
6. M. D. Archer and A. J. Nozik, *Nanostructured and Photoelectrochemical Systems for Solar Photon Conversion*; Imperial College Press: London, 2008.
7. H. A. Atwater and A. Polman, *Nature Mat*. **9**, 205 (2010).
8. A. Martí, E. Antolín, C. R. Stanley, C. D. Farmer, N. López, P. Díaz, E. Cánovas, P. G. Linares, and A. Luque, *Phys. Rev. Lett.* **97**, 247701 (2006).
9. M. Grätzel, *Inorg. Chem.* **44**, 6841 (2005).
10. N. Beermann, L. Vayssieres, S.-E. Lindquist, and A. Hagfeldt, *J. Electrochem. Soc.* **147**, 2456 (2000).
11. H. J. Snaith and C. Ducati, *Nano Lett.* **10**, 1259 (2010).
12. H. Zhong, Y. Zhou, Y. Yang, C. Yang, and Y. Li, *J. Phys. Chem. C* **111**, 6538 (2007).
13. J. Zhang, Y. Tang, K. Lee, and M. Ouyang, *Nature* **466**, 91 (2010).

14. M. G. Walter, E. L. Warren, J. R. McKone, S. W. Boettcher, Q. Mi, E. A. Santori, and N. S. Lewis, *Chem. Rev.* **110**, 6446 (2010).

15. L. Vayssieres, A. Hagfeldt, and S.-E. Lindquist, *Pure Appl. Chem.* **72**, 47 (2000).

16. R. L. Puurunen, *J. Appl. Phys.* **97**, 121301 (2005).

17. J. R. Bakke, H. J. Jung, J. T. Tanskanen, R. Sinclair, and S. F. Bent, *Chem. Mater.* **22**, 4669 (2010).

18. L. Vayssieres, N. Beermann, S.-E. Lindquist, and A. Hagfeldt, *Chem. Mater.* **13**, 233 (2001).

19. L. Vayssieres, C. Sathe, S. M. Butorin, D. K. Shuh, J. Nordgren, and J. Guo, *Adv. Mater.* **17**, 2320 (2005).

20. F.-T. Liou, C. Y. Yang, and S. N. Levine, *J. Electrochem. Soc*. **129**, 342 (1982).

21. L. Peng, T. Xie, Y. Lu, H. Fan, and D. Wang, *Phys. Chem. Chem. Phys.* **12**, 8033 (2010).

22. S. K. Mohapatra, S. Banerjee, and M. Misra, *Nanotechnology* **19**, 315601 (2008).

23. J. Guo, *Int. J. Quantum Chem.* **109**, 2714 (2009).

24. J. Biener, M. Bäumer, J. Wang, and R. J. Madix, *Surface Science* **450**, 12 (2000).

25. D. W. Fischer, and W. L. Baun, *J. Appl. Phys.* **39**, 4757 (1968).

26. F. M. F. de Groot, M. O. Figueiredo, M. J. Basto, M. Abbate, H. Petersen, and J. C. Fuggle, *Phys. Chem. Minerals* **19**, 140 (1992).

27. A. G. Thomas, W. R. Flavell, A. K. Mallick, A. R. Kumarasinghe, D. Tsoutsou, N. Khan, C. Chatwin, S. Rayner, and G. C. Smith, *Phys. Rev. B* **75**, 035105 (2007).

28. X. Chen, P.-A. Glans, X. Qiu, S. Dayal, W. D. Jennings, K. E. Smith, C. Burda, and J. Guo, *J.of Electron Spectroscopy and Related Phenomena* **162**, 67 (2008).

29. F. M. F. de Groot, J. C. Fuggle, B. T. Thole, and G. A. Sawatzky, *Phys. Rev. B* **41**, 928 (1990).

30. V. S. Lusvardi, M. A. Barteau, J. G. Chen, J. Eng Jr., B. Fruhberger, and A. Teplyakov, *Surface Science* **397**, 237 (1998).

31. J. P. Crocombette and F. Jollet, *J. Phys.: Condens. Matter* **6**, 10811 (1994).

32. J. Narayan and B. C. Larson, *J. Appl. Phys.* **93**, 278 (2003).

33. F. M. F. de Groot, M. Grioni, J. C. Fuggle, J. Ghijsen, G. A. Sawatzky, and H. Petersen, *Phys. Rev. B* **40**, 5715 (1989).

34. J. G. Chen, *Surf. Science Reports* **30**, 1 (1997).

35. T.-J. Park, S. Sambasivan, D. A. Fischer, W.-S. Yoon, J. A. Misewich, and S. S. Wong, *J. Phys. Chem. C* **112**, 10359 (2008).

36. S. Andersson, B. Collén, U. Kuylenstierna, and A. Magnéli, *Acta Chemica Scandinavica* **11**, 1641 (1957).

37. S.-i. Ohkoshi, Y. Tsunobuchi, T. Matsuda, K. Hashimoto, A. Namai, F. Hakoe, and H. Tokoro, *Nature Chem.* **2**, 539 (2010).

38. F. J. Morin, *Phys. Rev.* **93**, 1195 (1954).

39. F. J. Morin, *Bell System Tech. J.* **37**, 1047 (1958).

40. H. Liu, W. Yang, Y. Ma, and J. Yao, *Appl. Catal. A: General* **299**, 218 (2006).

41. J. M. Honig and T. B. Reed, *Phys. Rev.* **174**, 1020 (1968).

42. J. M. Honig, *Rev. Modern Phys.* **40**, 748 (1968).

43. N. J. Cherepy, D. B. Liston, J. A. Lovejoy, H. Deng, and J. Z. Zhang, *J. Phys. Chem. B* **102**, 770 (1998).

44. V. A. Nadtochenko, N. N. Denisov, V. Yu. Gak, F. E. Gostev, A. A. Titov, O. M. Sarkisov, and V. V. Nikandrov, *Russian Chem. Bulletin, International Edition* **51**, 457 (2002).

45. A. G. Joly, J. R. Williams, S. A. Chambers, G. Xiong, W. P. Hess, and D. M. Laman, *J. Appl. Phys.* **99**, 053521 (2006).

46. Y. P. He, Y. M. Miao, C. R. Li, S. Q. Wang, L. Cao, S. S. Xie, G. Z. Yang, B. S. Zou, and C. Burda, *Phys. Rev. B* **71**, 125411 (2005).

47. S. R. Pendlebury, M. Barroso, A. J. Cowan, K. Sivula, J. Tang, M. Grätzel, D. Klug, and J.R. Durrant, *Chem. Commun.* **47**, 716 (2011).

48. P. Ardalan, T. B. Brennan, H. B. R. Lee, J. R. Bakke, I. K. Ding, M. D. McGehee, and S. F. Bent, *ACS Nano* **5**, 1495 (2011).

49. A. Mattsson, M. Leideborg, K. Larsson, G. Westin, and L. Österlund, *J. Phys. Chem. B* **110**, 1210 (2006).

50. R. J. Newhouse, H. Wang, J. K. Hensel, D. A. Wheeler, S. Zou, and J. Z. Zhang, *J. Phys. Chem. Lett.* **2**, 228 (2011).

6 TiO_2-SnO_2:F interfacial electronic structure investigated by soft x-ray absorption spectroscopy

Chapter 6 is an adaptation of a published article:

Coleman X. Kronawitter, Mukes Kapilashrami, Jonathan R. Bakke, Stacey F. Bent, Cheng-Hao Chuang, Way-Faung Pong, Jinghua Guo, Lionel Vayssieres, and Samuel S. Mao, *Phys. Rev. B* **85**, 125109 (2012).

6.1 Abstract for Chapter 6

The electronic structure of the titanium dioxide (TiO_2) - fluorine-doped tin dioxide (FTO) interface is investigated by soft x-ray absorption spectroscopy using synchrotron radiation. The measurements probe the site- and symmetry-selected unoccupied density-of-states, and reflect a complex interaction between an early transition metal oxide (d^0) semiconductor and a post-transition metal oxide (d^{10}) degenerate semiconductor. The distinct interfacial electronic structure of TiO_2-FTO is established by contrasting spectra with those for anatase and rutile TiO_2, FTO, and ZnO-FTO and CdO-FTO interfaces. Oxygen 1*s* absorption spectra, which relate to the O 2*p* partial density-of-states of the conduction band, indicate that the interface is associated with a reduction in Ti *d* - O *p* orbital hybridization and an alteration of the TiO_2 crystal field. These observations are consistent with measured titanium 2*p* absorption spectra, which in addition provide evidence for distortion of long-range order around the cation site in the interfacial TiO_2. The TiO_2-FTO interface is a functional component of a number of optoelectronic devices, perhaps most notably within the anode structure of solar cell architectures. In non-equilibrium conditions such as those found in operating solar cells interfacial electronic structure directly influences performance, for instance by modifying the quasi-Fermi level of electrons and the potential distribution at the transparent electrode.

6.2 Introduction to Chapter 6

Performance in modern optoelectronics is increasingly reliant on the efficiency of interfacial processes, which are directly influenced by the character and occupancy of electronic states near the interface. Devices designed to absorb or emit light contain layers of organic or inorganic heterostructures, which either function as active components or which facilitate the extraction or injection of electrons from or to the optically active phases. The interfacial regions of heterostructures, which can extend several nanometers beyond their actual atomic interfaces, can be characterized by abrupt or gradual changes in chemical, structural, and electronic properties.[1] The nature of these atomic- and molecular-level interactions is not restricted to academic interest; the macroscopic performance of modern technologies is often reliant on their presence. Here we can consider for example the various incarnations of the excitonic solar cell,[2] and its inorganic counterpart the quantum dot solar cell,[3] whose very operation requires exciton dissociation and electron transfer processes, which are interfacial phenomena. In general the

significance of heterostructure properties is amplified in nanodevices, the large junction areas within which contribute considerably to the overall device functionality.

In transition metal oxide heterostructures, charge transfer, covalent bonding, and orbital reconstruction effects modify the *d* orbital character and occupancy at the interface.[4] These effects are expressed through a number of new discoveries whose related technologies will rely on precise knowledge of the interface electronic structure, such as those utilizing interfacial conductivity,[5] magnetism,[6] or electron enrichment.[7] Size effects in low-dimensional oxides further influence interfacial chemistry[8] and electronic structure through enhancements in orbital hybridization[9] and through quantum confinement.[10]

Here we examine the electronic structure of the interface of titanium dioxide (TiO_2) and fluorine-doped tin dioxide (SnO_2:F, FTO), a transparent conductive oxide (TCO). FTO is the preferred transparent electrode material for numerous optoelectronic applications and is notable for its thermal stability over a wide range of processing temperatures. The buried interfaces are studied by synchrotron-based soft x-ray absorption spectroscopy (XAS), which provides spectra related to the site- and symmetry-selected unoccupied density of states. The key experimental requirement is the deposition of ultrathin layers, whose feature dimensions should not exceed the inelastic mean free path of electrons (*ca.* 1-10 nm). This enables the measurement of electron yields generated from transitions originating exclusively from the interfacial region upon synchrotron soft x-ray irradiation. For comparative purposes we examine some aspects of CdO- and ZnO-FTO interfaces (all post-transition metal oxides), mainly to highlight the relative chemical sensitivity and specificity of the TiO_2 phase. We adopt the notation SnO_2:F to refer to the FTO phase, and ZnO and CdO to refer to the binary post-transition metal oxides, which are expected to remain stoichiometric in these conditions due to the very high ionization potentials of monovalent cations. The TiO_2 phase is strongly influenced by the substrate as will be discussed in detail herein. However, for convenience we refer to the ultrathin titanium oxide as TiO_2, given that similar preparation conditions for thicker films produce stoichiometric TiO_2.[11]

Comprehensive understanding of the electronic structure of oxide-TCO interfaces contributes to continuing efforts to optimize a number of optoelectronic devices of considerable social consequence. The oxide-TCO interface be found in dye-sensitized,[12,13,14] quantum dot-sensitized,[15] organic,[16] and solid-state solar cells,[17,18,19], in light emitting[20] and organic light emitting diodes, as well as in solar water splitting photoanodes.[21] In nanodevices the interface may result from the direct growth of nanomaterials onto TCO electrodes[22] or through the use of seed layers[23] to facilitate nanomaterial growth. In all cases, during device operation electrons are transported through the interfacial region, where they interact with the interface electronic structure. For instance, in dye-sensitized solar cells the open circuit potential can be limited by recombination at the metal oxide-TCO interface.[24] Additionally it has recently been demonstrated that annealing α-Fe_2O_3 photoanodes at high temperatures alters the nature of the α-Fe_2O_3-TCO interface, leading to a dramatic increase in water oxidation photocurrents in photoelectrochemical cells.[25] Another recent report, which has motivations similar to those in this study, has characterized the TiO_2-indium tin oxide interface electronic structure through photoemission spectroscopy.[26] A fundamental understanding of the oxide-TCO interface provides direction to address operational deficiencies at their physical source. To best facilitate these important fields, we fabricated heterostructures using techniques that realistically represent

actual fabrication steps for these devices: use of commercial polycrystalline FTO substrates, low temperatures, and moderate pressures.

6.3 Experiment

Ultrathin films of TiO_2, ZnO, and CdO were fabricated by atomic layer deposition. Films were deposited onto commercial FTO substrates (Pilkington, TEC 7) at 150 °C utilizing titanium tetrachloride, diethyl zinc dimethyl cadmium, and water as the precursors. The pulsing sequence for each system was 3 s metal molecule, 60 s N_2 purge, 3 s water, and 60 s N_2 purge where the N_2 purge and carrier flow rate is constant at 80 SCCM. Six cycles of ZnO and CdO and 15 cycles of TiO_2 were performed so that the thickness of each oxide is 12 ± 2 Å [11,27]. Prior to measurement, all samples were annealed in air at 450 °C for 2 hrs (0.36 °C s^{-1} ramp rate from 23 °C to 450 °C), to ensure the crystallinity of all phases.

Soft x-ray absorption spectra were measured on Beamline 8.0 at the Advanced Light Source (ALS) at Lawrence Berkeley National Laboratory. Spectra were recorded in total electron yield mode, and were obtained by measurement of the sample drain photocurrent under irradiation with monochromatic light. The resolutions of the measurements were 0.4 eV at the O *K*-edge, 0.35 eV at the Sn *M*-edge, and 0.3 eV at the Ti *L*-edge. The incident radiation flux was monitored by the photocurrent produced in a gold mesh in the beam path. The photon energy was calibrated using the first peak of the anatase TiO_2 O l*s* absorption spectrum located at 530.8 eV. Absorption spectra for anatase and rutile TiO_2 were measured on Beamline 7.0.1 at the ALS.

6.4 Results and Discussion

Soft x-ray absorption spectroscopy probes the site- and symmetry-selected unoccupied density-of-states through an electronic transition between a localized core state and a valence state in the oxide materials. The large energy separation among core levels gives the technique elemental selectivity, the participation of valence electrons yields chemical state sensitivity, and the dipole nature of the transitions provides symmetry information. The probe is localized to one specific atomic site, around which the electronic structure is reflected as a partial density-of-states contribution.

To provide context to an analysis of interfacial x-ray absorption spectra, a few important distinctions are necessary to be made between TiO_2 and the post-transition metal oxides SnO_2, ZnO, and CdO. In TiO_2, Ti ions have a $Ti^{4+}(3d^0)$ electronic configuration and the empty conduction band is comprised of Ti 3*d*, 4*s*, and 4*p* orbitals, with 3*d* orbitals dominant in the bottom of the conduction band. In contrast, in SnO_2 for example, Sn ions have a $Sn^{4+}(4d^{10}5s^05p^0)$ configuration, with 5*s* and 5*p* orbitals dominant in the conduction band minimum.[28] In addition, with a few exceptions the post-transition metal oxide cations have one preferred oxidation state, whereas in the transition metal oxides there is often a small energy

difference between the d^n and d^{n+1} configurations. As a result, the transition metals typically have many stable oxides and their surface and interface chemistry is much more complex.[29] These complexities are evident in x-ray absorption spectra; their interpretation requires the inclusion of titanium oxide reference spectra. There are additional properties specific to the reference oxides examined which must be briefly addressed. The anisotropy and surface polarity of ZnO are important aspects of this material,[30] which directly influence electronic structure measurements. Additionally, the large electron accumulation in CdO,[31] associated with massive band bending, is not characteristic of TiO_2 and should be noted. These factors should not influence our interpretations to any significant degree.

6.4.1 Oxygen 1s soft x-ray absorption

Upon irradiation of the oxides with x-rays of sufficient energies, core O 1*s* electrons are promoted to an excited state, which is coupled to the original state by the dipole selection rule.[32] The change in angular momentum quantum number (ΔL) must be ± 1 – only the oxygen *p* character is probed. The existence of these transitions in itself is an indication of the partially covalent bonding in these materials.[33] For this application, O 1*s* spectra provide a useful representation of the unoccupied electronic structure at interfacial metal sites, because in these materials above the Fermi level empty bands are predominantly metal weight hybridized with O 2*p* character.

The O 1*s* absorption spectra for the un-modified SnO_2:F surface and the TiO_2-SnO_2:F, ZnO-SnO_2:F, and CdO-SnO_2:F interfaces are provided in Figure 6-1. The qualitatively similar spectrum measured for all cases confirms the validity of the ultrathin film approach to probe the interface: the buried SnO_2:F dominates the expression of O *p* states in each XAS measurement. In other words, because the inelastic mean free path is restricted to *ca.* 1-10 nm, the signal represents the O *p* states of the interface, defined as a region approximately 2 nm on either side of the atomic interface.

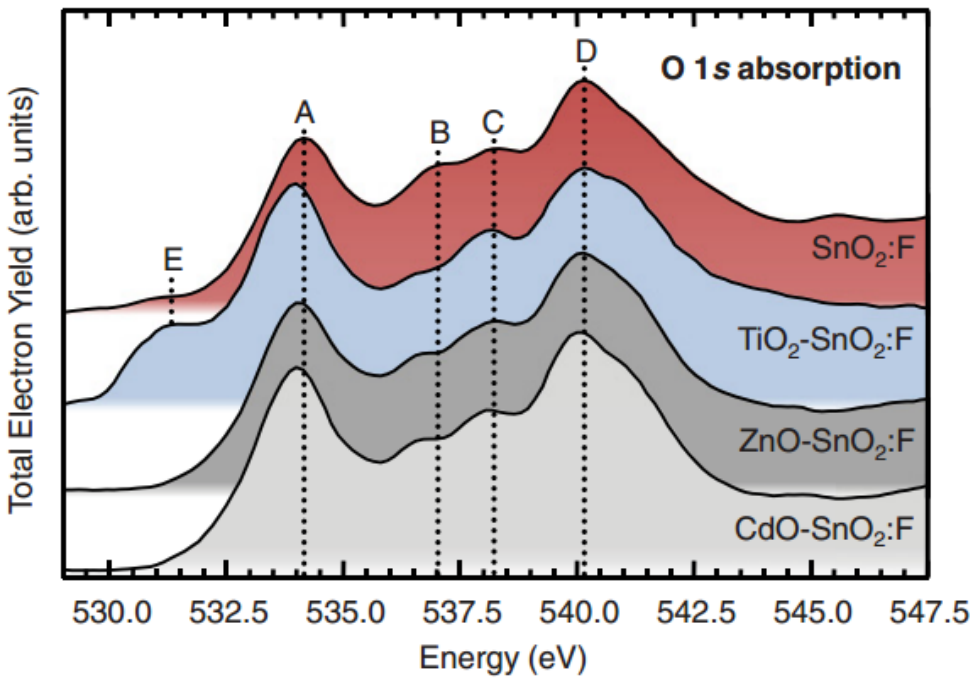

Figure 6-1 O *K*-edge x-ray absorption spectra for (from top to bottom) un-modified SnO_2:F and the TiO_2-SnO_2:F, ZnO-SnO_2:F, and CdO-SnO_2:F interfaces.

The bottom of the conduction band of SnO_2 is comprised of Sn 5*s* orbitals, which hybridize with O 2*p* orbitals and are expressed in the O 1*s* absorption spectra as peak *A* in Figure 6-1. Peaks *B*, *C*, and *D* primarily correspond to the O 2*p* orbitals hybridized with Sn 5*p* orbitals deeper in the conduction band.[34] In the molecular orbital framework, peak *A* corresponds to transition to the a_g state, and peaks *B*, *C*, and *D* correspond to the successive transitions to the b_{1u}, b_{2u}, and b_{3u} states.[35] The a_g state reflects the partial density of states of the O_2 set of oxygen orbitals, which are perpendicular to the plane of the Sn_3O trigonal configuration, while the b_{1u}, b_{2u}, and b_{3u} states reflect a combination of the in-plane O_1 set and out-of-plane O_2 set.[34,36] Peak *E*, located in the pre-edge region at 531.4 eV, is found uniquely in TiO_2-SnO_2:F, and results from the hybridization of unoccupied Ti $d(t_{2g})$ levels with O 2*p* levels, which exist in the conduction bands of titanium oxides, as will be discussed in detail later in this report. Close inspection of the rising edge of peak *A* reveals additional intensity near 533.4 eV for all thin film samples. This is attributed to Ti 3*d*-, Zn 4*s*-, and Cd 5*s* - O 2*p* hybridized states, which exist in the respective conduction bands of the oxides.[37]

6.4.2 Tin 3d soft x-ray absorption

The Sn $M_{4,5}$-edge x-ray absorption spectra, presented in Figure 6-2, describe transitions from Sn 3*d* levels to *p* or *f* states in the conduction band of SnO_2:F. The lower signal-to-noise ratio in comparison to those for O *K*-edge spectra results from the much lower x-ray absorption cross

section of the *M*-edge. The conduction band minimum of SnO_2 is dominantly comprised of Sn 5*s* levels. Deeper in the conduction band the density-of-states is dominantly Sn *p* character.[38]

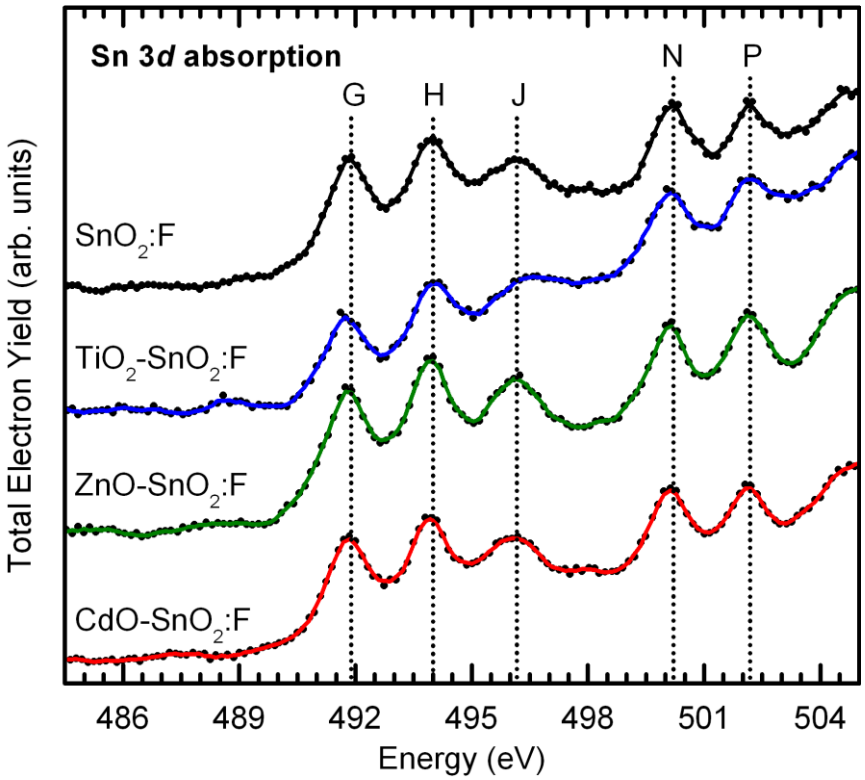

Figure 6-2 Sn $M_{4,5}$-edge absorption spectra for un-modified SnO_2:F (black solid line), and the TiO_2-SnO_2:F (blue solid line), ZnO-SnO_2:F (green solid line), and CdO-SnO_2:F (red solid line) interfaces.

It is apparent in Figure 6-2 that Sn 3*d* absorption at the surface of SnO_2:F is largely unchanged by the formation of an interface with CdO and ZnO. Here we can consider the relative chemical stability of the post-transition metal oxides. High energies are required to add or remove electrons when these cations are coordinated with O^{2-} ligands, limiting the number of states accessible for the formation of defects, which have different electron configurations.[29] These spectra contrast with that of TiO_2-SnO_2:F, which contains a large distortion of the M_4 and M_5 bands. The broadening and overall reduction in resolution of these peaks compared to those for un-modified SnO_2:F has been found in x-ray absorption spectra for SnO.[39] Through consideration of high-surface-area SnO_2 aerogels, Kucheyev *et al.*[39] assigned the distortion to the presence of under-coordinated surface atoms. Ahn *et al.*[40] observed a similar broadening in their study of size-controlled SnO_2 nanoparticles, where increased broadening was found to be correlated with decreasing nanoparticle size. Broadening in this case was attributed to decreasing long-range order in SnO_2 crystals.

The small leading edge feature near 488.5 eV present in the M_5 band for TiO_2-SnO_2:F has been identified previously in SnO_2 aerogels[39] and nanoribbons.[41] It is suggested to be related to Sn *p* states that are created by oxygen vacancies and surface reconstruction. The spin orbit splitting creates an M_4 band counterpart that overlaps with peak *J*, which explains the dramatic distortion

of this peak in our experiments. Surface reconstruction of this type will alter the Fermi level position of the heterostructure.[39] The presence of additional Sn *p* states, which have been assigned to exist both below[42] and above[39] the conduction band minimum, potentially alters the electronic structure of the conduction band. In order to confirm the presence of SnO_2 surface reconstruction, which is only observed indirectly here, more detailed analyses are required, for example those involving high-resolution transmission electron microscopy.

6.4.3 Titanium 3d band projected onto O 2p orbitals

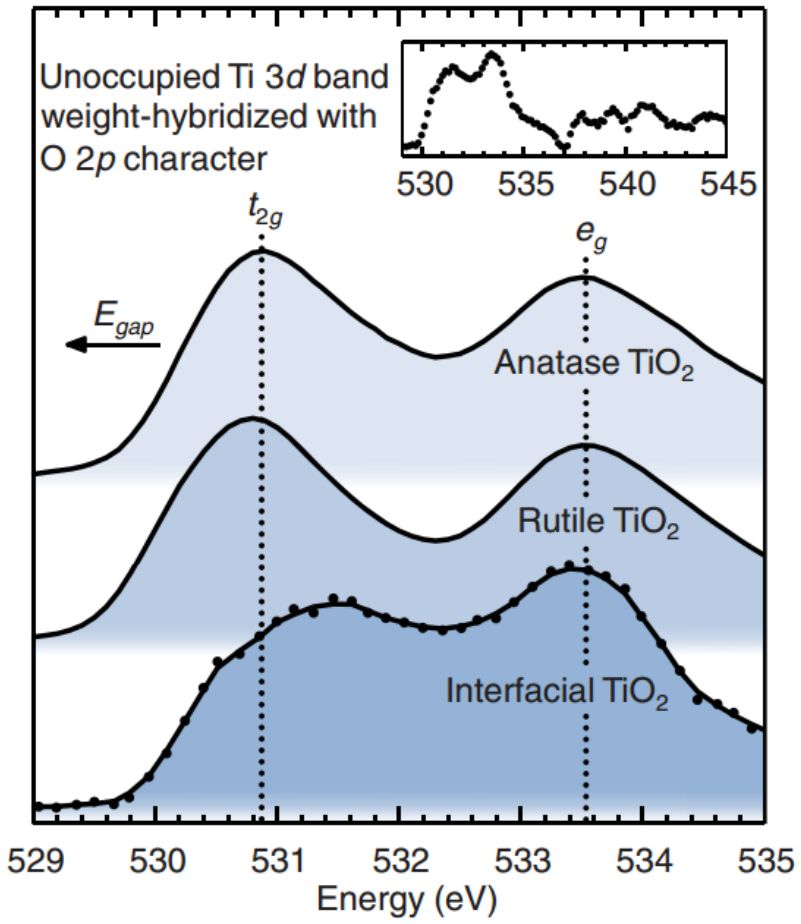

Figure 6-3 Oxygen 1*s* absorption spectra for anatase TiO_2, rutile TiO_2, and TiO_2 thin film deposited on SnO_2:F. The interfacial TiO_2 spectrum was obtained by subtraction of the SnO_2:F O 1*s* absorption spectrum. The dashed vertical lines indicate the positions of the Ti t_{2g} and e_g bands of anatase TiO_2.

The strong intensity of peak *E* in Figure 6-1, which corresponds primarily to unoccupied O 2*p* states, weight-hybridized in states with Ti 3*d* character,[9] enables more detailed analysis of the conduction band minimum of TiO_2 at its interface with SnO_2:F. The difference spectrum obtained by subtraction of the SnO_2:F O 1*s* absorption spectrum from that of TiO_2-SnO_2:F (such that the resulting spectrum intensity is positive) is presented in Figure 6-3, with O 1*s* absorption

spectra of anatase and rutile TiO_2 included for comparison. The Ti 3*d* band of the O l*s* absorption spectrum (located from 529 eV to 535 eV[7]) is of primary interest to this study, and the difference spectrum in this energy range possesses a high signal-to-noise ratio, highlighting the importance of XAS for studying d^0 materials. The 4*sp* band is located at higher energies (inset of Figure 6-3) and possesses a larger energy spread, which is related to the degree of covalency in the material.[32] Increased broadening of this band is consistent with previous investigations of size effects in TiO_2,[9] as described in detail below. It is possible that the O 1*s* absorption spectrum of the underlying SnO_2:F, modified by the presence of the TiO_2, is not the same as that of un-modified SnO_2:F. (see discussion above on the Sn *M*-edge). The analysis of the difference spectrum that follows is conducted in the context of this unavoidable limitation.

In the oxides of titanium, Ti cations are surrounded by a distorted octahedron of oxygen anions, and the associated electrostatic fields split the *d* orbitals into a triply degenerate t_{2g} band (d_{xy}, d_{xz}, and d_{yz} orbitals) and a doubly degenerate e_g band (d_{x2-y2} and d_{z2} orbitals). The dashed vertical lines in Figure 6-3 show the positions of the t_{2g} and e_g bands hybridized with O 2*p* orbitals in the conduction band of anatase TiO_2. The center energies of the peaks corresponding to the e_g bands nearly overlap among anatase TiO_2, rutile TiO_2, and TiO_2-SnO_2:F. In contrast, the centroid of the t_{2g} peak for TiO_2-SnO_2:F lies at greater energies than reference titanium oxides.

The energy separation between the O 2*p* weights of the t_{2g} and e_g sub-bands is a reflection of the ligand-field strength, or the ligand-field splitting parameter Δ.[32] This parameter depends on the specific metal and ligand involved, as well as the oxidation state of the metal, and in general for a given metal the ligand field strength increases with increasing oxidation state. In the TiO_2-SnO_2:F interface, structural distortions in the lattice could change the symmetry of the cation site environment, which would be associated with a change in the ligand field. Interestingly, Soriano *et al.*[43] showed that structural disorder in TiO_2 induced by surface sputtering is associated with a 0.6 eV reduction in the ligand-field splitting, which was attributed to weaker Ti 3*d* - O 2*p* hybridization.

An alteration of the titanium oxide ligand-field is notable in this analysis of the interface electronic structure: the field influences the orientation of *d* orbitals around the metal ion in transition metal oxide systems, and by extension many of the system's physical properties. A large deviation of the ligand-field at the TiO_2-SnO_2:F interface from that of reference TiO_2 will influence electron conduction, which primarily takes place in empty Ti 3*d* orbitals. Significant alterations of the ligand-field strength suggest the presence of further distortion of the octahedral coordination of Ti.

The line shape of O l*s* absorption spectra in this energy range is additionally modified by size effects related to the high density of interface and surface states in nanoscale systems. Vayssieres *et al.*[9] recently examined the size effect on the orbital character of TiO_2 nanoparticles over three length scales. It was determined that, as a consequence of the contracted nature of *d* orbitals, the hybridization of O 2*p* with Ti 4*s* orbitals is of greater importance in systems with nanoscale dimensionality and high concentrations of surface states. It is reasonable to assume in the present case that interface and surface states manifest as line broadening in the measured O ls absorption spectra, consistent with an enhancement of *s-p* orbital hybridization.

6.4.4 Titanium 2p soft x-ray absorption

Titanium *L*-edge absorption spectra were recorded to provide additional information on the interfacial cation site environment of TiO_2-SnO_2:F. For comparison, as above, spectra were recorded for anatase and rutile TiO_2 reference crystals. These spectra, presented in Figure 6-4a, possess four primary peaks, which result from the core-hole spin-orbit splitting of $2p$ levels and the crystal-field splitting of d orbitals discussed above.[44,45,46,47] Specifically, the L_3 band, located from 456 to 462 eV, represents the $2p_{3/2} \rightarrow 3d4s$ transition; the L_2 band located from 462 to 468 eV represents the $2p_{1/2} \rightarrow 3d4s$ transition. Peaks *T* and *W* reflect transitions to empty t_{2g} levels and Peaks *U, V*, and *Y* reflect transitions to empty e_g levels.

In the final state of the Ti $2p$ x-ray absorption process, the significant overlap of core and valence wavefunctions is expressed as multiplet effects, which remain largely unscreened in the solid state. These describe primarily atomic effects associated with electronic transitions (intra-ionic transitions) of the general form $2p^6d^n \rightarrow 2p^5d^{n+1}$. For this reason they can be simulated by calculations in the context of atomic multiplet theory with modifications to account for the crystal field and charge transfer effects, [48] or through multichannel multiple-scattering calculations.[49] The leading edge multiplet structure of TiO_2 (peaks *R* and *S*), have been assigned in analyses to $2p^6d^0 \rightarrow 2p^5d^1$ for Ti^{4+} in O_h symmetry.[50] The Ti $2p$ absorption spectra in Figure 6-4a indicate the Ti oxidation state in interfacial TiO_2 is primarily 4+.

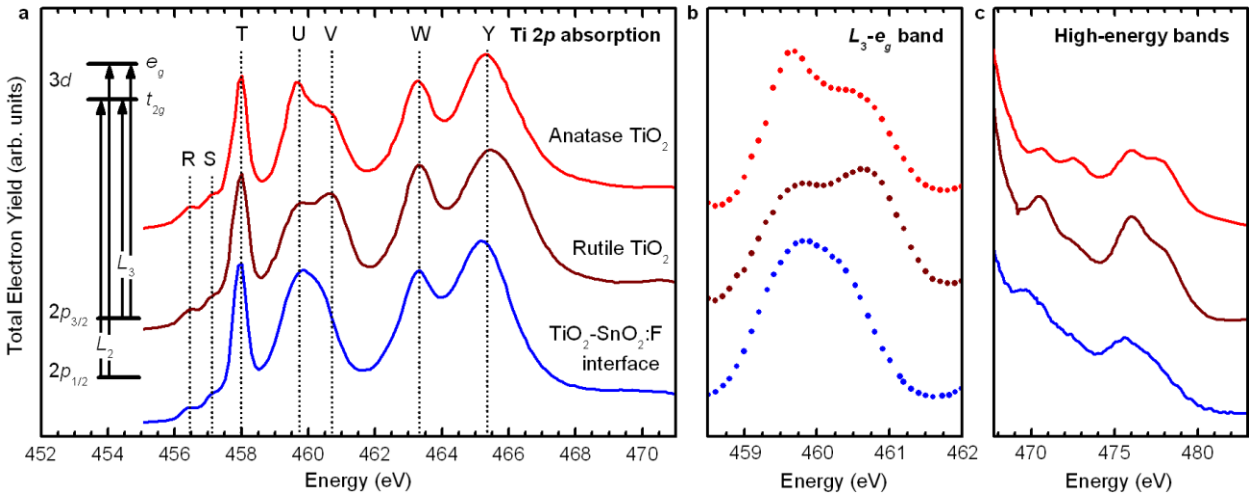

Figure 6-4 Ti $L_{2,3}$-edge x-ray absorption spectra for (top to bottom) anatase TiO_2 (red), rutile TiO_2 (dark red), and TiO_2-SnO_2:F (blue). (a) Complete spectra; (b) L_3-e_g band; (c) High-energy bands, normalized to peak *Y*. (b) and (c) follow the same order and color convention as in (a).

We now consider the L_3-e_g band (peaks *U* and *V*, Figure 6-4b), which shows the greatest variation in intensity among the various titanium oxides examined. The e_g orbitals point directly to the ligands and as a result the projection of their energy levels in x-ray absorption spectra provides a signature of the cation site environment. It is evident from the comparison of *L*-edge spectra provided in Figure 6-4b that the line shape of the L_3-e_g band is sensitive to the symmetry

of the cation. For all samples the e_g band is split into an asymmetric doublet, the origins of which have been explained through a number of interpretations. Kucheyev *et al.*[51] discussed these recently in their study of titanium oxide aerogels, and through comparisons with amorphous titanium oxide suggested long-range order effects contribute to the line shapes. Based on a neglible change in peak positions with reduction in sample temperature, they also suggested that the dynamic Jahn-Teller effect is not a major contributor to the e_g band splitting. Calculations of the expected Ti $L_{2,3}$ absorption-edge shapes performed by Crocombette *et al.*[52] determined that the influence of first-neighbor interactions cannot account for the large e_g splitting observed in these spectra. This was recently explicitly confirmed in a study by Krüger[49], which reported Ti $L_{2,3}$-edge absorption spectra as simulated by the first-principles multichannel multiple-scattering method, with large numbers of TiO_6 clusters. The splitting of the L_3-e_g band could only be reproduced after consideration of a cluster size of about 60 atoms, which corresponds to a length scale of ~1 nm. This analysis of the L_3-e_g band suggests that TiO_2-SnO_2:F differs in its long-range order from the titanium oxide reference crystals. The physical correlate to this electronic structure observation could be the structural discontinuity that occurs at the substrate-film interface. Disorder on this length scale could reflect a strain gradient and/or relaxation in the interfacial TiO_2. The line shape of the L_3-e_g band appears similar to those found for unrelaxed amorphous TiO_2 prepared by ion bombardment of rutile TiO_2.[51] These disorder-induced modifications to the interfacial electronic structure are expected to exist within larger crystals deposited onto SnO_2:F, which would be strained near the interface and relaxed toward bulk properties farther from the interface.

The high-energy region of the Ti 2*p* absorption spectra, located between 468 and 480 eV (Figure 6-4c), shows variation among anatase, rutile, and the interfacial TiO_2. This energy range contains two bands separated by 5-6 eV, which have been suggested to originate from $2p_{3/2}$ and $2p_{1/2}$ transitions,[51] as discussed above. The line shapes of these features have been attributed to polaronic transitions,[53] the partial Ti 3*d* and Ti 4*s* density-of-states,[50] and in the molecular orbital description to transitions from Ti 2*p* core levels to t_{1u}-type orbitals.[51,54] The peaks' doublet structure, most evident in the spectrum for anatase TiO_2, is not resolved in the spectrum for TiO_2-SnO_2:F. Generally we observe broadening of the peaks, which is consistent with the disruption of long-range order discussed above with respect to the L_3-e_g band.

Observation of unique ordering on a length scale of 1 nm in interfacial TiO_2 has a number of implications for carrier transport through the TiO_2-SnO_2:F interface during device operation. For example, the corundum crystal structure and associated distorted octahedral symmetry of Ti_2O_3 causes splitting of conduction band t_{2g} states into sub-bands in this material.[55] Specifically, in Ti_2O_3 t_{2g} states are split into bonding and antibonding a_{1g} sub-bands, which surround a e_g^{π} sub-band. This creates a bandgap and results in semiconducting behavior. Although these features of the TiO_2-SnO_2:F interface cannot be determined from data presented in this report, it is interesting to consider the interfacial bonding environment is associated with a number of possible conduction band structures. The unique dispersion of the interfacial Ti 3*d* band, projected onto O *p* orbitals in O 1*s* absorption spectra in Figure 6-3, provides additional evidence of the type of long-range order to which these data refer.

6.4.5 TiO_2-SnO_2:F interfaces in solar cells

The data presented in this report suggest the electronic structure of the TiO_2-FTO interface contrasts with that of its constituent reference crystals through distinct alterations of the crystal-field and long-range order of the cation site environment. These observations provide evidence toward understanding the operation of optoelectronic devices utilizing this interface, which often possess feature dimensionality on the length scale over which the interface was probed in this study. For example, dye-sensitized solar cells commonly utilize as electron transport phases colloidal films of TiO_2 nanoparticles whose diameter is on the order of ten nanometers.[12] The nature of the TiO_2-SnO_2:F interface may play a critical role in determining the performance of these devices. It is generally interpreted that the open circuit potential of dye-sensitized solar cells is limited by the energy difference between the TiO_2 conduction band and the redox potential of the electrolyte.[56] However, the TiO_2-SnO_2:F interface can significantly influence operating parameters such as the fill factor.[57] Rühle and Cahen[57] analyzed the electrostatic potential distribution at the TiO_2-SnO_2:F interface and simulated cell performance with an analytical expression for electron tunneling through an electrostatic barrier. The potential distribution from this analysis suggests the existence of an TiO_2-SnO_2:F interfacial potential barrier width of approximately 1 nm. This is the same length scale over which we observe distinct dissimilarities between the electronic structure of the interface and those of all reference titania crystals. Inorganic solid-state solar cells with similar anode architectures, such as extremely-thin-absorber cells,[20] require compact TiO_2 thin films to prevent recombination current during operation. In such cells the potential distribution in this layer should be engineered to promote the efficient injection of electrons from TiO_2 into SnO_2:F. For example, photocurrent transient measurements performed by Rühle and Dittrich[58] suggest increased narrowness of the electrostatic potential drop at the TiO_2-SnO_2:F interface may be required to increase the performance of such cells. In most applications, the translation of electrochemical potential of electrons in TiO_2 to an electrostatic potential at the TiO_2-SnO_2;F interface[56] is expected to be influenced by the unoccupied density-of-states studied experimentally in this report. The description of the electronic structure provided by these measurements suggests, for example, that in non-equilibrium conditions (*i.e.* solar cell operating conditions), the quasi-Fermi level of electrons in the interface will differ from what is expected by consideration of the respective bulk semiconductor properties of the constituent phases.

6.5 Conclusions from Chapter 6

The electronic structure of the TiO_2-FTO interface, an important structure for a number of optoelectronic devices, has been investigated by soft x-ray absorption spectroscopy. The distinct interfacial electronic structure of TiO_2-FTO has been established by contrasting spectra with those for anatase and rutile TiO_2, FTO, and the ZnO-FTO and CdO-FTO interfaces. The Ti 3*d* band of the interfacial oxygen 1*s* absorption spectrum indicates a reduction in the degree of *p*-*d* hybridization and an alteration of the TiO_2 crystal field. Titanium 2*p* absorption spectra provide evidence for distortion of long-range order around Ti ions in the interfacial TiO_2.

These observations can inform methodology to address operational deficiencies associated with the TiO_2-FTO interface in optoelectronic devices. For example, a comprehensive characterization of the chemically-resolved interfacial electronic structure provides information that facilitates the elimination of unfavorable processing conditions, for example high temperatures, which are associated with additional costs and diffusion effects between phases, and which preclude the use of inexpensive temperature-sensitive substrates. The results indicate that in solar cell operating conditions, the quasi-Fermi level of electrons in the interface will differ from predictions based on bulk oxide material properties. The interfacial electronic structure in addition influences the electrostatic potential distribution at the oxide-TCO interface, which is often a critical operational aspect of working optoelectronic devices. The description of the unoccupied electronic states at the TiO_2-SnO_2:F interface presented in this report provides additional information toward explaining deviations in solar cell performance metrics from those expected by bulk material properties and the various predictive models.

6.6 References for Chapter 6

1. P. Zubko, S. Gariglio, M. Gabay, P. Ghosez, and J.-M. Triscone, *Annu. Rev. Condens. Matter Phys.* **2**, 141 (2011).

2. B. A. Gregg, *J. Phys. Chem. B* **107**, 4688 (2003).

3. A. J. Nozik, *Nano Lett.* **10**, 2735 (2010).

4. J. Chakhalian, J. W. Freeland, H.-U. Habermeier, G. Cristiani, G. Khaliullin, M. van Veenendaal, and B. Keimer, *Science* **318**, 1114 (2007).

5. A. Ohtomo and H. Y. Hwang, *Nature* **427**, 423 (2004).

6. A. Brinkman, M. Huijben, M. van Zalk, J. Huijben, U. Zeitler, J. C. Maan, W. G. van der Wiel, G. Rijnders, D. H. A. Blank, and H. Hilgenkamp, *Nature Mater.* **6**, 493 (2007).

7. C. X. Kronawitter, J. R. Bakke, D. A. Wheeler, W.-C. Wang, C. Chang, B. R. Antoun, J. Z. Zhang, J.-H. Guo, S. F. Bent, S. S. Mao, and L. Vayssieres, *Nano Lett*. **11**, 3855 (2011).

8. L. Vayssieres, *J. Phys. Chem.* C **113**, 4733 (2009).

9. L. Vayssieres, C. Persson, and J.-H. Guo, *Appl. Phys. Lett.* **99**, 183101 (2011).

10. L. Vayssieres, C. Sathe, S. M. Butorin, D. K. Shuh, J. Nordgren, and J.-H. Guo, *Adv. Mater.* **17**, 2320 (2005).

11. P. Ardalan, T. B. Brennan, H. B. R. Lee, J. R. Bakke, I. K. Ding, M. D. McGehee, and S. F. Bent, *ACS Nano* **5**, 1495 (2011).

12. M. Grätzel, *Inorg. Chem*. **44**, 6841 (2005).

13. N. Tétreault, É. Arsenault, L.-P. Heiniger, N. Soheilnia, J. Brillet, T. Moehl, S. Zakeeruddin, G. A. Ozin, and M. Grätzel, *Nano Lett.* **11**, 4579 (2011).

14. M.-H. Kim and Y.-U. Kwon, *J. Phys. Chem. C* **113**, 17176 (2009).

15. K. S. Leschkies, R. Divakar, J. Basu, E. Enache-Pommer, J. E. Boercker, C. B. Carter, U. R. Kortshagen, D. J. Norris, and E. S. Aydil, *Nano Lett.* **7**, 1793 (2007).

16. A. K. K. Kyaw, X. W. Sun, C. Y. Jiang, G. Q. Lo, D. W. Zhao, and D. L. Kwong, *Appl. Phys. Lett.* **93**, 221107 (2008).

17. K. Ernst, A. Belaidi, and R. Könenkamp, *Semicond. Sci. Technol.* **18**, 475 (2003).

18. C. Lévy-Clément, R. Tena-Zaera, M. A. Ryan, A. Katty, and G. Hodes, *Adv. Mater*. **17**, 1512 (2005).

19. T. Jiang, T. Xie, Y. Zhang, L. Chen, L. Peng, H. Li, and D. Wang, *Phys. Chem. Chem. Phys*. **12**, 15476 (2010).

20. R. Könenkamp, R. C. Word, and C. Schlegel, *Appl. Phys. Lett*. **85**, 6004 (2004).

21. *On Solar Hydrogen & Nanotechnology*; L. Vayssieres ed., John Wiley and Sons: Singapore, 2009.

22. L. Vayssieres, *Adv. Mater.* **15**, 464 (2003).

23. T. Ma, M. Guo, M. Zhang, Y. Zhang, and X. Wang, Nanotechnolgy **18**, 035605 (2007).

24. K. Zhu, E. A. Schiff, N.-G. Park, J. van de Lagemaat, and A. J. Frank, *Appl. Phys. Lett*. **80**, 685 (2002).

25. Y. Ling, G. Wang, D. A. Wheeler, J. Z. Zhang, and Y. Li, *Nano Lett*. **11**, 2119 (2011).

26. S. Gutmann, M. A. Wolak, M. Conrad, M. M. Beerbom, and R. Schlaf, *J. Appl. Phys*. **109**, 113719 (2011).

27. J. T. Tanskanena, J. R. Bakke, T. A. Pakkanen, and S. F. Bent, *J. Vac. Sci. Technol. A* **29**, 031507 (2011).

28. V. E. Henrich, *Rep. Prog. Phys.* **48**, 1481 (1985).

29. G. Korotcenkov, *Mater. Sci. Eng.* B **139**, 1 (2007).

30. J. Lahiri, S. Senanayake, and M. Batzill, *Phys. Rev. B* **78**, 155414 (2008)

31. L. F. J. Piper, L. Colakerol, P. D. C. King, A. Schleife, J. Zúñiga-Pérez, P.-A. Glans, T. Learmonth, A. Federov, T. D. Veal, F. Fuchs, V. Muñoz-Sanjosé, F. Bechstedt, C. F. McConville, and K. E. Smith, *Phys. Rev. B* **78**, 165127 (2008).

32. F. M. F. de Groot, M. Grioni, J. C. Fuggle, J. Ghijsen, G. A. Sawatzky, and H. Petersen, *Phys. Rev. B* **40**, 5715 (1989).

33. M. Abbate, F. M. F. de Groot, J. C. Fuggle, A. Fujimori, O. Strebel, F. Lopez, M. Domke, and G. Kaindl, G. A. Sawatzky, M. Takano, Y. Takeda, H. Eisaki, and S. Uchida, *Phys. Rev. B* **46**, 4511-4519 (1992).

34. C. McGuinness, C. B. Stagarescu, P. J. Ryan, J. E. Downes, D. Fu, K. E. Smith, and R. G. Egdell, *Phys. Rev. B* **68**, 165104 (2003).

35. J. Chouvin, J. Olivier-Fourcade, J. C. Jumas, B. Simon, Ph. Biensan, F. J. Fernández Madrigal, J. L. Tirado, and C. Pérez Vicente, *J. Electroanal. Chem.* **494**, 136 (2000).

36. H. Thakur, R. Kumar, P. Thakur, N. B. Brookesc, K. K. Sharma, A. P. Singh, Y. Kumar, S. Gautam, and K. H. Chae, *Chem. Phys. Lett.* **511**, 322 (2011).

37. J.-H. Guo, L. Vayssieres, C. Persson, R. Ahuja, B. Johansson, and J. Nordgren, *J. Phys.: Condens. Matter* **14**, 6969 (2002).

38. K. C. Mishra, K. H. Johnson, and P. C. Schmidt, *Phys. Rev. B* **51**, 13972 (1995).

39. S. O. Kucheyev, T. F. Baumann, P. A. Sterne, Y. M. Wang, T. van Buuren, A. V. Hamza, L. J. Terminello, and T. M. Willey, *Phys. Rev. B* **72**, 035404 (2005).

40. H.-J. Ahn, H.-C. Choi, K.-W. Park, S.-B. Kim, and Y.-E. Sung, *J. Phys. Chem. B* **108**, 9815 (2004).

41. X. T. Zhou, J. G. Zhou, M. W. Murphy, J. Y. P. Ko, F. Heigl, T. Regier, R. I. R. Blyth, and T. K. Sham, *J. Chem. Phys*. **128**, 144703 (2008).

42. X. T. Zhou, F. Heigl, M. W. Murphy, T. K. Sham, T. Regier, I. Coulthard, and R. I. R. Blyth, *Appl. Phys. Lett*. **89**, 213109 (2006).

43. L. Soriano, M. Abbate, J. Vogel, J. C. Fuggle, A. Fernández, A. R. González-Elipe, M. Sacchi, and J. M. Sanz, *Surf. Sci.* **290**, 427 (1993).

44. D. W. Fischer and W. L. Baun, *J. Appl. Phys.* **39**, 4757 (1968).

45. F. M. F. de Groot, M. O. Figueiredo, M. J. Basto, M. Abbate, H. Petersen, and J. C. Fuggle, *Phys. Chem. Miner*. **19**, 140 (1992).

46. A. G. Thomas, W. R. Flavell, A. K. Mallick, A. R. Kumarasinghe, D. Tsoutsou, N. Khan, C. Chatwin, S. Rayner, G. C. Smith, R. L. Stockbauer, S. Warren, T. K. Johal, S. Patel, D. Holland, A. Taleb, and F. Wiame, *Phys. Rev. B* **75**, 035105 (2007).

47. X. Chen, P.-A. Glans, X. Qiu, S. Dayal, W. D. Jennings, K. E. Smith, C. Burda, and J.-H. Guo, *J. Electron Spectrosc. Relat. Phenom*. **162**, 67 (2008).

48. H. Ikeno, F. M. F de Groot, E. Stavitski, and I. Tanaka, *J. Phys.: Condens. Matter* **21**, 104208 (2009).

49. P. Krüger, *Phys. Rev. B* **81**, 125121 (2010).

50. L. D. Finkelstein, E. I. Zabolotzky, M. A. Korotin, S. N. Shamin, S. M. Butorin, E. Z. Kurmaev, and J. Nordgren, *x-ray Spectrom.* **31**, 414 (2002).

51. S. O. Kucheyev, T. van Buuren, T. F. Baumann, J. H. Satcher, Jr., T. M. Willey, R. W. Meulenberg, T. E. Felter, J. F. Poco, S. A. Gammon, and L. J. Terminello, *Phys. Rev. B* **69**, 245102 (2004).

52. J. P. Crocombette and F. Jollet, *J. Phys.: Condens. Matter* **6**, 10811 (1994).

53. G. van der Laan, *Phys. Rev. B* **41**, 12 366 (1990).

54. J. A. Tossell, D. J. Vaughan, and K. H. Johnson, *Am. Mineral*. **59**, 319 (1974).

55. A. T. Paxton and L. Thiên-Nga, *Phys. Rev. B* **57**, 1579 (1998).

56. J. Bisquert, D. Cahen, G. Hodes, S. Rühle, and A. Zaban, *J. Phys. Chem. B* **108**, 8106 (2004).

57. S. Rühle and D. Cahen, *J. Phys. Chem. B* **108**, 17946 (2004).

58. S. Rühle and T. Dittrich, *J. Phys. Chem. B* **109**, 9522 (2005).

7 Conclusions and Outlook

This dissertation has comprehensively analyzed several related photoelectrode structures to contribute to the optimization of metal oxides for the solar-driven oxidation of water in photoelectrochemical cells. The first chapters presented results related to electrodes based on alpha-phase iron(III) oxide, a promising visible-light-active material widely investigated for this application. Studies of porous films fabricated by physical vapor deposition reveal the importance of structural quality, as determined by the deposition substrate temperature, on photoelectrochemical performance. Heterostructures with nanoscale feature dimensionality were explored and reviewed in a later chapter, which describes the methodologies to combine the unique and complimentary functional properties of dissimilar oxides to optimize the water photo-oxidation process Experimental results based on an iron(III) oxide-tungsten(VI) oxide system show enhancements associated with the heterostructure, which may indicate the presence of unexpected minority carrier dynamics, as observed additionally by ultrafast transient absorption spectroscopy

Next, a new conceptual framework for the design of solar water oxidation photoelectrodes based on the spatially inhomogeneous doping of wide-bandgap metal oxide nanostructures was introduced and experimentally verified. It is found that optical absorption and electronic conduction can be decoupled and optimized by spatially segregating the functional impurity species that facilitate their associated physical processes. In the later chapters, the presentation has emphasized the importance of interfacial regions of oxide heterostructures, whose electronic structures were analyzed comprehensively using soft x-ray spectroscopy. These studies indicate that the interfacial regions of electrodes possess distinct electronic structures, which deviate in terms of orbital character and occupancy from those of their constituent bulk oxides. These observations inform methodology to address certain operational deficiencies associated with the use of metal oxides for solar energy conversion applications.

There are a number of exciting advancements expected for this field in the near future. The progress for α-Fe_2O_3-based electrodes has been remarkable: photocurrent densities in standard conditions have increased from less than 500 mA cm^{-2} to greater than 3 mA cm^{-2} in the past decade. This observation has been compared to the remarkable progress observed for Si photovoltaics in the 1970s.[1] For example, recent results show that by heat treating the α-Fe_2O_3 structures studied in Chapter 3 of this dissertation, photocurrent densities approaching 4 mA cm^{-2} are attainable.[2] In terms of new materials, there are several ternary compounds which are promising for this application, including for example $BiVO_4$. These new materials are being effectively investigated by combinatorial techniques[3] as well as through calculations to supplement experiments. The investigation of oxide electronic structure, for example as presented in Chapters 5 and 6, has the potential to significantly deepen the community's understanding of candidate materials, as well as strengthen our understanding of oxide-electrolyte interactions. It is expected that feedback from these advanced characterization techniques, supported by theoretical investigations, will facilitate considerable progress in the design of oxide photoelectrode materials in the coming years.

7.1 References for Chapter 7

1. K. Sivula, F. Le Formal, and M. Grätzel, *ChemSusChem* **4**, 432 (2011).

2. Y. Ling, G. Wang, J. Reddy, C. Wang, J. Z. Zhang, and Y. Li, *Angew. Chem.* **124**, 4150 (2012).

3. T. F. Jaramillo, S.-H. Baeck, A. Kleiman-Shwarsctein, K.-S. Choi, G. D. Stucky, and E.W. McFarland, *J. Comb. Chem.* **7**, 264 (2005).